Measuring the orbital angular momentum of light with time mapping and using it to probe higher dimensional states.

by

Paul Joseph Bierdz

A dissertation submitted in partial fulfillment
of the requirements for the degree of
Doctor of Philosophy
(Physics)
in the University of Michigan
2014

Doctoral Committee:

Assistant Professor Hui Deng, Chair
Professor Paul R. Berman
Professor Çagliyan Kurdak
Professor Theodore B. Norris
Professor Duncan G. Steel

2014

In memory of my mother.

Acknowledgments

First, I want to thank my advisor Hui. Out of Bo, Renée and myself we were her firsts. During our first summer, she spent countless hours in the lab training us and having a exorbitant amount of patience. I am embarrassed to think back about how long it took me to align a laser into a fiber for the first time. But she was not embarrassed of me and rather patiently encouraged me in all things. I also appreciate and am thankful for her allowing me to pursue my own curiosity in the scientific realm while still funding me. Hui was also immensely approachable and we had many fruitful conversation about what it means to be a scientist. Apart from work, she was friendly and would host annual parties at her house or take us out for ice cream every time the undergraduates would leave us at the end of the summer. She is a role model of someone who can be incredibly patient, incredibly available and also incredibly brilliant and successful.

I would also like to thank my committee members, Professor Paul Berman, Professor Çagliyan Kurdak, Professor Ted Norris and Professor Duncan Steel, for taking their time to allow me to present my research to them and their many useful comments. I also want to thank Professor Luming Duan for his useful comments during my prelim.

I want to thank Professor Miles Padgett from the University of Glasgow for all the cool work that he has done with orbital angular momentum of light that has kept me interested in this field when my work was slow. I had the pleasure of meeting him and learned a lot during our short meeting.

Now for past and present members of Hui's group. Our optics tables are filled with experiments, thanks to you all. I thank you for our conversations and your friendship. Thank you Renée Harton, Lei Zhang, Seckin Senlik, Minchuan Zhou, Zhaorong "Joey" Wang, Tyler Hill, Jinhai Chen, Hoon Kim and Glenn Leung. I want to thank Tyler in particular for all the interesting mathematical problems we worked on. And also Lei for

reminding me to register for the pre-defense meeting with Rackham. Glenn, I wish you good luck. I also want to thank Connor Roncaioli and Minho Kwon for directly helping with me a lot of my experiments.

Oh wait, I forgot someone! Bo Zhang! He would be really sad if I didn't mention him, so I'll give him his own paragraph. Thank you Bo.

Thank you so much for all the friends that I have made here at the University: Michelle Adan, Sarah Anderson, Matt Bales, Kevin Bergemann, Alex Burgers, Midhat Farooq, Jake Ketchum, Jee Hyun Kim, Se Ryeon Lee, Yen Ting Lin, Gechuan Liu, Grant Meadors, Justin Nieusma, Ben Norman, Max Radin, Ryo Saotome, Tim Saucer, Chao Shen, Chris Trowbridge, Jia Xu, Yifan Zhang, Yuanyuan Zhang and Zhen Zhang. I want to especially thank Michelle and Matt for their practical help with finding a job and writing a thesis; and thank Yuanyuan for her help in critiquing my presentations.

To all the support staff in the physics department, you have been wonderful and really helped a panicked graduate student in times of need. I want to extend a special thanks to the Graduate Coordinator, Christina Zigulis who should also be considered my therapist, and Joe Sheldon who ensured the safety of all my packages including fist bumps.

To Adam Lausche. I am so thankful that I met you and that you were several years older than me. You were my graduate student mentor. Even though you were not in physics, you paved the path for me.

To Dr. Don Lincoln, my advisor at Fermilab, who helped me apply to college and graduate school, who gave me much needed advice about finding a job after graduate school and just being a general all around great guy and really inspired me to continue to be a scientist, even if not in high energy.

To Jin Ji, the creator of this LaTeX template and all the other contributors[1].

To Professor Theo Lasser and Matthias Geissbühler for their *Morgenstemning* and other color-blind friendly colormaps for MATLAB[1].

[1] http://www-personal.umich.edu/~dalle/codes/thesis-umich/

Now I want to take some time to thank the various people that helped brought me to and throughout graduate school where I could complete this work.

To my mother. She gave birth to me and raised me and instilled in me the importance of education. She would take us to the library almost every night to hang out and read books and let me check out any book, even if it seemed silly. So I would check a book half my size filled with glorious images of stars, galaxies and nebulae along with Go, Dog. Go![2]. She would feed my penchant for mathematics by buying me a small bag of marbles for every milestone I would make. She wanted all of my brothers and me to go to college. Well Mom, I'm getting a PhD; I did it, thank you for getting me this far. I miss you.

To my brothers, in our shared childhood and beyond. So many fights, but so many laughs.

To my grandparents, who raised me after my parents' deaths and also for being great grandparents before that and great-grandparents now; what a difference a hyphen makes!

To the Ruthenbergs. The best that I can say is that it's complicated, but you know who you are and why you are here.

To my wife Arina. Thank you for your all your support for these six long years. I have discovered you are truly a marvelous person, which these acknowledgements are too narrow to contain.

To Zoë and Mia. Without you, this thesis probably would have been finished sooner or with more content, but if I had the chance to go back and make the decision again, I'd pick you every time. Zoë I am so happy that you made me a father. I love playing with you, I love teaching you and I love loving you. The universe is amazing and I hope that you'll see that for yourself and be able to discover a section for yourself to show everyone. And Mia, I look forward to meeting you.

There have been countless others, but I must get on with the rest of the thesis. I still thank you. And I thank you, yes you, the reader, for reading and I hope that you can learn something about orbital angular momentum of light.

TABLE OF CONTENTS

LIST OF FIGURES

LIST OF TABLES

LIST OF APPENDICES

LIST OF ABBREVIATIONS

OAM orbital angular momentum of light

PBS polarizing beam splitter

QKD quantum key distribution

QZI quantum Zeno interrogator

SAM spin angular momentum of light

SLM spatial light modulator

SMF single mode fiber

SPDC spontaneous parametric down-conversion

SPM spiral phase mirror

SPP spiral phase plate

TAM total angular momentum

VPP vortex phase plate

ABSTRACT

The orbital angular momentum of light (OAM) is a fundamental property of light. Beams with OAM have a helical wave front that carries quantized orbital angular momentum $\ell\hbar$ per photon, where ℓ is any integer. This unbounded Hilbert space can increase information capacity of both classical and quantum communications and also improve and extend qubit and qudit quantum algorithms. Additionally, the use of the OAM modes allows for novel imaging techniques to directly observe and measure various topological properties of objects ranging from defects in semiconductors to rotating black holes and extrasolar planets. However, measuring such higher dimensional OAM states is fundamentally important, albeit challenging, in order to use this rich degree of freedom.

In the work that follows, I present two novel OAM to time mapping schemes and an application using the higher dimensionality of OAM to non-destructively probe quantum states. These are the first OAM measuring schemes to use the temporal degree of freedom to measure OAM. The use of the novel loop nature allows for high fidelity and high speed measurements of a large number of OAM states without significant increase in experimental resources. The first scheme experimentally demonstrates a compact and practical device to measure the OAM spectrum. I report a fidelity of -21.3 dB for 5 different OAM states. The second scheme extends the first, but uses non-demolition measurements to iteratively test for specific OAM values. While this increases experimental complexity, it allows for the detection of an arbitrarily large OAM value from a single photon. I also discuss details of each technique investigate the affects

of misalignment on the OAM spectrum. In the remaining part, I discuss my novel generalized quantum Zeno interrogation. The original quantum Zeno interrogation is limited to the two-dimensional state of a single object; while the generalized version has the ability to non-destructively probe the quantum state a set of objects, and deterministically imprint that information onto a single photon using the OAM degree of freedom.

CHAPTER 1

Orbital Angular Momentum of Light

1.1 History of OAM

Maxwell described light in a series of wave equations known as Maxwell's equations [3]; Poynting later published papers showing that light has both linear momentum [4] and angular momentum (in the form of polarization) [5]. But it was not until 1992 when Allen and coworkers discovered that light possesses as well defined orbital angular momentum in the paraxial regime in the form of Laguerre-Gaussian modes [6]. Since then, many researchers have discovered other interesting properties of orbital angular momentum of light (OAM), and also a variety of applications ranging from the quantum mechanical to astronomical. In this chapter, I will briefly introduce the history of light's momentum, then give the mathematical expression for light containing OAM, followed by discussion of the quantum mechanical nature of OAM and then lastly discussing various applications of OAM.

1.1.1 Light and momentum

In 1884, Poynting noted that electromagnetic fields had an energy flux density given by the, now called, Poynting vector $\vec{S} = \vec{E} \times \vec{H}$ where $\vec{E}$ and $\vec{H}$ are the electric and magnetic fields respectively. An electromagnetic field will exert a radiation pressure on objects equal to $1/c$ of the time average of the Poynting vector. This implies that light has linear momen-

tum [4, 7]. In quantum mechanics, where light has been quantized, the photons will have momentum but no mass [8].

In addition to linear momentum, light will have angular momentum. Initially theorized by Poynting in 1909 [5], then later in 1936, Beth experimentally verified light's angular momentum [9]. If circularly polarized light passes through a half wave-plate, the polarization would change to the opposite polarization. If light has angular momentum, the angular momentum must be conserved and thus imparted onto the waveplate itself! This change in angular momentum would manifest in the form of a torque that could be measured. A more recent experiment using optical tweezers to demonstrate the mechanical transfer of angular momentum to birefringent micro-particles was developed and readily accessible to undergraduates [10].

1.1.2 Paraxial wave equation

Helmholtz's equation describes time-independent source-less light waves (See Equation 1.1) where ∇^2 is the Laplacian, k is the wave vector and A is the amplitude.

$$\left(\nabla^2 + k^2\right) A = 0 \tag{1.1}$$

In the paraxial approximation, where the light is a beam rather than spherical wave, the z-component of the wave vector can be written as $k_z = \sqrt{k^2 - k_x^2 - k_y^2} \approx k - \frac{k_x^2 + k_y^2}{2k}$. This allows for the Ansatz of $A(\vec{r}) = u(\vec{r})\mathrm{e}^{ikz}$. Plugging back into the Helmholt'z equation:

$$\left(\frac{\partial^2}{\partial x^2} + \frac{\partial^2}{\partial y^2} + \frac{\partial^2}{\partial z^2} + 2ik\frac{\partial}{\partial z}\right) u = 0 \tag{1.2}$$

In the paraxial regime, the time-independent amplitude of the light wave in the propagation direction changes slowly with respect to the transverse amplitude; therefore, the second spatial derivative in the propagation direction is dropped yielding the equation below:

$$\left(\frac{\partial^2}{\partial x^2}+\frac{\partial^2}{\partial y^2}+2ik\frac{\partial}{\partial z}\right)u=0 \tag{1.3}$$

Note, the electric field is related to the field amplitude u by $\vec{E}\left(\vec{r},t\right) = u\left(\vec{r}\right)e^{ikz-i\omega t}\vec{e}\left(\vec{r},t\right)$ where $\vec{e}\left(\vec{r},t\right)$ is the polarization. In the paraxial regime, polarization is completely separate from the field amplitude u. Most laser beams are commonly described as solutions to the paraxial wave equation [11]. In the non-paraxial regime, this separation is not generally true; however, light still has a total angular momentum [12].

1.1.3 Laguerre-Gaussian and other sets of modes

The common solution to this equation is the fundamental Gaussian mode; however, higher order solutions exist. When considering rectilinear symmetry, the solutions are Hermite-Gaussian modes (Equation 1.4) [13, 14], while cylindrical symmetry provides Laguerre-Gaussian modes (Equation 1.6) [6, 14, 15]. Each solution set form a complete orthogonal set of solutions to the paraxial Helmholtz's equation; therefore, any paraxial beam (e.g., most laser beams) can be represented as a superposition of modes from either of these bases. Moreover, any Hermite-Gaussian mode can be written as a superposition of Laguerre-Gaussian modes and vice versa [16]. The fundamental Gaussian mode is both $u_{0,0}^{LG}$ and $u_{0,0}^{HG}$.

$$u_{m,n}^{HG}(x,y,z) = u_m^{HG}(x,z)u_n^{HG}(y,z) \tag{1.4}$$

$$u_n^{HG}(x,z) = \frac{1}{\sqrt{w(z)}}\sqrt{\frac{\sqrt{2/\pi}}{2^n n!}}e^{-\frac{x^2}{w^2(z)}}H_n\left(\frac{\sqrt{2}x}{w(z)}\right)e^{\frac{ik\rho^2 z}{2\left(z^2+z_R^2\right)}} \times e^{-i(n+1/2)\tan^{-1}\left(\frac{z}{z_R}\right)} \tag{1.5}$$

$$u_{l,p}^{LG}(\rho,\phi,z) = \frac{1}{w(z)}\sqrt{\frac{2}{\pi}\frac{p!}{(p+|l|)!}}\left(\frac{\sqrt{2}\rho}{w(z)}\right)^{|l|}e^{-\frac{\rho^2}{w^2(z)}}L_p^{|l|}\left(\frac{2\rho^2}{w^2(z)}\right)e^{il\phi} \times e^{\frac{ik\rho^2 z}{2\left(z^2+z_R^2\right)}}e^{-i(2p+|l|+1)\tan^{-1}\left(\frac{z}{z_R}\right)} \tag{1.6}$$

The beam waist is given by $w(z)$ (Equation 1.7) where w_0 is the beam waist at the focus, z_R is the Rayleigh range, $L_p^{|l|}(x)$ is the Laguerre polynomial and $H_n(x)$ the Hermite polynomial. The phase term containing $\tan^{-1}\left(\frac{z}{z_R}\right)$ is called the Gouy phase. The Laguerre-Gaussian modes are plotted in Figure 1.1.

$$w_z = w(z) = w_0\sqrt{1+\frac{z^2}{z_R^2}} \tag{1.7}$$

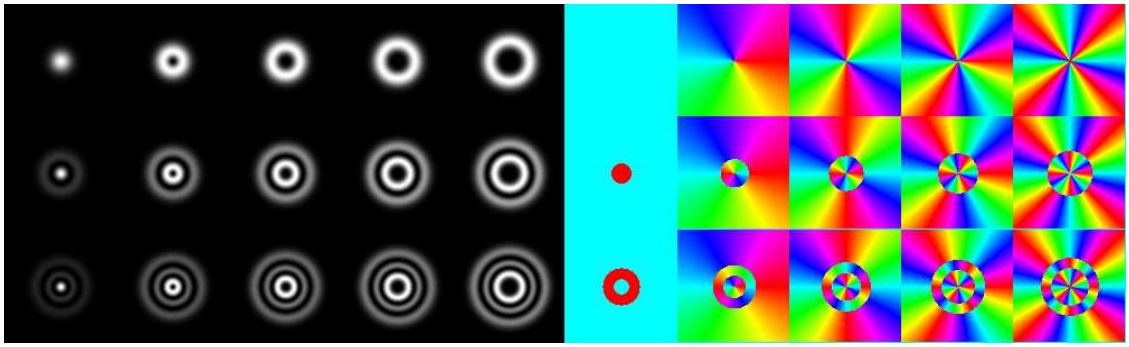

Figure 1.1: This figure is divided into two sections: (left) intensity and (right) phase. More precisely, three rows and 10 columns. The columns represent different ℓ's ranging from 0 to 4, then repeating for phase. The rows represent different p's ranging from 0 to 2. Negative values of ℓ will have the same intensity, but the phase would twist in the opposite direction.

Allen and coworkers noticed that Laguerre-Gaussian modes have a helical phase term $\exp^{i\ell\phi}$. Analogous to quantum mechanics, these modes would be an eigenfunction of the orbital angular momentum operator $\hat{L}_z = -i\hbar\frac{\partial}{\partial\phi}$ with eigenvalue $\ell\hbar$. In the ray-optics picture, the Poynting vector is perpendicular to the phase front, then Laguerre-Gaussian modes and other beams with helical phase will have a Poynting vector that twists about the optical axis. For a beam with OAM ℓ, wave vector k and at radius r from the optical axis, then the skew ray will have an angle $\beta = \frac{\ell}{kr}$. The momentum per photon is $\vec{p} = \hbar\vec{k}$; therefore, the angular momentum per photon is $\vec{r}\times\vec{p} = r\hbar k\sin\beta$. In the paraxial approximation $\sin\beta \approx \beta$; therefore the orbital angular momentum per photon is $\hbar\ell$, as expected. Allen and coworkers used another approach of deriving the OAM to energy ratio, which is ℓ/ω, which implies $\hbar\ell$ orbital angular momentum per photon.

Phase singularities, in general, have been studied since 1974 in both acoustic and optical fields [17, 18]. In 1974, Nye and Berry observed lines of undefinable phase (phase singularities) in radio echoes in the ice sheets in Antarctica [19]. In 1990, Bazhenov observed phase singularities in laser light by interfering Laguerre-Gaussian modes and observing the fork dislocation pattern [20]. However, none of these researchers associated helical phase patterns with orbital angular momentum of light before Allen and coworkers in 1992.

While the 1992 seminal paper discusses Laguerre-Gaussian modes containing orbital angular momentum of light there are other modes of interest to researchers. One such example are Ince-Gaussian modes, which is a third class of orthogonal complete solutions to the paraxial wave equation. They are the solutions in elliptical coordinates and serve as a continuum between Laguerre-Gaussian and Hermite-Gaussian modes [21, 22, 23]. Another interesting set of modes are called Bessel beams, but they are solutions to the full Helmholtz's equation and have infinite energy (like plane waves) [24]; the paraxial solutions are called Bessel-Gauss beams [25]. In both cases, they have the helical phase factor $\mathrm{e}^{i\ell\phi}$ which imparts the beam with OAM $\hbar\ell$ per photon.

The term OAM mode is technically ambiguous; therefore, throughout this thesis when I refer to an OAM mode, I am only concerned with the helical phase twist $\mathrm{e}^{i\ell\phi}$ which gives the original angular momentum. Sometimes I will refer to the ℓ-state, or a beam or wave with helical phase. This matches what I have read in literature and it is my opinion that this provides for less clunky exposition since often the ℓ value is generally the most important. However, when I do refer to a generic OAM state I am usually thinking about Laguerre-Gaussian modes, either with $p = 0$ or summing over all p-states. Wherever the exact transverse mode is important to the discussion, I will then refer to the precise mode.

1.2 Quantum Nature of OAM

In the previous section, I introduced the concept that light has angular momentum and in the paraxial approximation, light has a well-defined separation between spin angular momentum (polarization) and orbital angular momentum (helical phase front). Moreover, light has quantized orbital angular momentum of $\ell\hbar$ per photon. In this section, I will discuss the quantum mechanical implication of OAM.

Light, as what is known from quantum mechanics, is quantized in units called photons. Einstein originally postulated the existence of quanta of light, in part, to solve the ultraviolet catastrophe. This effect is called the photoelectric effect and the quanta of light, now called photons, would have quantized energy $E = \hbar\omega$ where $\hbar$ is Planck's constant divided by 2π and ω is the angular frequency [26]. Earlier, I derived a classical explanation for OAM. Like polarization, OAM exists at the quantum level and is an extremely useful quantum resource. For example, in 1996, Dholakia *et al.* demonstrated that through second-harmonic generation, not only is the energy of the photon doubled, but so is the ℓ value [27]. And unlike polarization, there are an arbitrarily large number of different orthogonal OAM states, opening up studying quantum mechanics of light in higher dimensions.

1.2.1 Entanglement of OAM

Entanglement is truly a quantum phenomenon [28, 29, 30, 31, 32]. Originally entangled photons were produced via atomic cascades [31] and now are commonly done via spontaneous parametric down-conversion (SPDC) [33]. SPDC [34, 35] is a non-linear process that splits a "pump" photon into two photons ("signal" and "idler") in a way that conserves energy (Equation 1.8) and momentum (Equation 1.9). SPDC is now commonly used in experiments involving entanglement of photons.

$$\hbar\omega_p = \hbar\omega_s + \hbar\omega_i \tag{1.8}$$

$$\vec{k}_p = \vec{k}_s + \vec{k}_i \tag{1.9}$$

Entanglement in the many different degrees of freedom for a photon has been demonstrated: polarization [36, 37, 33], linear momentum [38, 39], time-energy [40, 41], time-bin [42] and other spatial modes, like Hermite-Gaussian [43, 44], the p-modes of Laguerre-Gaussian [45], Bessel-Gaussian modes [46] and Ince-Gauss modes [47]. If two or more of these categories are entangled together, it is called hyper-entanglement [48, 49, 50, 51] including that of polarization and OAM [52].

Entanglement in the OAM degree of freedom has been demonstrated. The first non-trivial case in 2001 was by Zeilinger's group by demonstrating entanglement in three different OAM states ($\ell = -1, 0,$ or 1) [53]. In 2011, entanglement of 11 different ℓ values was demonstrated by Dada *et al.* [54] and very recently in 2014 the creation and measurement of a massive 100x100 dimensional entangled system using the photons' transverse modes [55] was also demonstrated. These experiments have not only demonstrated the feasibility of using the OAM degree of freedom for a quantum resource, but also the arbitrarily large Hilbert space that is possible with OAM.

Due to the azimuthal symmetry of the SPDC Hamiltonian [56], OAM is expected to be conserved throughout this process. This is true for mostly collinear type-I SPDC and the selection rule is similar to the energy and linear momentum (Equation 1.10) [57] and the output wavefunction will be an entangled state in OAM (See Equation 1.11).

$$\ell_p = \ell_s + \ell_i \tag{1.10}$$

$$|\psi\rangle = \sum_{\ell=-\infty}^{\infty} c_\ell |\ell_p - \ell\rangle_s |\ell\rangle_i \tag{1.11}$$

However, in general [58], OAM is not conserved. Tweaking the parameters of the SPDC, like crystal thickness, can change the spiral bandwidth (which changes c_ℓ) to either

make the output state entangled in a few OAM states or many [59].

While experimental verification for entanglement was demonstrated in 1972 [31] there still remains a few technical loopholes. Closing these loopholes is not just in the interest of good science, but for good secure quantum communication schemes that use entanglement since any asinine attack can be thwarted [60]. One loophole is called locality, or that space-like intervals are required for detection to prevent any subluminal communication no matter how improbable. The second loophole invokes the fair-sampling assumption in which events that are detected represent a fair-sample of all events, not a biased sample that would make the experiment work. The third assumption is in which the settings of the experiment are not influenced by the states created. Use of detectors set by quantum random number generators alleviates the third loophole. The local loophole has been closed by use of photons [61]. The detection loophole has been closed by use of ions [62] and very recently with photons [63], albeit with an experiment in which closing the locality loophole would be extremely difficult due to the use of special high-efficiency detectors. However, the use of higher dimensional states, like OAM, can be used to close the detection (fair-sampling) loophole because the detection efficiency required for an inequality violation is reduced, reaching a limit of $1/d$ in the limit of large d, where d is the dimension of the system [64]. Therefore, using normal detectors to allow for space-like separation, all loopholes could be conceivable closed simultaneously with the use of OAM. That would be an exciting experiment.

1.2.1.1 Fourier relationship between OAM and angle

Quantum mechanics states that precise information about all measurables of a system cannot be simultaneously knowable. This is the uncertainty principle and there are uncertainty relationship between conjugate variables, like the canonical example of position and momentum [65, 66, 67]. OAM and angular position are conjugate variables [68], albeit with a more complicated uncertainty relationship as shown below:

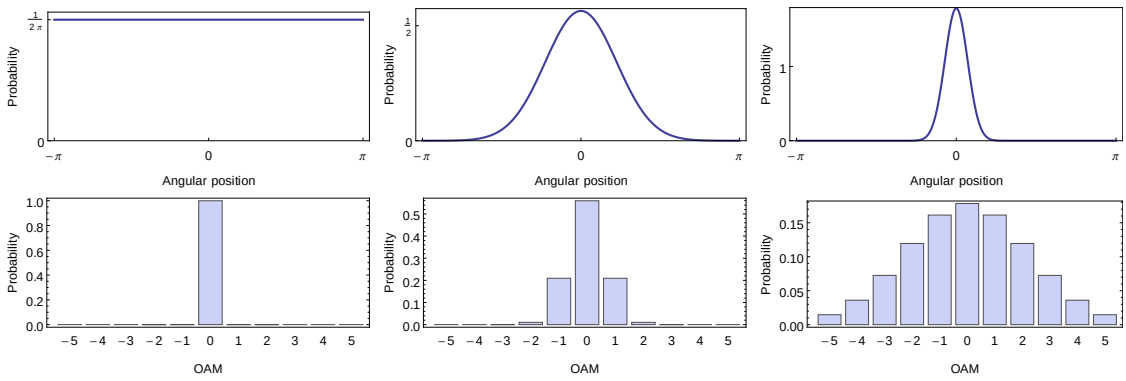

Figure 1.2: Top: The angular position ranging from all angles (open aperture), to narrow angular range. Bottom: The corresponding OAM uncertainty where the original state before passing through the angular aperture was $\ell = 0$.

$$\Delta\phi_\theta \Delta\ell \geq \frac{1}{2}\left|1 - 2\pi P(\theta)\right| \tag{1.12}$$

$P(\theta)$ is a complicated expression that depends on the uncertainty in the angles [69]. In the limit of a small uncertainty of angles, $P(\theta) \to 0$, one recovers the standard uncertainty relationship. In the limit of all angles (full aperture) there is no uncertainty in OAM. This is like the Fourier relationship between a Dirac-delta function and a constant; except that angles only range from $-\pi$ to π instead of all real values[1]. Figure 1.2 shows three examples of this relationship.

This relationship is important to consider when encoding and transmitting messages, or use imaging techniques with OAM, since partial angular measurements puts a fundamental limit on the fidelity of OAM spectrum of the source. The uncertainty relationship has been confirmed in 2008 with entangled photon pairs [70] and in 2010, the use of angular position states in lieu of the conjugate OAM states has been shown for quantum information schemes [71].

OAM is well-defined and quantized for paraxial beams, conserved in various non-linear processes, such as frequency-doubling and SPDC and has a quantum mechanical uncer-

[1]The fact that the angles $\theta + N2\pi$ are all considered the same angle is what gives rise to the more complicated uncertainty relationship

tainty relationship with the conjugate variable angular position. Therefore, OAM is truly a quantum mechanical resource and the following section will discuss applications of OAM.

1.3 Applications of OAM

The orbital angular momentum of light has been exploited for a wide range of modern applications from increased bandwidth of quantum and classically communication, increased security in quantum networks, astronomical applications and novel detection and imaging techniques. In this section I will briefly describe some of the interesting applications of OAM.

1.3.1 Quantum Applications of OAM

One obvious and self-evident application for OAM is increased bandwidth for quantum communications [72, 73]. Normally, polarization is used to send qubits (2 dimensions) while OAM can be used to send qudits (d dimensions)[2]. Additionally, use of qudits, as opposed to qubits, can increase security for quantum key distribution. The BB84 protocol was the first quantum key distribution (QKD) scheme [74, 75]. The idea was for the two receivers, commonly called Alice and Bob, to share a secret key with only each other. In encryption parlance, if a one-time pad (key) that is at least the same size of the plaintext (the message) is used to encrypt the message, then the encrypted text is fundamental unbreakable without the key. However, distribution and creation of perfectly random one-time pads (keys) is difficult.[3]

The BB84 protocol solves the key distribution problem by allowing Alice and Bob

[2] In the literature, sometimes qunits or quNits is used instead

[3] For a bit of history, the enigma machines during World War II, if used properly, would have one-time pads to have unbreakable messages. However, the distribution of those keys were a concern. Currently, the key distribution problem is "solved" via public-key cryptography in which deriving the private key used to decode the message is a "hard" problem from the public key. However, Shor's quantum factoring algorithm that would solve the factoring problem in polynomial time [76] putting most current encryption schemes into jeopardy.

d	2	3	4	5	8
Maximal error rate (%)	11.00	15.95	18.93	20.99	24.70

Table 1.1: In quantum key distribution, the use of qudits increases the security of key exchange. The upper bound on the disturbance, or error rate, increases with increased d (dimension of system). Disturbance below this level has guaranteed security against coherent attacks or any weaker attacks.

to create a random key (random from quantum mechanics) that is shared only between those two parties. In fact, if the eavesdropper, Eve, attempts to listen in on the key, that will disturb the creation of the key and so Alice and Bob could detect eavesdropping. Therefore, there is a limit on how much information Eve can glean from Alice and if the mutual information between Alice and Eve (I_{AE}) is less than the mutual information between Alice and Bob (I_{AB}) then Alice and Bob can share a secret key. For BB84, this limit is 11% error rate. If the dimension of the system is changed from 2-dimensions to d-dimensions [77], the maximal error rate is increased as seen in Table 1.1 [78, 79, 80]. A successful qutrit (3-dimensional system) has been experimentally demonstrated in 2006 using OAM [81].

While larger Hilbert spaces (that OAM can provide) increases security for QKD, it can also be used to detect cheating for quantum coin-tossing protocols in which Alice and Bob once again are trying to share a message, but they do not trust each other. Alice sends Bob a state, Bob makes a bet, Alice tells Bob what she sent and Bob then verifies. Alice could simply send mixed states and lie and will win much more than 50% of the time. By using qutrits, the error rate of the protocol will be much more than normal error rate due to honest participants and lying can be detected. This experiment was carried out in 2005 and uses OAM to provide the three-dimensional Hilbert space [82].

The use of larger Hilbert spaces can also simplify quantum logic. One such example is the Toffoli gate, also called a CCNOT[4] gate, which has three inputs and outputs. If the first two inputs are logically true, then the third input is flipped; otherwise everything stays the same. The Toffoli gate, with the single-qubit Hadamard gate, form one of the simplest

[4]controlled-controlled-NOT

instruction sets for universal quantum computing [83]. Deconstruction of the three-qubit Toffoli gate requires at least five two-qubit gates (or six two-qubit gates if restricted only to CNOT gates). Naturally, other single-qubit gates are required. However, if one of the inputs is replaced by a qutrit, then only three two-qubits gates are used. The qutrit gate is not a complete qutrit gate because it only operates on two-dimensional subspaces at a time [84]. There have been other studies on qudits gates and the improvements on quantum computation [85, 86]. Using OAM allows for arbitrarily large Hilbert spaces for use of qudit gates, while still retaining all the advantages of a photon-based system.

1.3.2 Enhanced Classical Communication

In addition to enhanced quantum communication and computing, classical communications can have increased bandwidth due to the increased alphabet. In 2012, Alan Wilner's group demonstrated free space propagation information transfer speeds of 2.56 Tbit s^{-1} by multiplexing 16 OAM modes along with polarization and frequency multiplexing [87]. In the following year, the same group demonstrated slightly reduced speeds in an optical fiber at 1.6 Tbit s^{-1} using two OAM modes over 10 wavelengths in a fiber, or speeds at 400 Gbit s^{-1} using four OAM modes at a single wavelength [88].

However, OAM, being encoded in phase, is sensitive to atmospheric disturbance. OAM modes are eigenmodes of free-space propagation and thus have advantages over other non-orthogonal modes when diffraction effects are significant. However, when propagating through the atmosphere, turbulence will change the wavefront and distort the modes. The channel capacity will be adversely affected [89, 90]. Experiments have been performed to study the effects of atmospheric turbulence on OAM modes and OAM communication [91], including entangled states [92]. Since OAM values can take on any integer, encoding information by skipping OAM modes can salvage channel capacity.

Aside from optical frequencies, work has been done in the radio frequency where coherent measurements are electronically accessible. Tamburini *et al.* created a special radio

transmitter and receiver to create the helical phase front waves and transmitted two different radio signals at the same time and at the same frequency from a hotel balcony to an island about half a kilometer away [93]. Due to the orthogonality of the helical waves, both signals could be recovered independently of each other.

1.3.3 Imaging with OAM

The orbital angular momentum of light, like wavelength, polarization, linear momentum and other fundamental properties of light can be used to infer information from the sources, reflections, refractions or other interactions with objects. For example, the wavelength can be used in spectroscopy to identify chemical compositions. In this section, I will provide rich examples of how OAM can be used to image and measure interesting and unique properties of objects or phenomena [94]. In some cases, by rephrasing the problem in terms of OAM, or more precisely, Laguerre-Gaussian modes, the answer can be more apparent, or even in one of several orthogonal OAM states. The decomposition into the OAM "basis" is called the spiral spectrum.

The spiral spectrum can yield interesting information about a system. For example, due to the uncertainty relationship between OAM and angular position, the spiral spectrum of a known OAM source passing through an angularly truncated object will reveal information of the type of truncation. The spiral spectrum can also be used to identifying more complicated objects [94, 95], such as size and position of dielectric spheres [96]. Also, the correlation in OAM in entangled photon pairs can reveal information about the object being probed [97, 98]. Recently in 2014, Chen *et al.* devised a remote sensing scheme, the entangled photon pairs can be used to identify pure-phase objects without interacting with the object [99]. There is a recent review article giving more details about this subject [100].

In addition to direct identification of objects, the use of OAM or a vortex phase plates (a device to create OAM, which will be discussed in more detail in the following chapter) can be used to enhance standard imaging techniques. For example, spiral phase contrast mi-

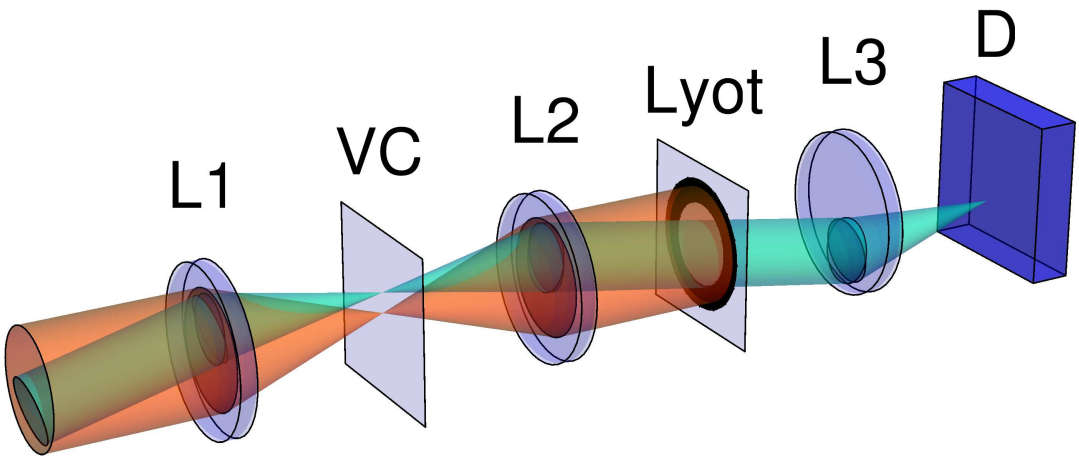

Figure 1.3: A diagram of a vortex coronagraph. L1, L2, L3 are lens in the system. VC is the vortex coronagraph (acts like VPP that adds the helically phase twist to the on-axis starlight (reddish-orange), but does not add much phase twist to the off-axis brown dwarf's or extrasolar planet's light (greenish-blue). Since the on-axis light gets a helical phase twist, it will focus to an annular shape and thus blocked by the Lyot stop. The off-axis extrasolar planet's light to pass through and arrive at detector D.

croscopy imaging uses a standard microscope setup, but places a vortex phase plate (VPP)[5] along the imaging pathway creates a sharp phase gradient and enhances edge detection for specimens [101, 102]. In a similar vein, the use of an optical vortex coronagraph in telescopes (See Figure 1.3) would allow detection of faint objects nearby bright objects, like extrasolar planets or weaker binary stars [103, 104, 105].

The basic operating principle of the vortex coronagraph telescope is that the bright star will be centered directly upon the telescope, after passing through the VPP, the star light will have $\ell = 1$ and will be focused to a ring instead of a bright spot. The dimmer, off-axis, object will have a superposition of ℓ-states [106], but having mostly $\ell = 0$, which would be focused to a bright spot. The use of a Lyot spot in the second Fourier plane would greatly suppress the on-axis bright starlight annulus allowing direct imaging of the much dimmer object. Additionally, there are some theories that sub-Rayleigh resolution can be achieved due to diffraction effects of higher order Laguerre-Gaussian modes [107, 108].

[5]Technically, the paper uses a spatial light modulator

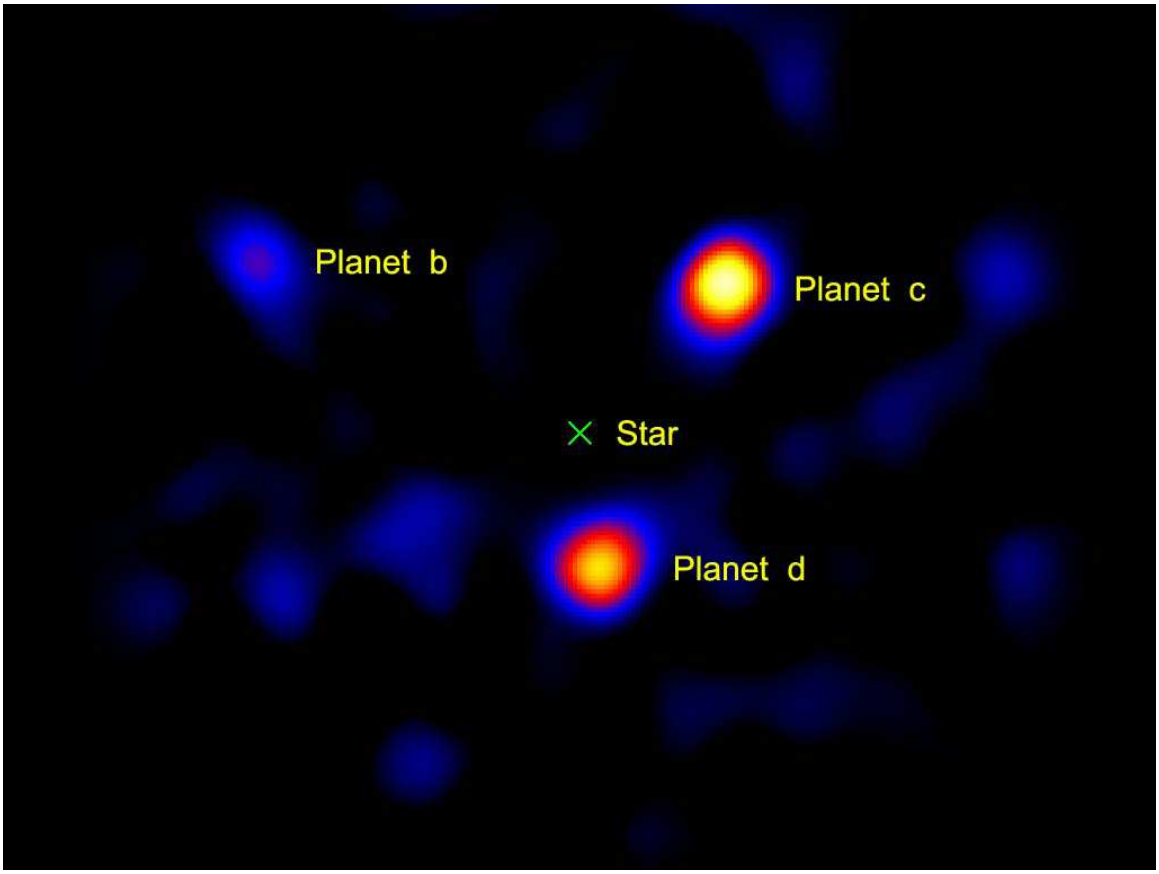

Figure 1.4: The image above is taken from a 1.5-meter portion of the Palomar Observatory's Hale Telescope in California. The star's intensity (HR8799) has been greatly suppressed and replaced with an X to indicate the position. The star is 120 light years away. The three planets, called HR8799b, c and d respectively are believed to be gas giants larger than Jupiter and orbiting the star at 24, 38 and 68 AU. For comparison, Jupiter is about 5 AU away from our Sun. This is the first image taken of extrasolar planets from a telescope this size. Image credit: NASA and JPL-Caltech and Palomar Observatory

This suppression and sub-Rayleigh resolution allows for smaller ground-based telescopes to image these astronomical systems. Several weaker partners to binary systems have been imaged via this technique [109, 110, 111] and the star HR8799 with three extrasolar planets has been directly imaged with a 1.5 meter ground-based telescope (See Figure 1.4) [112].

The spiral spectrum can also be used to directly detect rotating black holes. Additionally, the rotational speed and angle can be inferred from the distribution of the spiral spectrum [113]. This is due to strong gravitational fields near the rotating black hole and the light emitting from the accretion disc will be twisted and emit a distinct OAM signature.

OAM superposition states will produce azimuthal asymmetry in the intensity and from this pattern the spiral spectrum and other properties can be deduced. For example, in the past few years, Rumala *et al.* studied multiple reflections from a VPPs modelled as a Fabry–Pérot etalon. Due to multiple reflections, the output state would not just be $|\ell+L\rangle$, where $|\ell\rangle$ is the original state and L is the topological charge of the VPP, instead the output state will have a small contribution from even higher order states. This cause cylindrical asymmetry in intensity and yields a star-shaped pattern. If the wavelength is changed slightly, this star-shaped pattern will be rotated relative to the previous position at the previous wavelength. Thus one application would be an extremely sensitive frequency sensor [114, 115].

OAM can also be used indirectly to measure the rotation of remote objects. This is the rotational Doppler shift analogous to the linear Doppler shift which produces a frequency shift proportional to the velocity of the object towards or away from the detector. For the rotational Doppler shift, there is a frequency shift that is proportional to the product of the rotational speed and OAM even in the case where the angular momentum vector of the object is parallel to the vector between the detector and object [116]. This can be used to determined rotation of remote objects, for example, astronomical sources.

1.3.4 Optical tweezers

At the beginning of this chapter, I discussed the physical embodiment of momentum, orbital angular momentum, of light. In 1936, Beth demonstrated that polarized light does indeed possess angular momentum and can impart a torque on birefringent materials [9]. Due to the linear momentum of a laser beam, dielectric microparticles can be trapped in a focused beam due to the gradient force because the net force on the particle will move it into a position of highest intensity. For a focused Gaussian beam; there is a stable position at the focus (See Figure 1.5) [117]. For a Laguerre-Gaussian beam, He *et al.* demonstrated that black (or reflective) particles comparable to the beam waist would be similarly trapped [118] with a torque applied to the particle proportional to ℓ. A year later, Friese *et al.*

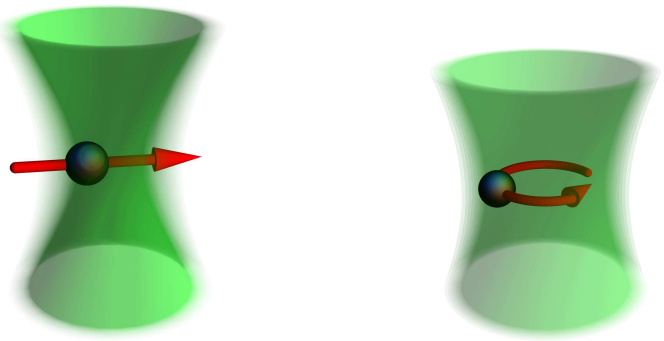

Figure 1.5: A cartoon of a particle trapped by a focused laser beam. (Left) The particle, as shown, is off-centered. There is a restoring force, the gradient force, that moves the particle towards the region of high intensity. This force is represented by the red arrow. (Right) The particle is also off-centered, but is now trapped by an OAM beam. It moves along the annulus because that is the region with highest intensity and will rotated about the optical axis, thus imparting the particle with orbital angular momentum.

trapped particles using OAM and polarization to show that the torque was $\Gamma = \frac{P_{abs}}{\lambda}(\ell + \sigma)$ where P_{abs} is the power absorbed. Therefore, using $\ell = 1$ and $\sigma = -1$, the particle would be trapped, albeit with no net torque [119]. More recently, more elaborate trapping schemes were developed, like an optical shield, where one OAM beam would trap the particle while the other OAM beam would have a larger annulus and shield the inner ring from other particles in the liquid [120].

1.4 Outline of Thesis

In this thesis I will discuss my contributes to the field of orbital angular momentum of light. This chapter is an introduction to OAM with a brief history, mathematical derivation and discussion of applications. The following chapter will give a detailed overview of a variety of methods used to measure OAM and compare and contrast them. Chapter 3 will discuss my experimental scheme used to measure OAM wit high fidelity by using an optical loop. Chapter 4 will give a treatise on various overlap integrals and the affect of misalignment on Laguerre-Gaussian modes relevant to the aforementioned experiment. Chapter 5 will discuss a modification to the loop design to incorporate a quantum Zeno interrogator in

order to measure the OAM for a single photon. Chapter 6 will discuss my work on the generalization and abstraction of quantum Zeno interrogator in using the OAM degree of freedom to probe higher dimensional states. Lastly the conclusion will summarize my work in the context of the field of OAM and give advice for future continuation of my work.

CHAPTER 2

Measurement of the Orbital Angular Momentum of Light

In the previous chapter, I introduced the concept of the orbital angular momentum of light and discussed a variety of applications. Naturally, measuring (and preparing) states of orbital angular momentum is very useful, but remains technically challenging. In this chapter, I will discuss a variety of existing methods used to determine the orbital angular momentum of light and discuss the various pros and cons of each approach. In the following chapters, I will discuss the two approaches I have invented in more detail; therefore, they will only be discussed briefly in this chapter.

In preparation for the discussion of how to measure the orbital angular momentum of light, it is important to first consider the experimental techniques used to measure another fundamental property of light, that is the polarization[1]. There are two kinds of methods to measure the polarization as indicated in Figure 2.1. The first kind of measurement uses two different, orthogonal, polarizers which filters all other polarizations except for the desired one, either horizontal or vertical[2]. The second kind uses a polarizing beam splitter to send the orthogonal states of polarization to different paths. The first case acts as a filter that only can detect one of the two states, while the second separates the eigenstates to be measured

[1]The previous chapter mentioned that polarization (spin angular momentum of light (SAM)) is distinguishable from OAM in the paraxial approximation. I will consider the paraxial approximation unless stated otherwise

[2]Or the basis vectors of the other two mutually unbiased bases - diagonal/anti-diagonal and left-/right-circularly polarized light

by two detectors. Another analogy is a monochormator versus a spectrometer. The former allows a narrow band of frequencies to transmit through the system, while the later images a large segment of the spectrum to photographer paper, or much more likely, a camera.

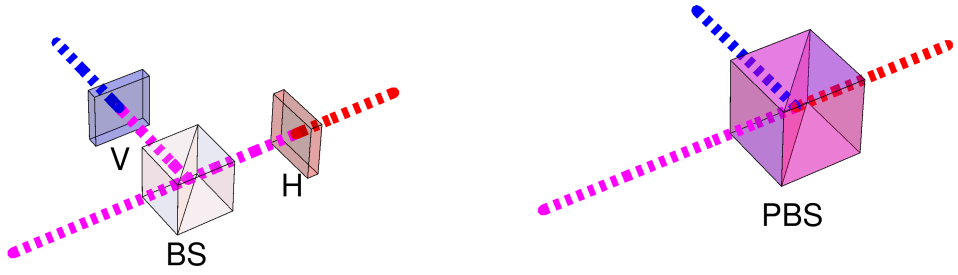

Figure 2.1: This figure shows two main methods for measuring the polarization of light. I have used color to denote polarization. Red being one polarization (horizontal) and blue the other. Without loss of generality, one of the other two mutually unbiased bases could have been chosen. Purple denotes unknown or mixed polarization. (Left), a probabilistic beam splitter randomly selects each photon to either attempt pass through the vertical or horizontal filter for future detection. (Right), a polarzing beam splitter separates the two states and allows for the two orthogonal states to be measured simultaneously and lose no information.

In the context of OAM measurements, I will categorize the methods of detection into three classes, two which are analogous to the aforementioned polarization methods. The classes are pattern recognition, filtering techniques and OAM beam-splitter techniques. There are some other esoteric methods, such as measuring the speed of rotation of micro-particles [118].

The OAM beam-splitter techniques have a bandwidth and efficiency advantage over the filtering techniques. The OAM beam-splitter can determine *which* OAM state the light is in, while the filtering techniques can only determine if the light is in a particle state or not. This is an important distinction. Therefore, for filtering techniques, in order to measure N different OAM states, at least N different filters will be required and thus require at least N identically prepared states. For communication or information purposes this erases all

advantages of using the larger Hilbert space OAM brings since the channel capacity of the system can never exceed 1 bit/photon — the same limit as using polarization. However, for other purposes, for example OAM spectroscopy, the to-be measured state is in a superposition of multiple eigenstates and thus fidelity may be more important than efficiency.

As an aside, most techniques, when measuring an OAM mode, will actually measure the probability the state is in that particle OAM mode according to Born's rule and not any phase[3] relationship between the OAM eigenstates. More specifically, an arbitrary state can be written as a superposition of OAM eigenstates as shown in Equation 2.1 where c_ℓ is the complex amplitude of the OAM eigenstate $|\ell\rangle$[4]. Some techniques can measure c_ℓ, others only $|c_\ell|^2$. In the case where the to-be measured state is an OAM eigenstate, there is no difference between global phases do not matter in quantum mechanics.

$$|\psi\rangle = \sum_{\ell=-\infty}^{\infty} c_\ell |\ell\rangle \tag{2.1}$$

Lastly, it is still an open problem whether or not there exists a simple and extremely efficient method to detect an arbitrarily large amount of OAM states with high fidelity. While the methods discussed in the section about OAM-beam splitters are interesting and ingenious, it is the author's opinion that none of them meet this criteria.

2.1 Pattern matching methods

Since OAM modes are just modes of light propagating, it should be possible to directly image them. There are a variety of ways to do this.

[3] This is a different kind of phase than the helical phase twist

[4] In terms of Laguerre-Gaussian modes introduced in the previous chapter, this would be a summation over p-states

2.1.1 Modal matching

The first and most obvious method would be to take an image of the intensity as a function of spatial position, although there are disadvantages to this technique. Since any paraxial beam is a superposition of Laguerre-Gaussian beams, all that is required is a fit the intensity pattern to a superposition of Laguerre-Gaussian modes. This method will be limited by the noise and dynamic range of the camera. Moreover, the complete state cannot be found in general, since there an infinite number of Laguerre-Gaussian modes. In fact, even with a handful of modes, fitting the complex amplitude coefficients will be computationally expensive. Moreover, while a singular Laguerre-Gaussian mode is a eigenmode of the paraxial wave equation, which means that the intensity pattern does not change under propagation (apart from an increased beam waist, like the Gaussian mode), a superposition can have interference between the Gouy phases and result in radically different intensity profiles along propagation. For example, one researcher looked at bottle beams which have zero intensity at the focus, but non-zero intensity elsewhere[121].

Nevertheless, direct imaging of OAM beams is extremely easy and many researchers use it to distinguish modes with helical phase and those without (Gaussian mode) due to the distinct annulus shape characteristic of OAM beams. Additionally, if the mode is a pure Laguerre-Gaussian mode $LG_{\ell,p=0}$, then the annulus size (the point with maximum intensity) scales as the square root of ℓ (full form given by Equation 2.2). Therefore with a known beam waist, w_0, and focus position, z, where z_R is the Rayleigh range, the actual value of ℓ can be measured albeit up to a sign.

$$\rho_{max} = \sqrt{\frac{|\ell|}{2}} w(z) = \sqrt{\frac{w_0^2 |\ell|}{2}\left(1 + \frac{z^2}{z_R^2}\right)} \tag{2.2}$$

$$I\left(\rho = \rho_{max}\right) = \frac{1}{w(z)^2}\frac{2}{\pi|\ell|!}|\ell|^{|\ell|}e^{-|\ell|} \tag{2.3}$$

2.1.2 Interference

The intensity information alone cannot determine the sign of the OAM value; yet, the phase information can reveal both the value and sign of OAM. However, at optical frequencies, no electronics can measure the phase directly, but interference techniques can recover the phase. One method to recover is to interfere with a reference plane wave at a skew angle and extract the phase from the Fourier transform at the spatial frequency of the skew angle. If the reference is a Gaussian beam, additional corrections would be required to compensate for the potentially curved phase front, but the phase twists from OAM will still be apparent. I use this method to visually inspect the quality of my input beams used in an experiment in Chapter 3.

The two interferometers discussed in this chapter are the Mach-Zehnder (Figure 2.2) and Michaelson (Figure 2.3) interferometers. As shown in the figures, the two arms of the interferometer can either be coincident, or interfere at a slight skew angle. A Gaussian beam will be the input and one arm will be the reference beam. The other arm will contain the experiment or whatever creates the OAM mode from the Gaussian beam. This allows for a coherent measurement. The reference beam can be focused or enlarged to function as an effectively plane wave over the region of the signal beam. If the signal and reference beam are coincident there will be spiral fringes [122]. By adjusting the focus, the spiral fringes will go one way, straighten out and then reverse direction. If the signal and reference beam are at a skew angle, then there will be a forked diffraction pattern where the number of the fork (1 line going into N+1 lines) determines the OAM value of the signal beam. Bazhenov and coworkers observed the relationship between the forked diffraction pattern and optical vortices before the work by Allen and coworkers in 1992, although they did not realize the connection between optical vortices and orbital angular momentum [20]. Simulations of these various interference patterns are shown in Figure 2.4 and a cartoon to understand where the fork interference comes from is shown in Figure 2.5.

However, it is still possible to recover the phase, or at least, qualitatively determine the

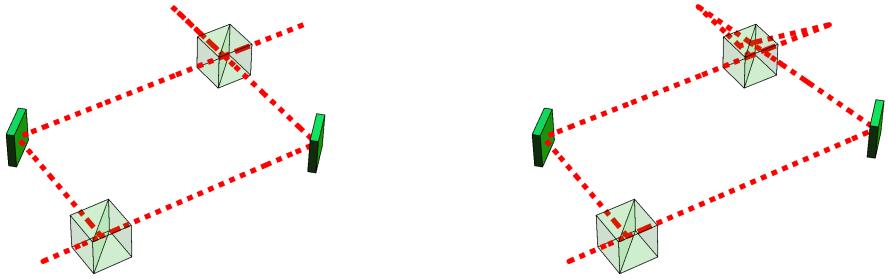

Figure 2.2: One of the basic kinds of interferometers is a Mach-Zehnder interferometer. (Left) The Mach-Zehnder interferometer is perfectly aligned so that the two exit ports are coincident. (Right) In one of the arms of the interferometer, the bottom-right mirror is angled and displaced slight so that the two beams from the two arms will interfere at a slight skewed angle. This will produce the fringe interference pattern. In general, the skewed angle is very small and not readily noticeable - the angle is simply exaggerated for illustrative purposes.

OAM value where a plane wave or Gaussian reference beam is unavailable, undesired or experimentally challenging. Such examples include light from astronomical sources, or when the experiment is not a coherent process, such as the light from exciton-polaritons in semiconductors in which the polaritons have been created from non-resonant pumping. Yet, even without a reference beam, experimenters can still get interference via self-interference with a Michelson interferometer[5], or biprism [123]. By designing the Michelson interferometer (Figure 2.3) such that the two beams will come not only at a skew angle, but also displaced when imaged on the camera, a fork pattern can be observed as seen in Figure 2.6. The astute reader will notice that there are two fork dislocations, both facing in the opposite direction. This is because the signal is split into two beams. From the first beam's perspective, it sees the other beam greatly displaced. Displaced from the center, the change in phase is rather small, much less than 2π; therefore, behaves somewhat like a plane wave. This produces the fork pattern. For the second beam, this perspective is also true, so there is another fork. The second fork could be considered a "fake" fork because one would only expect to see a single fork when interfering with a plane wave or Gaussian.

[5] Or even just the Mach-Zehnder interferometer again.

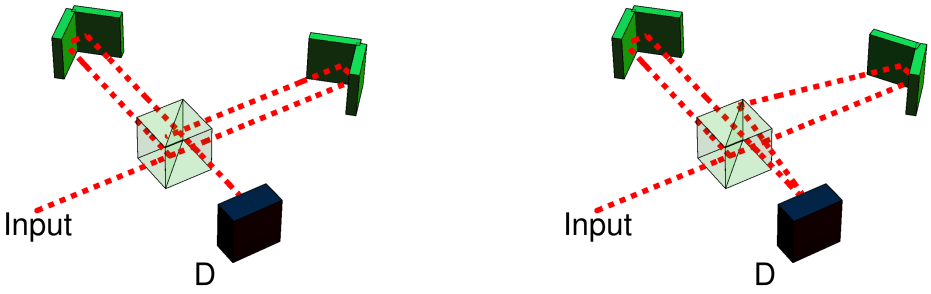

Figure 2.3: The other kind of basic interferometers is a Michaelson interferometer. (Left) The Michaelson interferometer is perfectly aligned so that the beams exiting the lower port are coincident. Technically, the Michaelson interferometer has two exit ports, but it is often left unused. (Right) one of the arms of the interferometer is greatly exaggerated so that at the exit port, the two beams from the two arms will interfere at a slight skew angle. This will produce the fringe interference pattern.

2.1.3 Diffraction patterns

Diffraction from special apertures, being sensitive to phase, can create distinct patterns in near- or far-field, which allow researches to determine the OAM value. The far-field pattern of light through an aperture can be calculated by the two-dimensional Fourier transform the electric field amplitude immediately after the aperture (See Equation 2.4). This is known as Fraunhofer diffraction. This is contrasted with Fresnel diffraction which is near-field diffraction. What is considered near and far (distance L) is relative based on the size of the aperture (a) and the wavelength of light (λ) denoted by the Fresnel number (F) given in Equation 2.5. $F \gg 1$ is considered the Fresnel regime, while $F \ll 1$ is considered the Fraunhofer [124]. A lens can also be used to achieve Fraunhofer diffraction.

$$E_{\text{far field}}\left(\vec{k}_{\perp}\right) = \int \tau\left(\vec{r}_{\perp}\right) E_{\text{source}}\left(\vec{r}_{\perp}\right) \mathrm{e}^{\mathrm{i}\vec{k}_{\perp}\vec{r}_{\perp}} d\vec{r}_{\perp} \tag{2.4}$$

$$F = \frac{a^2}{L\lambda} \tag{2.5}$$

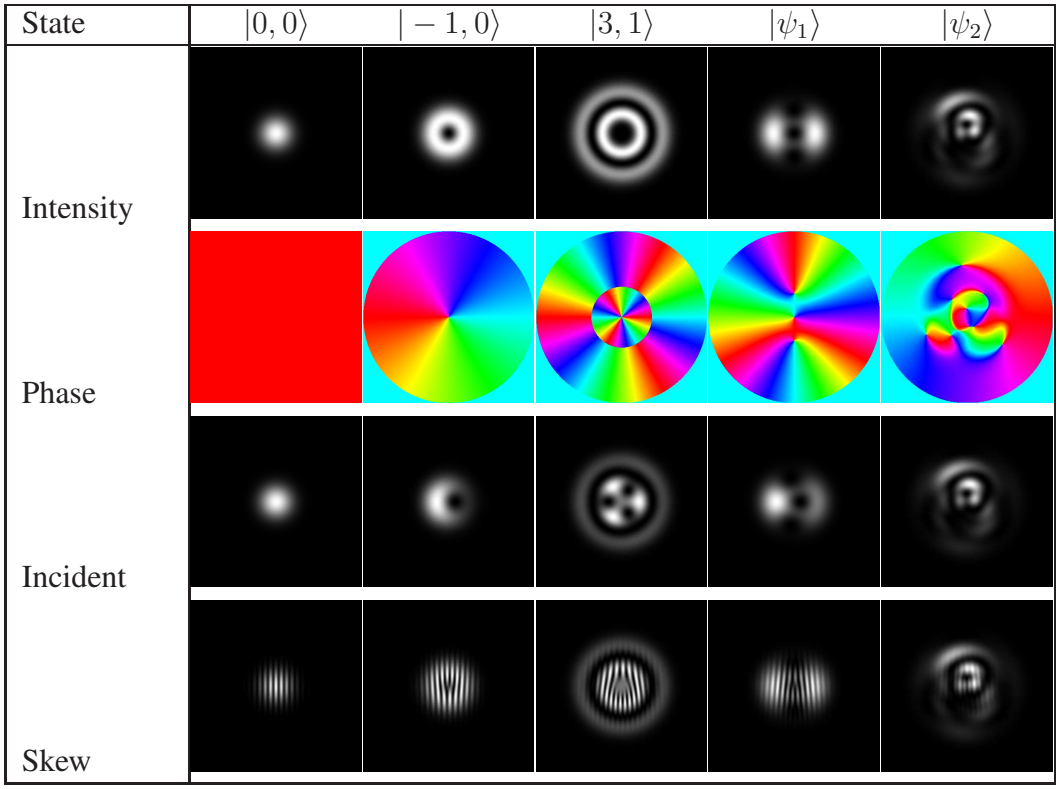

Figure 2.4: Simulated intensity, phase and diffraction patterns for six different states. Other states causing interference are Gaussian beams. Every state is an eigenstate and can be visually identified. $|\psi_1\rangle$ is a superposition of two states $\frac{1}{\sqrt{2}}(|1,0\rangle + |3,0\rangle)$ and $|\psi_2\rangle$ is a superposition of five states. $\frac{1}{\sqrt{5}}(|2,1\rangle + i|-1,3\rangle + \mathrm{e}^{i0.2\pi}|3,0\rangle - |0,2\rangle + \mathrm{e}^{i0.6\pi}|1,1\rangle)$ For the superposition states is nearly impossible to identify the various components in the interference patterns.

2.1.3.1 Triangular aperture

One of the neatest and simplest methods to determine ℓ from an aperture was created by Hickmann and coworkers in 2010 using a triangle aperture to produce a triangular lattice of circles that gave the value and the sign of ℓ [125]. The helical phase produces an ℓ-dependent diffraction pattern at each of the triangles edges and in total produces a triangular lattice with $\ell + 1$ bright orbs per side as shown in Figure 2.7. Additionally, when the sign of ℓ is reversed, the entire diffraction pattern is flipped. Therefore, this is a rather neat and easy way to determine both the sign and magnitude of OAM eigenstates.

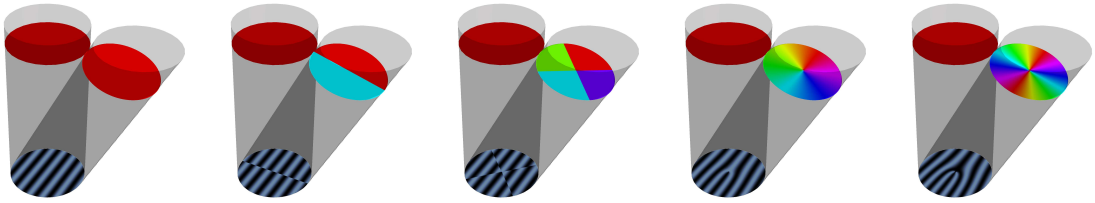

Figure 2.5: This cartoon gives an intuitive understanding of the fork dislocation pattern commonly associated with OAM. The first image shows the standard fringe interference pattern from two skewed plane waves. If the bottom of one of the plane waves is shifted π out of phase, then the interference pattern will shift as well. Including an intermediate step and one can see how the fork dislocation is form. The last image considers $\ell = 2$ and demonstrates the the prongs of the fork is always $\ell + 1$.

2.1.3.2 Multi-Point Interferometer

For the triangle aperture method to function, the size of the aperture is comparable to the size of the beam waist. In some cases, the beam waist could be very large when arriving at the detector and such a large aperture to capture the entire beam would be impractical. An example would be light arriving from astronomical sources having propagated long distances. Berkhout and Beijersbergen demonstrated a scheme, based on a multi-point interferometer, to determine the OAM value of a beam in which the total aperture area is very small. The device contains N individual pinholes evenly spaced on an figurative circle concentric with the optical OAM beam axis. The size of the pinholes need to be smaller than the space between them. A multi-point interferometer with N pinholes will only produce N unique patterns for N odd, and $N/2+1$ if N is even due to symmetry. Thus only distinguish N $(N/2 + 1)$ OAM states [126]. Berkhout and Beijersbergen also devised the algorithm to determine the c_ℓ coefficients in Equation 2.1 from these interference patterns, but noted that it would require many Fourier transforms and may be impractical for some purposes [127]. By using multiple circles, the technique could be extended to distinguish the radial modes (p) as well [128].

Figure 2.6: This interference pattern was created by interfering a Laguerre-Gaussian mode $|1,0\rangle$ with itself. The skew angle allows the fringes to be seen and a displacement of the beam allows phase singularities of both beams to be seen. This works because away from the phase singularity, the Laguerre-Gaussian mode has a locally homogeneous phase.

2.1.3.3 Near-Field Double-Slit

A group of researchers at Zhejiang University considered distinguishable patterns in self-interference for helically phased beams, but in the near-field instead of far-field [129]. In a setup similar to a Young's double-slit, they considered two Laguerre-Gaussian modes propagating along the same direction, albeit displaced from each other by some small distance d. This configuration could easily be made via a beam splitter and carefully placed mirrors, or a specially cut beam splitter. In the near-field there will be a figure eight pattern with $|\ell| - 1$ twists with the direction of the twists determined by the sign of ℓ. This distinguishes modes with $|\ell| > 1$. However, in the far-field the interference patterns are not distinguishable.

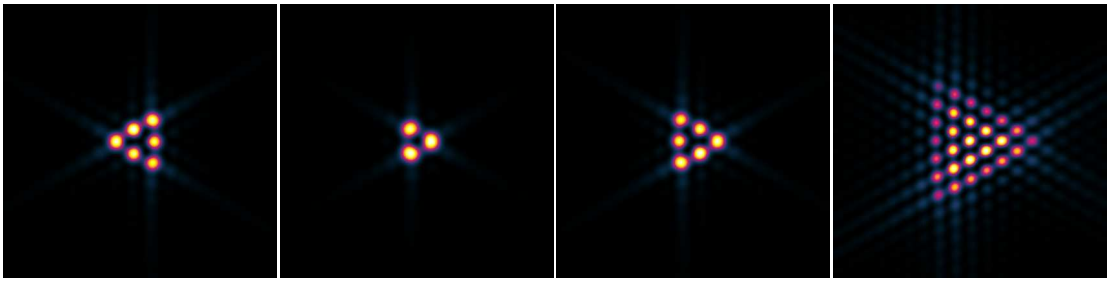

$\ell = -2$ $\ell = 1$ $\ell = 2$ $\ell = 6$

Figure 2.7: A beam with a helical phase twist when passing through a triangular aperture will self interfere and form a diffraction pattern that depends on both ℓ and its sign. In the figure, I have selected several ℓ values to show the triangle lattice pattern. By counting the lobes on the side, one can determine the ℓ value. Note, for negative values of ℓ the triangle lattice faces the opposite direction. These are simulated images to match the results shown by Hickmann *et al.*

2.1.3.4 Summary of Diffraction Patterns

Any of these pattern matching techniques result in images in which the patterns caused by different OAM states will spatially overlap. In other words, the location where a single photon hits the detector is insufficient to uniquely determine the OAM state. Many photons are requires to resolve and distinguish the intensity patterns from each other. Additionally, resolving superpositions of OAM states would be technically and computationally difficult. For the rest of the chapter I will discuss techniques that, in principle, would require only a few photons to distinguish the different OAM states.

2.2 Filtering methods

The polarization filter example requires two filters for the two different states. For N OAM states, at least N filters would be required. If a photon is in an OAM state other than the filter, the photon will be scattered or absorbed. Because of this inherent loss, filtering methods would require at least N copies of the original state to determine which of the N eigenmodes the state was in. The most common OAM filter is the single mode fiber (SMF),

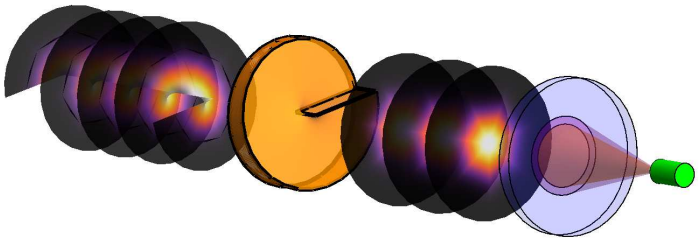

Figure 2.8: The $\ell = 1$ beam passes through the vortex phase plate decreasing the helical phase by a step of 2π thus turning the $\ell = 1$ beam into $\ell = 0$, the Gaussian beam, which then can be focused through a single mode fiber. Had any other $\ell \neq 1$ beam passed through the VPP, the beam would not be a Gaussian and thus not go through the fiber. This is the basic idea of the filtering techniques for measuring OAM

which, as the name suggests, only couples to a single mode[6], the Gaussian or $u_{0,0}^{LG}$ in the parlance of Laguerre-Gaussian modes. There are several techniques to produce an OAM mode from the fundamental Gaussian and by the reversibility of optics, the same technique can be applied to measure said OAM state (See Figure 2.8). This section will discuss these various techniques.

2.2.1 Cylindrical lenses

One technique that is used to create higher order Laguerre-Gaussian modes, but really used to distinguish OAM modes are cylindrical lenses. Cylindrical lenses can be used to convert Hermite-Gaussian modes into Laguerre-Gaussian modes [6, 130, 131]. This is due to the anisotropy in the focusing, allowing the different Gouy phase shifts along the different axes thus changing the relative phases in the superpositions and creating a Laguerre-Gaussian mode. Hermite-Gaussian modes can be created in a laser cavity by placing wires along the lines of zero intensity. This method was used by Allen and coworkers in order to create the Laguerre-Gaussian modes to discover OAM.

[6] As long as the alignment is perfect and this is very critical and Chapter 4 will discuss this in more detail

2.2.2 Forked diffraction grating

Forked diffraction gratings are commonly used to create and detected OAM when coupled with a SMF and generally in the form of a spatial light modulator (SLM)[7]. A SLM is a device that has individually addressable pixels in order to change the phase and/or intensity (for phase only, intensity only or complex SLMs) of the beam. The process works as a hologram in which the forked diffraction grating is calculated by the interference between a helical phase wave and a plane wave, so that when a plane wave diffracts from the grating, it will produce the helical phase wave. Bazhenov and coworkers noticed the connection between helically phase beams and forked diffraction gratings prioer to Allen and coworkers [20].

A forked diffraction grating operates under a similar principle of an ordinary diffraction grating. A forked diffraction grating with (topological) charge ℓ is mathematically determined by "adding" the helical phase term $e^{i\ell\phi}$ to a normal diffraction grating (See Figure 2.9). The m^{th} diffraction order will increase its OAM value by $m\ell$ [132]. Therefore, the zeroth order will be unchanged in phase and undergo specular reflection as in the ordinary diffraction grating. Additionally, there are two main kinds of gratings — blazed and unblazed, and these still apply to forked diffraction gratings. A blazed, or sawtooth grating, is often used to make a particle diffraction order most efficient. The equations for constructing each grating are given for both blazed (Equation 2.6) and unblazed (Equation 2.7) forked diffraction gratings, where Λ is the pitch of the grating, Arg returns the argument of the exponential between $-\pi$ and π and $Sign(x)$ returns either ± 1 if $x = \pm|x|$.

$$\frac{1}{2\pi} Arg\left[\exp\left(i\frac{2\pi x}{\Lambda} + \ell \arctan(y/x)\right) + \pi\right] \tag{2.6}$$

[7] A computer generated pattern printed on an overhead projector's transparency using a standard desktop printer can give proof-of-principle results with a laser pointer. This is an easy experiment and I urge the reader to try this.

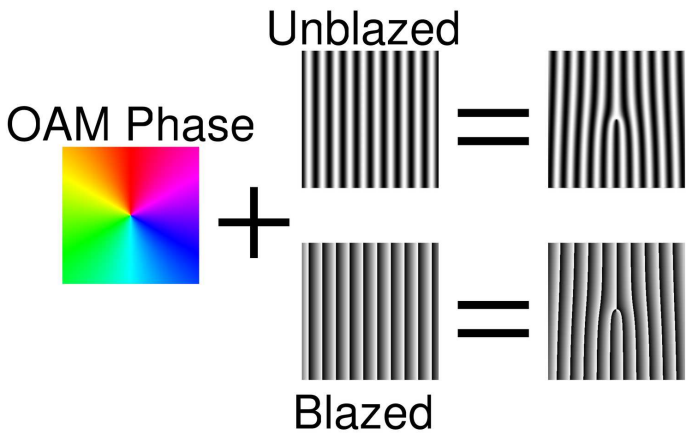

Figure 2.9: The fork diffraction patterns are taken by superimposing the desired OAM phase to reconstruct with the standard blazed or unblazed diffraction grating.

$$Sign\left[\exp\left(i\frac{2\pi x}{\Lambda}+\ell\arctan(y/x)\right)\right] \tag{2.7}$$

The forked diffraction gratings, as defined above, will produce the correct helical phase; however, in the language of Laguerre-Gaussian modes, for a phase-only forked diffracted grating; there will be a superposition of p-states. One researcher christened these modes Hypergeometric Gaussian modes [133]. Since most SLM are phase-only devices, it is useful to create a specific pure higher order Laguerre-Gaussian mode. In 1999, Davis *et al.* concluded that by changing the diffraction efficiency into the first diffraction mode at a pixel level, then both the phase and intensity can be changed producing an exact higher order Laguerre-Gaussian mode from a Gaussian [134]. There are several techniques in how to encode both the phase and diffraction efficiency and a good experimental review was provided by Ando *et al.* [135]. Only until recently was the exact solution to the simultaneous encoding of phase and intensity with a phase only SLM proven [136]. By the reversibility of optics, ℓ can be determined by diffract the incoming beam from the reverse forked diffraction grating and attempting to couple into a SMF. Zeilinger's group in 2001 was the first to use this principle to measure OAM between one of three values: -1, 0 and 1.

Beam splitters were used to probabilistically select from one of the three forked diffraction gratings [53]. Often, researchers use a SLM coupled with a single SMF and iterate through all the forked diffraction grating holograms to make a measurement.

By using a two-dimensional grating, one can produce orders of diffractions in both orthogonal directions and have 8 different first order diffraction locations, with a total of nine when including the zeroth diffraction order [73]. This produces an tartan like pattern. The simplest tartan forked diffraction grating would have topological charge 1 in one direction and 3 in the other; which would have $pm1m \pm 3n$ as the possible OAM values to measure with $m, n = \pm 1, 0$. This results in a grid of 9 beams ranging in OAM value from -4 to 4. This allowed for detection of 9 different OAM values when using one fixed forked grating without encountering fidelity and efficiency issues of higher diffraction orders or higher topological charges.

2.2.3 Vortex phase plate

The VPP, also known as spiral phase plate (SPP), of topological charge ℓ is an optic that imparts the helical phase $e^{i\ell\phi}$ to a beam. It works by having an azimuthally varying thickness of "glass" so than an incident input beam will receive an azimuthally varying phase shift [137, 138]. By selecting the thickness, index of refraction and wavelength of light, the VPP can shift the azimuthal phase by an integer multiple of 2π (See Equation 2.8). This creates an OAM state in a very similar way to the forked diffraction grating. In fact, for small angles, the first order diffraction from a forked diffraction grating of topological charge ℓ is exactly the same as the transmitted beam through a VPP of topological charge ℓ [139, 140] and can be used interchangeably in various measuring devices[8]. Also like some forked diffraction patterns, since the VPP imparts only a phase delay, it will convert a Gaussian into a Hypergeometric Gaussian modes [133] and not a pure higher order

[8] Of course, a VPP transmits the beam without changing alignment, while a forked diffraction grating will and any experimental setup will have to account for this

Number of steps	∞	32	16	8	4
$u_{0,0}^{LG}$ to $u_{1,0}^{LG}$ efficiency (%)	78.5	78.3	77.5	74.6	63.7

Table 2.1: The efficiency of converting a Gaussian beam to the first Laguerre-Gaussian mode using a VPP of charge 1 when considering a discrete number of steps to produce the azimuthally varying phase. For the continuous, ideal, case, this is $\pi/4 \approx 78.5\%$. This is less than unity because a VPP converts a Gaussian to a hypergeometric-Gaussian mode and not a pure Laguerre-Gaussian mode.

Laguerre-Gaussian mode.

$$\ell = \frac{h(n-1)}{\lambda} \tag{2.8}$$

vortex phase plate can have higher fidelity than forked diffraction gratings. Ideally, the VPP should smoothly vary the thickness of the material as a function of azimuthal angle, but manufacturing limitations may prevent this. Efficiency of the transformation of a Gaussian mode to a Laguerre-Gaussian mode (and vice versa) is limited by the discrete number of steps of the vortex phase plate, like a spiral staircase [141]. Although not many steps are required to get to maximal efficiency (See Table 2.1).

VPPs can also produce extremely high OAM modes and the highest demonstrated value is at $\ell = 5050$ [142] using a spiral phase mirror (SPM), a technology related to VPPs. A SPM is a mirror with a milled spiral kinoform pattern [143]. The kinoform pattern, like a Fresnel lens (Figure 2.10), the same idea can also be applied to regular VPPs which allow for easier manufacturing of higher order plates [144]. The VPPs I use in my experiments use this kinoform design produced by a lithographic process from RPC Photonics.

2.2.4 Q-plate

A Q-plate is a birefringent optic containing a topological defect of charge q caused by a anisotropic orientation of the fast axis of the material [145]. This has the interesting effect of converting a state with spin angular momentum of light (Left or Right circularly

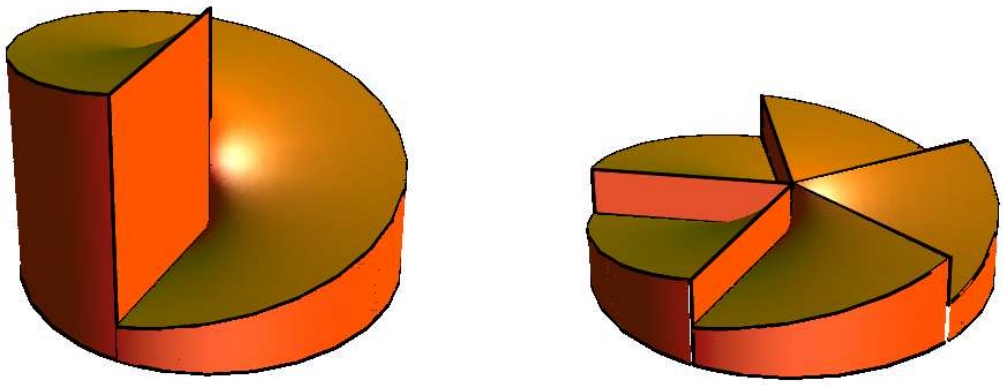

Figure 2.10: Two vortex phase plates with topological charge 5. The left VPP has a single ramp with phase delay 0 to $5 \times 2\pi$, while the right VPP has a kinoform pattern and thus has five ramps with phase delay 0 to 2π. The latter VPP is easier to mill. The steepness of the ramps are greatly exaggerated for clarity.

polarized) into the other and exchanging $\pm q$ orbital angular momentum of light as shown by Equations 2.9 and 2.10. If $q = 1$, then total angular momentum is conserved.

$$|L\rangle|\ell\rangle \rightarrow |R\rangle|\ell + 2q\rangle \tag{2.9}$$

$$|R\rangle|\ell\rangle \rightarrow |L\rangle|\ell - 2q\rangle \tag{2.10}$$

2.3 OAM beam-splitter methods

This section is about OAM beam-splitter techniques, which consists of techniques that efficiencies, in principle, could exceed $1/N$ where N is the number of OAM states to be measured. This is analogous to the polarizing beam splitter situation, except now instead of two orthogonal states limited by SAM, OAM can be any integer, limited only be the Fresnel number of the system due to the maximum allowable transverse modes [146, 147].

2.3.1 Dove prism

A Dove prism is an optical device that is sensitive to the ℓ value and can be used as part of a OAM beam-splitter setup. The Dove prism was invented by Heinrich Wilhelm Dove in the 1800s and it is used to rotate an image at an arbitrary angle because when the prism is rotated at an angle θ, the image is rotated by 2θ (See Figure 2.11). This means for OAM beams that have a phase term $\exp^{i\ell\phi}$ will pick up a phase $2\ell\theta$. This ℓ-dependent phase shift can be used to differentiate the different OAM modes. However, it was later discovered that Dove prisms will change the polarization slightly, therefore, an inverting prism can be used instead to only affect OAM [148, 149, 150].

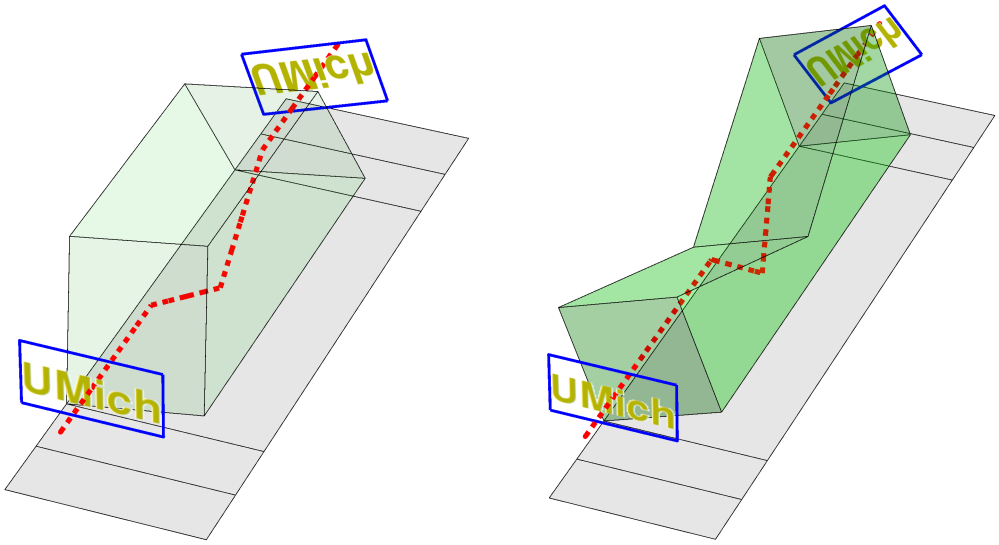

Figure 2.11: (Left) The Dove prism will have total internal reflection and thus rotate an image at twice the angle that the Dove prism was rotated. (Right) The inverting prism does the same, albeit without any change in polarization.

2.3.1.1 Rotational Doppler Shift

By shining light at a moving object and measuring the frequency shift, the speed of the object can be determined. This is called the Doppler effect [124]. If a half-wave plate is

rotating at some angular velocity Ω and circularly polarized light passes through the half-wave plate, the light will experience a frequency shift of $\sigma\Omega$ where $\sigma = \pm 1$ depending if the light is left or right circularly polarized [151]. Courtial *et al.* demonstrated a frequency shift $\Omega\ell$ for beams with orbital angular momentum ℓ when passing through a Dove prism with angular velocity Ω. This is to be expected because if a fixed rotation produces a fixed ℓ-dependent phase shift, then an angular velocity will produce an ℓ-dependent frequency shift. It is akin to rotating a watch and noticing that the second hand moves faster (or slower) [152]. Later that year, the group published an experiment with a Dove prism and half-wave plate to show that the frequency shifts in OAM and SAM (polarization) could be added to yield $\Delta\omega = \Omega(\ell + \sigma)$ [153]. However, these rotational Doppler shift experiments with OAM were carried out in the millimeter wave regime where both the relative frequency shift would be easier to measure and the alignment easier. At the time of writing, a similar experiment has not yet been carried out at optical frequencies.

2.3.1.2 Cascading Interferometer

By using the ℓ-dependent phase shift from Dove prisms along arms of a Mach-Zehnder interferometer (See Figure 2.12), constructive or destructive interference is possible for a congruence class of OAM states at the two existing ports. By judiciously choosing the relative angle between the Dove prisms the congruence class can be selected. By placing additional interferometers with different judiciously chosen relative angles between their Dove prisms, additional congruence classes can be additionally separated. For example, the first interferometer separates even and odd modes. With the pre-selected even modes, a second interferometer can additionally separated even modes into even and odd multiples of 2 (e.g., 0, 4, 8 out one port and 2, 6, 10 out the other). A third interferometer would then separated the states 1 and 3 (and modulo multiples of 4) from the pre-selected odd modes. In all, the scheme would require $2^N - 1$ interferometers to separate 2^N different OAM modes; however, it is theoretically 100% efficient.

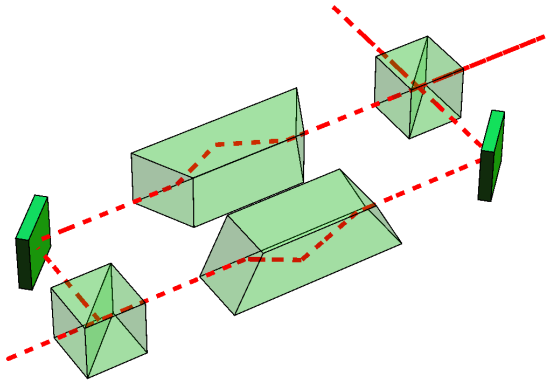

Figure 2.12: The Mach-Zehnder Dove prism interferometer works by introducing an ℓ-dependent phase shift. With a stabilized interferometer without the Dove prisms, the light would constructively interfere out of one of the ports and destructively interfere with the other. By introducing the ℓ-dependent phase shift, different congruence classes would interfere constructively or destructively out of the exit ports. In the example above, the relative angle of rotation between the Dove prisms is $\pi/2$, so there is an $\pi\ell$ phase shift, sorting between even and odd modes of ℓ.

The Glasgow group first came up with the idea in 2002[154], but then Wei and Xue improved upon the original scheme by using additional glass plates to do phase shifts to handle the odd cases [155]. In 2004, the Glasgow group further refined the scheme, using total angular momentum [156]. In 2011, Lavery *et al.* further improved upon the design by smashing together the optics directly and controlled the input beam direction to yield a very good even-odd mode sorter for up to $\ell = \pm 40$ with efficiencies as high as 93% [157]. The Mach-Zehnder Dove prism interferometer can be applied in reverse to merge N qubits into N photons along the same spatial channel, or multplex N qubits into a single photon [158].

2.3.2 Quantum Zeno Interrogator

The filtering techniques discussed earlier will absorb or scatter the mode if it does not match the desired value for the filter. However, a quantum Zeno interrogator [159] can

non-destructively probe the mode and determine if the mode will pass through the OAM filter or not without losing the mode[9]. Therefore, by setting up a loop scheme and iterating through the various filters, or more precisely, decreasing (or increasing) the OAM value of the beam with each quantum Zeno interrogator, one can determine deterministically and with arbitrarily high efficiency determine the OAM of a single photon by mapping it to time [160]. This is my OAM beam-splitter that I invented and details will be discussed in Chapter 5. A great advantage is due to the looping nature, only larger optics are required to detect higher order OAM states. This was also the *first* method to use the time degree of freedom to measure OAM.

2.3.3 Image reformater

In 2010, Berkhout *et al.* developed a scheme to measure OAM by converting the phase twists into linear phase gradients that when focused through a lens will focus to different regions [161]. This is achieved through an optical transformation, a technique first developed by Bryngdahl [162] that would convert the electric field in coordinates (x,y) to one of (u,v) in the Fourier plane. To convert the helical phase twists into linear phase gradients, a Cartesian to polar coordinate transformation would work, i.e., the unfolding of the donut. However, there are various restrictions on the allowable transformations and the one chosen in the end is given by Equations 2.11 and 2.12

$$u = -a \ln\left(\frac{\sqrt{x^2+y^2}}{b}\right) \tag{2.11}$$

$$v = a \arctan\left(\frac{y}{x}\right) \tag{2.12}$$

Originally, SLMs were used to perform the transform [161] but they lacked efficiency, over 70% light lost from the two SLMs. In a few years, the SLMs were replaced with

[9] With arbitrarily high efficiency

custom refractive elements to both reduce loss and increase the total number of states to be distinguished from 11 to 50 [163, 147]. In the same group, they also revised the image reformater to sort Bessel beams, which also contain OAM, in which they sorted both the azimuthal and radial modes [164]. This method is an OAM beam-splitter in the sense that the channel capacity can be much greater than 1 bit per photon (the limit imposed by polarization). However, due to the mathematical conversion from helical phase twists to linear phase gradients, there is a fundamental limit on the efficiency due to diffraction. To decrease this diffraction limit, and thus decrease crosstalk; skipping OAM states is possible. Additionally, there is recent research upon improving the algorithm for transformation, albeit the added complexity can also reduce efficiency [165].

2.4 Summary of Detection of OAM

This this chapter, I have presented a variety of methods used to detect and distinguish different OAM states, from pattern recognition through diffraction or interference to special OAM sensitive filters to perform a tomography of the state to full-fledge OAM beam-splitters that are useful for single photon measurements. I have also briefly presented my own work and my contribution to the field of OAM detection. Many other schemes require increase experimental complexity to measurement more OAM states. However, due to the loop nature of both my schemes, only larger optics, a requirement all OAM schemes would need in order to support the higher order transverse modes, would be required to detect more OAM states. In the following chapters, I will present in more detail my OAM detection methods.

CHAPTER 3

High Fidelity Detection of the Orbital Angular Momentum of Light by Time Mapping

3.1 Introduction

In this chapter I will discuss the concept, design, experiment and analysis of a compact, high fidelity measurement of the orbital angular momentum of light. The concept uses a VPP as the filtering mechanism to measure OAM and an optical loop to measure an arbitrarily high OAM value. With discussion with Hui Deng, I came up with a simplified design of my earlier work [160] that could be more experimentally realized. Fellow students Connor Roncaioli and Minho Kwon assisted in setup and optical alignment. Minho Kwon also assisted in preliminary analyzed and developed the Fourier techniques to measure the phase of the light beams in real time. Support, discussions and funding for the project was provided for by Hui Deng [166].

Here we demonstrate a simplified, and practical, OAM-to-time mapping scheme, which achieved a record high extinction ratio among five OAM states at an operation speed of 80 MHz. Since OAM is mapped to time, the same apparatus can be used to measure an arbitrary number of unique OAM states. We note that a similar scheme was also adopted in a recent experiment on time-division multiplexing of OAM, although the fidelity and repetition rate were orders of magnitude lower than reported here [167]. We also note that, without employing a quantum Zeno investigator, time-division schemes are not suitable for

improving channel capacity in communication.

3.2 Principle of the OAM spectrometer

As shown in figure 3.1a, our OAM spectrometer consists of a single optical loop to perform time mapping, a vortex phase plate (VPP) of topological charge 1 as an OAM ladder operator, and an SMF as a filter for the fundamental Gaussian mode with zero OAM. Consider an incident pulse consisting of a fraction β_ℓ of OAM components with OAM value ℓ, where ℓ is an integer and $\sum_{\ell=-\infty}^{\infty} \beta_\ell = 1$. The optical loop converts the pulse into a sequence of pulses equally separated by the round trip propagation time T in the loop. The loop needs an even number of reflections to maintain the same sign of OAM. Per loop, the VPP decreases the OAM value of each OAM component by 1. Hence, after N loops, the fractional β_ℓ of the original pulse will have OAM value $\ell - N$. Only the component with zero OAM value in each pulse can pass through the SMF to be detected. Thus, the OAM component β_ℓ with OAM value ℓ in the original pulse will exit the spectrometer at a time $t = lT$ (figure 3.1b).

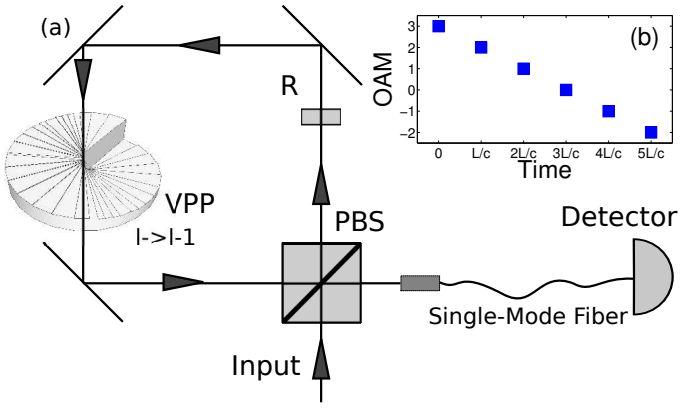

Figure 3.1: (a) Schematic of the OAM spectrometer, consisting of an optical loop that converts an input pulse into a sequence of pulses equally spaced in time, a VPP that decreases the OAM value by 1 per pass, and an SMF to filter out states with non-zero OAM. (b) Showing how the OAM value changes in time for an example input state with $\ell_0 = 3$.

3.2.1 Energy distribution

The distribution of the input-pulse energy among the sequence of pulses can be pre-calibrated and controlled by the beam splitter with polarization optics. We control the distribution with a polarizing beam-splitter (PBS) and half-wave plate (labelled as R in figure 3.1a) in the loop. The incident light is first set to be linearly polarized at an angle ϕ_0 with respect to the vertical. The PBS splits off the fraction of $\sin^2\phi_0$ into the first time window and sends the rest, now vertically polarized, into the loop. The wave plate R, rotated at an angle $\theta/2$ with respect to the vertical, rotates the vertically polarized light by an angle θ. The corresponding energy distribution is described below:

$$P(l) = \begin{cases} \sin^2\phi_0 & \text{if } \ell = 0, \\ \cos^2\phi_0 \cos^2\theta & \text{if } \ell = 1, \\ \cos^2\phi_0 \sin^4\theta \cos^{2(\ell-2)}\theta & \text{if } \ell \geq 2, \end{cases} \tag{3.1}$$

Here ℓ represents the ℓth output pulse. Alternatively, the PBS and wave plate can be replaced by a non-polarizing beam-splitter with a chosen splitting ratio for polarization-insensitive measurements. This would allow for information to be encoded in the polarization degree of freedom.

3.3 Experimental implementation

We implemented an OAM spectrometer as illustrated in figure 3.1(a). To test its performance, we used OAM eigenstates as input pulses and detected the output pulses using a Hamamatsu streak camera.

The input pulse was generated by diffracting a pulsed Gaussian laser beam off fork-diffraction patterns [20] on a Holoeye PLUTO LCoS spatial light modulator (SLM) with a period of about 10 lines per millimeter and pixel pitch of 8μm. The initial laser beam was from a Tsunami Ti-Sapphire laser centered at 730 nm, with a pulse width of 100 fs and

repetition rate of 80 MHz, and collimated with a 10x objective lens from an SMF ensuring an initial M^2 close to 1 and a spot size within the frame of the SLM.

We first verify the input states by measuring its far-field intensity and phase distributions, as shown in figure 3.2. The intensity distributions were measured with a charge-coupled device. The higher-order OAM beams show a larger spatial size as expected. Inhomogeneity in the radial intensity distribution reflects the lack of purity of the OAM value.

We measured the phase distribution by interfering the OAM beam with a reference Gaussian beam from the original laser. This produces a forked interference pattern. From this interference pattern we extract the phase front, as plotted in figure 3.2(f-j), by performing a Fourier transform, selecting the first diffracted mode, centring and then applying an inverse Fourier transform. The phase should twist about by $2\pi\ell$ for an ℓ^{th}-order OAM beam. Deviation from this results implies impure initial OAM states from optical aberrations or phase ripples from modulating the liquid crystals.

To calibrate the time-mapping and energy distribution of the OAM spectrometer, we used the zero-OAM Gaussian state as the input and replaced the VPP by a flat glass plate of the same thickness. The output from the SMF was detected by a Hamamatsu streak camera with a time resolution of 0.02 ns. As shown in figure 3.1(b), the input pulse was mapped into a sequence of pulses separated by $T = 1.03$ ns. The timing and dynamic range of the streak camera allowed us to measure the first five output pulses, or, the first five OAM states, at the laser repetition rate of 80 MHz. The experiment can also be redesigned to allow the measurement of a larger number of pulses by using different laser repetition rates, loop sizes or measurement devices.

The energy distribution among the pulses was calculated by integrating the intensity over each output pulse. The results are shown in figure 3.3(a) (the $\ell_0 = 0$ curve). We performed the same measurement with the input state $\ell_0 = 1$. The ratio of the two energy normalization curves at each ℓT gives an estimate of the misalignment of the SMF-coupling

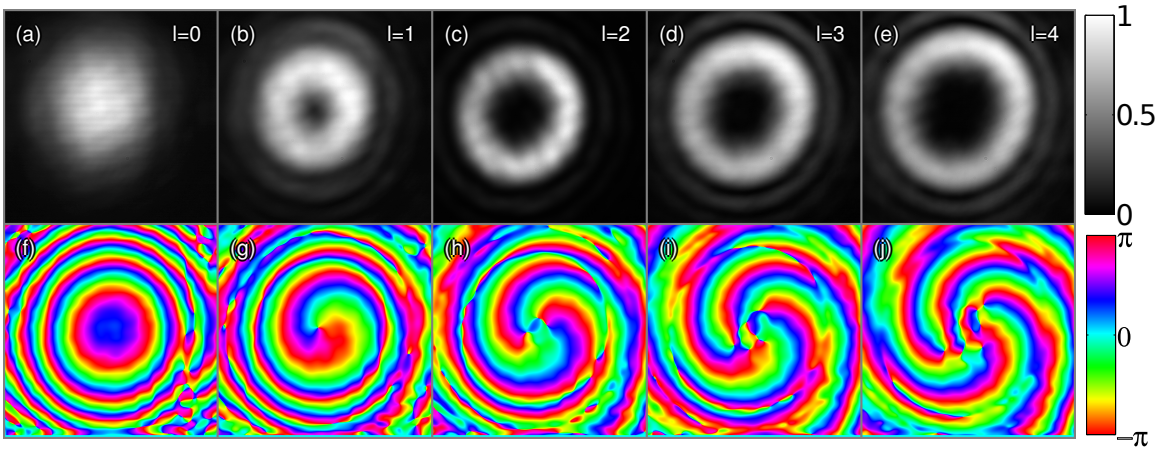

Figure 3.2: (a-e) The intensity measured with a camera of the different initial OAM beams from the SLM with $\ell = 0 - 4$. (f-j) The phase fronts of the input OAM beams. They are calculated from the interference patterns between the OAM beams and a reference Gaussian beam, as explained in the text.

(figure 3.3(b)) for the ℓ^{th} output pulse, as will be discussed in detail in Section 3.4.2 later. The uniformity of ratio among different ℓ confirms that the loop was well aligned.

Finally, we benchmark the performance of the OAM spectrometer by comparing the correct versus incorrect detection of an input OAM eigenstate. Figure 3.4(a-e) show examples of the output pulse sequences for input states $\ell_0 = 0 - 4$. The integrated intensity under each peak versus the input state ℓ_0 and the output time bin ℓ is shown in figure 3.4(f), where each row has been renormalized to the peak of the correct detection. We define the crosstalk to be the ratios between the left and right adjacent incorrect detections versus the correct detection, i.e., $\frac{P(\ell_0=\ell,N=\ell\pm1)}{P(\ell_0=\ell,N=\ell)}$ where $P(\ell_0, N)$ refers to the intensity measured at time NT with input OAM state ℓ_0. For $\ell_0 = 0$ to 4 we measured crosstalk values: -12.3, -18.8, -20.0, -21.1, -21.6, -23.2, -24.8 and -28.2 dB. The geometric mean of the crosstalk is 7.47×10^{-3} or -21.3 dB.

3.4 Analysis of the spectrometer performance

Below we simulate the performance of the spectrometer and analyze the main sources of error. We model the laser pulses as a superposition of Laguerre-Gaussian (LG) modes,

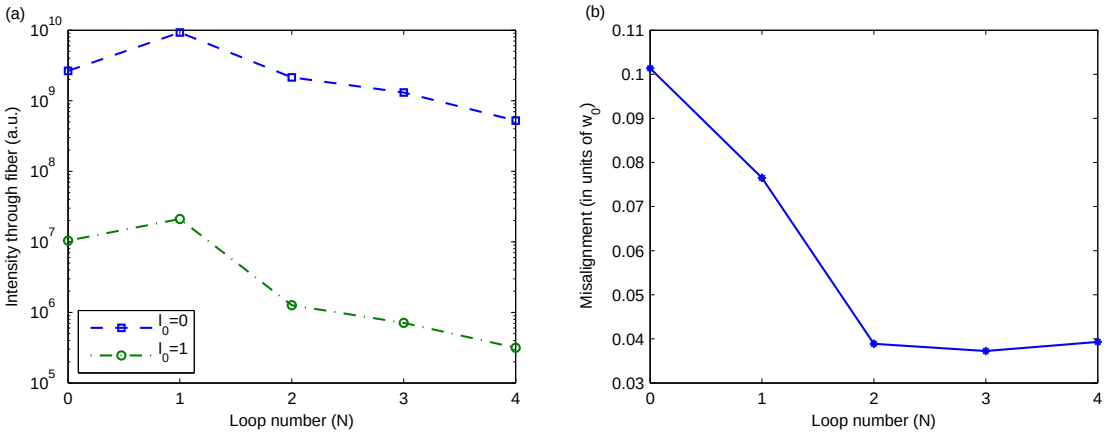

Figure 3.3: (a) Unnormalized power through the fibre versus the number of passes through the loop without a VPP and different initial OAM values ($\ell_0 = 0, 1$) set by the SLM. (b) Computed misalignment of SMF.

which are a complete orthonormal set of solutions to the paraxial wave equation. Each optical element operating on the pulse maps each LG mode into a different superposition of other LG modes. In particular, we focus on SMF, VPP and SLM. The remaining optics: mirrors, beam splitters, waveplates, etc. are insensitive to the transverse mode of the beam and thus preserve the LG mode. We then simulate the propagation of an input pulse through the spectrometer, and the coefficients of superposition obtained after the SMF corresponds to the measurement results.

3.4.1 Laguerre-Gaussian modes

The electric fields of LG modes can be described in cylindrical coordinates (ρ, ϕ, z) as [15]:

$$u_{\ell,p}(\rho,\phi,z) = \langle \rho,\phi,z|\ell,p\rangle = \frac{1}{w(z)}\sqrt{\frac{2}{\pi}\frac{p!}{(p+|\ell|)!}}\left(\frac{\sqrt{2}\rho}{w(z)}\right)^{|\ell|}\exp\left(-\frac{\rho^2}{w^2(z)}\right)L_p^{|\ell|}\left(\frac{2\rho^2}{w^2(z)}\right)\mathrm{e}^{\mathrm{i}\ell\phi}$$
$$\exp\left(\frac{\mathrm{i}k_0\rho^2 z}{2\left(z^2+z_\mathrm{R}^2\right)}\right)\exp\left(-\mathrm{i}(2p+|\ell|+1)\tan^{-1}\left(\frac{z}{z_\mathrm{R}}\right)\right) \quad (3.2)$$

Here $\ell\hbar$ ($\ell \in \mathbb{Z}$) is the OAM per photon, $p \geq 0$ labels the radial modes, $w(z)$ is the beam waist, z_R is Rayleigh range, and k_0 is the wave number of the fundamental Gaussian

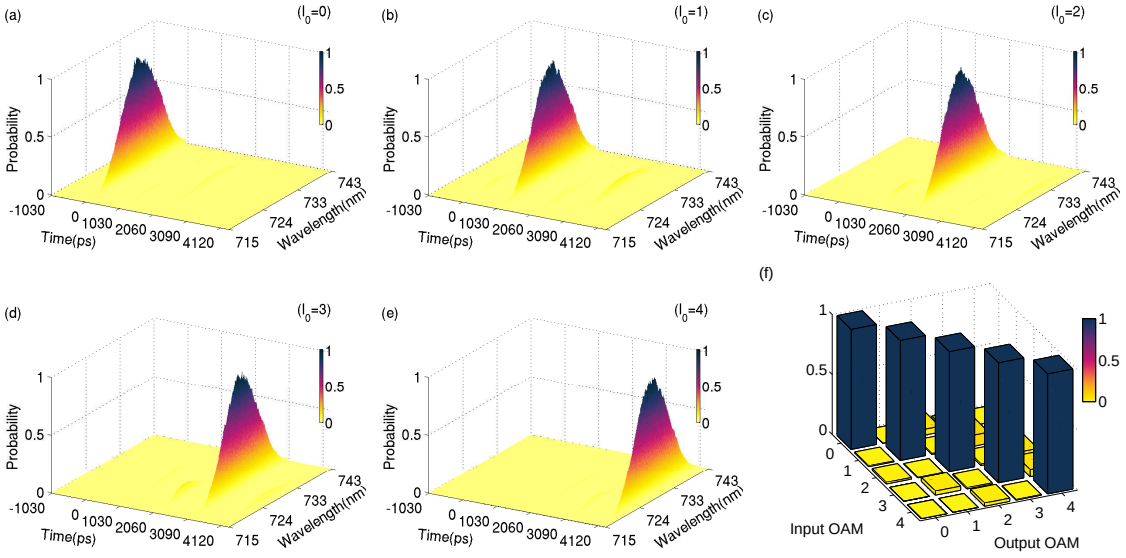

Figure 3.4: (a-e) Streak camera images for OAM eigenstates ($\ell = 0, 2, 4$) normalized based on (3.1). (f) Tabulated results of the OAM spectrometer up to $\ell = 4$.

mode.

3.4.2 Single mode fibre

Ideally, an SMF selects only the fundamental Gaussian mode ($\ell = 0, p = 0$) while all the other orthogonal spatial modes do not propagate through. In reality, higher order LG modes may still couple through the fibre due to finite apertures of optics and the fibre, imperfections of the fibre, mismatched beam waists between free-space and fibre-modes, and transverse misalignment between the propagation axes of the free-space and fibre-modes. In our experiments, the last effect, the transverse misalignment, is by far the dominant, while the other effects were too small to be measured. Hence we restrict our discussion to the transverse misalignment only. For a misalignment of Δ (in units of beam waist) between the two optical axes, the coupling efficiency of the LG beam (ℓ, p) through the SMF is given by (4.1.2):

$$|_{\Delta}\langle 0, 0|\ell, p\rangle|^2 = \frac{1}{p!(p+|\ell|)!}\left(\frac{\Delta^2}{2}\right)^{2p+|\ell|} \mathrm{e}^{-\Delta^2} \tag{3.3}$$

Experimentally, the above misalignment of the SMF can be estimated using the data for calibrating the energy distribution, as shown in figure 3.3(a). Nonzero output intensity from an input pulse of $\ell_0 = 1$ modes implies a misaligned (or imperfect) SMF. The amount of misalignment Δ can be calculated from the ratio of the two output intensities corresponding to the two input modes $\ell_0 = 0$ versus $\ell_0 = 1$ via:

$$\frac{P(\ell_0 = 1)}{P(\ell_0 = 0)} = \frac{|_\Delta\langle 0,0|M_{\text{VPP1}}|0,0\rangle|^2}{|_\Delta\langle 0,0|0,0\rangle|^2} \tag{3.4}$$

$$|_\Delta\langle 0,0|M_{\text{VPP1}}|0,0\rangle|^2 = \frac{\pi}{8}\Delta^2 \mathrm{e}^{-\frac{3}{2}\Delta^2}\left(I_0\left(\frac{\Delta^2}{4}\right) + I_1\left(\frac{\Delta^2}{4}\right)\right)^2 \tag{3.5}$$

The left hand side of (3.4) is measured experimentally. M_{VPP1} represents the operation by the SLM to create the input beam with $\ell_0 = 1$ and in a superposition of different p-states [133]. Equation (3.5) is obtained using (3.3) and (3.6) (See 4.1.3 for details). We plotted the derived misalignments in figure 3.3(b). The misalignment is less than 10.1% for all loops and converges to 3.7% for higher loop numbers, indicating only a minor accumulative loop misalignment.

3.4.3 VPP/SLM

The VPP and SLM are used to change the OAM state. The SLM, when applying the forked phase pattern, is mathematically equivalent to VPP for small diffraction angles [139, 140]. For a VPP of topological charge β, its operation on the laser beam can be described by a four-dimensional tensor $M_{VPP\beta}(z)$. We solve for the tensor elements $m_{\ell_1,p_1;\ell_2,p_2;\beta}(z)$

analytically (4.1.1) in the LG-mode basis:

$$m_{\ell_1,p_1;\ell_2,p_2;\beta}(z) = \left[\sqrt{\frac{p_1!p_2!}{(p_1+|\ell_1|)!(p_2+|\ell_2|)!}}\sum_{k=0}^{p_1}\sum_{m=0}^{p_2}(-1)^{k+m}\frac{(p_1+|\ell_1|)!}{(p_1-k)!(|\ell_1|+k)!k!}\right.$$
$$\left.\frac{(p_2+|\ell_2|)!}{(p_2-m)!(|\ell_2|+m)!m!}\,\Gamma\left(\frac{|\ell_1|+|\ell_2|}{2}+k+m+1\right)\right]$$
$$\left[\exp\left(\mathrm{i}(2(p_1-p_2)+|\ell_1|-|\ell_2|)\tan^{-1}\left(\frac{z}{z_\mathrm{R}}\right)\right)\right]$$
$$\left[\frac{\exp[2\pi\mathrm{i}(\ell_2+\beta-\ell_1)]-1}{2\pi\mathrm{i}(\ell_2+\beta-\ell_1)}\right] \quad (3.6)$$

This equation consists of a product of three terms denoted by square brackets. The first term with the double sum comes from the amplitude overlap between the different LG modes. The second term, consisting of an exponential, describes the effects of Gouy phases. The third term comes from OAM conservation and can describe the error in the topological charge of the VPP. We discuss the effect of each term below.

3.4.3.1 Gouy phase effects

Different LG modes have different Gouy phases which also vary differently as the beam propagates; therefore, whenever there is a superposition of modes, there can be interference effects between the modes that varies under free space propagation [121] and can lead to the loss of efficiency. However, the effect does not produce crosstalk between different ℓ-states, as OAM remain unchanged. In our experiment, the effect of the Gouy phase accounts for less than 0.05% loss in efficiency. This upper bound of 0.05% was calculated based on distances between the optics in the experimental setup and using (3.6). In general, the effect is negligible when the propagation distance is much smaller than the Rayleigh range ($z \ll z_\mathrm{R}$). When the size of the OAM spectrometer becomes comparable to the Rayleigh range, the use of 4-f systems between all phase elements would eliminate any Gouy phase effects.

3.4.3.2 Topological charge error

If the topological charge of the VPP is an integer, then the OAM of the beam is changed by that amount. If the laser's wavelength is different from the nominal wavelength of the VPP, or if the beam comes at a skew angle to the VPP, then the VPP will appear thicker or thinner. As a result, the OAM of the beam will be changed by a fractional value instead, or equivalently, become a superposition of LG modes of many OAM values. This leads to a loss in both the efficiency and fidelity of the OAM spectrometer.

Such topological charge error can be modelled by non-integer β in (3.6). In our experiment, both the laser wavelength and the angle of incidence are tightly controlled. Even if we consider a rather generous 0.5% error in the topological charge, it results in less than 0.05% loss of efficiency and less than -34dB crosstalk. Therefore the error in the topological charge is negligible.

3.4.3.3 Lateral misalignment

Although topological charge error will reduce the fidelity, it is, by far, not the leading cause. If the optical axes of the beam and VPP are displaced relative to each other, the VPP produces a superposition of not just p, but ℓ states [106] and thus reduces the fidelity. Such lateral misalignment of the VPP affects all three terms in (3.6). To model it, we first express the VPP tensor $M_\beta = \mathrm{e}^{\mathrm{i}\beta\phi}$ in a coordinate displaced from the common optical axis of the spectrometer. We then numerically evaluate $m_{\ell_1,p_1;\ell_2,p_2;\beta}(z)$ in a subspace of $\ell, p = [-7, 7] \times [0, 10]$. This chosen subspace yields less than 2% error on theoretical crosstalk.

To compare with the experimental result, we calculated the average crosstalk versus VPP misalignment, assuming a transverse misalignment of the SMF of 3.7% to 10.1% as obtained in 3.4.2. The results are shown in 3.5(a), where the x-direction corresponds to the direction of SMF misalignment. The measured crosstalk of -21.3 dB (3.3) corresponds to a VPP misalignment of 4.0% to 6.1% of the beam waist w_0. A larger (smaller) VPP

misalignment is allowed when its direction is aligned with (perpendicular to) that of the SMF misalignment.

3.4.4 Limiting factors of fidelity

In short, we show that misalignments of 3.7% to 10.1% at the SMF and 4.0% to 6.1% at the VPP are the leading causes for the loss of fidelity in our experiment, with an average crosstalk of -21.3 dB. Gouy phase effects do not affect fidelity and topological charge error contributes less than -34 dB to crosstalk.

The fidelity of the spectrometer can be further increased by improving the optical alignment at the VPP and SMF. We show in figure 3.5(b) the average crosstalk as a function of the VPP misalignment alone, neglecting SMF misalignment, and as a function of the SMF misalignment alone, neglecting VPP misalignment. It is more sensitive to VPP misalignment than to SMF misalignment, but decreases superlinearly with the reduction of either misalignment. With a VPP (SMF) misalignment of $< 1\%$, the crosstalk is reduced to < -34.4 dB (< -43.4 dB). When including both SMF and VPP misalignments, the crosstalk varies depending on the relative angle between the directions of the two misalignments. The crosstalk is the greatest when the misalignments are in perpendicular directions from each other. We show this upper bound crosstalk in 3.5(c). When the misalignments are in opposite directions, we generally see a reduction in crosstalk, sometimes up to 20 dB. Curiously, if the SMF is misaligned, crosstalk can be *decreased* by introducing some VPP misalignment, and vice versa. This is because with multiple elements misaligned, they can compensate each other. However, zero crosstalk is reached only when both misalignments are exactly zero.

As misalignment is reduced, other subtle effects will need to be taken under consideration. Such as imperfections in the surface roughness or other aberrations in the optics, which could further reduce efficiency and fidelity. Eventually, the fidelity will be limited by overlap in time between adjacent pulses. We did not include these effects in our model.

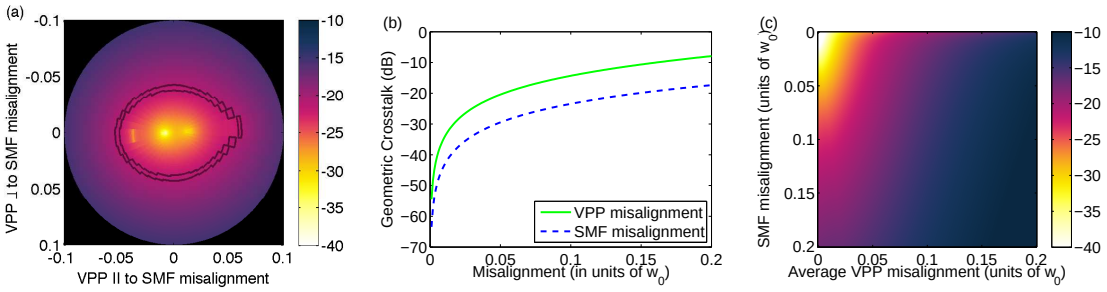

Figure 3.5: Calculated the geometric mean of crosstalk (in dB) as a function of the lateral misalignment of the SMF and VPP (normalized by w_0). (a) Crosstalk (in dB) as a function of the lateral misalignment of the VPP. SMF misalignment (measured in 3.3(c)) is taken along the x direction for convenience, since only the relative angle between VPP and SMF misalignment is important. The measured crosstalk of -20.9 to -21.6 dB corresponds to the values between the two black lines. (b) The crosstalk versus VPP misalignment with no SMF misalignment (green solid line), and the crosstalk versus SMF misalignment with no VPP misalignment (blue dashed line). (c) The upper bound of crosstalk (in dB) as a function of the SMF and VPP misalignments. The upper bound corresponds to when the directions of the SMF and VPP misalignments are perpendicular to each other. The crosstalk can be significantly reduced if the directions of the SMF and VPP lateral displacements are anti-parallel to each other.

3.5 Conclusions

In summary, we present a practical OAM spectrometer that can map OAM to time up to arbitrarily large OAM values. We have shown an average nearest neighbor crosstalk of -21.3dB among 5 OAM states, limited mainly by optical misalignment. The high fidelity of the demonstrated OAM spectrometer may enable accurate measurements of topological properties of objects such as in spiral imaging [94] and the angular momentum of black holes, which is encoded into the OAM spectrum of light from the accretion disc due to strong gravitational effects predicted by general relativity [113]. We also demonstrated speeds (80 MHz) orders of magnitude faster than the switching times of SLMs. Miniaturization of optics could allow for GHz detection rate.

CHAPTER 4

Effects of misalignment on Orbital Angular Momentum

This this chapter, I will provide additional mathematical background for working with OAM states. This is mostly derived from the appendix from the paper fellow students Minho Kwon and Connor Roncaioli assisted with. Additional support and funding provided by Hui Deng [166].

4.1 Define overlap integrals

In this appendix section we seek to derive the various actions and overlaps between the LG modes and optics. We first derive the action of the VPP in the LG basis. Then we derive the overlap of any LG mode with a misaligned SMF. Lastly, we derive the overlap of OAM states created by a VPP with a misaligned SMF. This is done by explicit integration and definitions of various special functions. We use the inner product between Laguerre-Gaussian modes defined in 3.2 in cylindrical coordinates:

$$\begin{aligned}\langle \ell_1, p_1 | \ell_2, p_2 \rangle &= \int_0^\infty \rho \mathrm{d}\rho \int_0^{2\pi} \mathrm{d}\phi \langle \ell_1, p_1 | \rho, \phi, z \rangle \langle \rho, \phi, z | \ell_2, p_2 \rangle \\ &= \int_0^\infty \rho \mathrm{d}\rho \int_0^{2\pi} \mathrm{d}\phi u^*_{\ell_1, p_1}(\rho, \phi, z) u_{\ell_2, p_2}(\rho, \phi, z) \end{aligned} \tag{4.1}$$

4.1.1 Derivation of VPP tensor

We derive the four dimensional tensor of the action of a VPP in the LG basis as seen in (3.6). We start by explicitly writing down the overlap integral:

$$\langle \ell_1, p_1 | M_{\mathrm{VPP}_\beta} | \ell_2, p_2 \rangle = \int_0^\infty \rho \mathrm{d}\rho \int_0^{2\pi} \mathrm{d}\phi LG^*_{\ell_1,p_1}(\rho,\phi) \mathrm{e}^{+\mathrm{i}\beta\phi} LG_{\ell_2,p_2}(\rho,\phi) \tag{4.2}$$

The LG functions are given by (3.2). Due to separability of variables, we will solve the ϕ-integral first:

$$\int_0^{2\pi} \mathrm{d}\phi \mathrm{e}^{-\mathrm{i}\ell_1\phi} \mathrm{e}^{+\mathrm{i}\beta\phi} \mathrm{e}^{+\mathrm{i}\ell_2\phi} = \frac{\exp\left(2\pi\mathrm{i}\left(\ell_2+\beta-\ell_1\right)\right)-1}{\mathrm{i}\left(\ell_2+\beta-\ell_1\right)} \tag{4.3}$$

In the limit where β is an integer, the ϕ-integral yields the OAM conserving solution of $2\pi\delta_{\ell_1+\beta-\ell_2,0}$, where $\delta_{a,b}$ is the Kronecker delta. The remaining ρ-integral is found by expanding the rest of the LG modes and the generalized Laguerre polynomials given by (4.4). This yields a finite polynomial of degree $|\ell_1|+|\ell_2|+2p_1+2p_2+1$ (the +1 is from the Jacobian) multiplied by the Gaussian function $\exp\left(\frac{-\rho^2}{2w_0^2}\right)$. This integral can be easily solved by using one of the definitions of the Gamma function as shown in (4.5) to yield the result in the text (3.6).

$$L_p^k(x) = \sum_{m=0}^{p} (-1)^m \frac{(p+k)!}{(p-m)!(k+m)!m!} x^m \tag{4.4}$$

$$\int_0^\infty \mathrm{d}x x^k \mathrm{e}^{-x^2} = \frac{1}{2}\Gamma\left(\frac{1+k}{2}\right) \tag{4.5}$$

4.1.2 Overlap between fundamental Gaussian and Laguerre-Gaussian

We first derive the overlap between a misaligned fundamental Gaussian mode and generic higher order LG modes. This is (3.3) in the text. We start with the fundamental Gaussian mode defined in cylindrical coordinates (ρ, ϕ, z) with an origin shifted by $w_0\Delta$ along the $\phi = 0$ direction. The propagation direction is along the z-axis.

$$ {}_{\Delta}\langle 0,0|\rho,\phi,z\rangle = \frac{1}{w_0}\sqrt{\frac{2}{\pi}}\exp\left(\frac{-\left(\rho^2+2\rho w_0\Delta\cos\phi+w_0^2\Delta^2\right)}{w_0^2}\right) \tag{4.6} $$

If the origin were shifted along a different ϕ angle, the only change would be the overall phase which does not affect the intensity. These calculations are performed at the beam waist since the beam should be focused on the fibre to have any substantial coupling. With a change of variables $x = \frac{\sqrt{2}\rho}{w_0}$ the complete overlap integral is now:

$$ {}_{\Delta}\langle 0,0|\ell,p\rangle = \int_0^{\infty}\int_0^{2\pi} x\mathrm{d}x\mathrm{d}\phi\frac{1}{\pi}\sqrt{\frac{p!}{(p+|\ell|)!}}x^{|\ell|}\exp\left(\frac{-x^2}{2}\right)L_p^{|\ell|}\left(x^2\right)\mathrm{e}^{\mathrm{i}\ell\phi} \exp\left(-\left(\frac{x^2}{2}+\sqrt{2}x\Delta\cos\phi+\Delta^2\right)\right) \tag{4.7} $$

The ϕ-integral is related to the well known Bessel integral (4.8), so (4.7) becomes (4.9).

$$ J_n(z) = \frac{1}{2\pi\mathrm{i}^n}\int_0^{2\pi}\mathrm{d}\phi\mathrm{e}^{\mathrm{i}z\cos\phi}\mathrm{e}^{\mathrm{i}n\phi} \tag{4.8} $$

$$ {}_{\Delta}\langle 0,0|\ell,p\rangle = \sqrt{\frac{p!}{(p+|\ell|)!}}\int_0^{\infty} x\mathrm{d}x x^{|\ell|}\mathrm{e}^{-\left(x^2+\Delta^2\right)}L_p^{|\ell|}\left(x^2\right)2\mathrm{i}^{-|\ell|}(-1)^{|\ell|}J_{|\ell|}\left(\mathrm{i}\sqrt{2}\Delta x\right) \tag{4.9} $$

The Bessel function can be converted into an infinite sum of generalized Laguerre polynomials as given in (4.10) below with $\sqrt{w} = \mathrm{i}\Delta/\sqrt{2}$. Using (4.10) and the orthogonality

relationship between generalized Laguerre polynomials (4.11). Equation (4.9) magnitude squared surprisingly reduces to the rather simple expression of (3.3) in the text.

$$\sum_{n=0}^{\infty} \frac{L_n^k(x)}{\Gamma(n+k+1)} w^n = e^w (xw)^{\frac{-k}{2}} J_k\left(2\sqrt{xw}\right) \tag{4.10}$$

$$\int_0^{\infty} \mathrm{d}x \mathrm{e}^{-x} L_n^k(x) L_m^k(x) = \frac{(n+k)!}{n!} \delta_{m,n} \tag{4.11}$$

4.1.3 Overlap between fundamental Gaussian and vortex phase plate mode

We create states with OAM by passing a Gaussian beam through a VPP. This state can be expressed as a sum of Laguerre Gaussian modes as given in (4.12), which is a special case of the more general equation solved in section 4.1.1. In the previous section, we calculated the overlap of a shifted fundamental Gaussian mode and any Laguerre Gaussian mode. Therefore, by combining these two calculations, we can derive the overlap of a shifted Gaussian mode and an OAM mode created by a VPP (4.13), here $z = \frac{\Delta^2}{2}$.

$$M_{\text{VPPN}}|0,0\rangle = \sum_{p=0}^{\infty} m_{0,0;N,p;N}|N,p\rangle \tag{4.12}$$

$$\text{where } m_{0,0;N,p;N} = \frac{N}{2}\sqrt{\frac{1}{(p+N)!}}\Gamma\left(p+\frac{N}{2}\right)$$

$${}_{\Delta}\langle 0,0|M_{\text{VPPN}}|0,0\rangle = \frac{e^{-z} z^{\frac{N}{2}} (-1)^N N}{2} \sum_{p=0}^{\infty} \frac{(-z)^p \Gamma\left(p+\frac{N}{2}\right)}{(p+N)!p!} \tag{4.13}$$

Equation (4.13) can be written in the form of a regularized confluent hypergeometric function (4.14) which can be evaluated using (4.15)[1] to yield the result in (4.16), where $I_\alpha(x)$ is the modified Bessel function of the first kind. The expression can be further simplified by noting $I_\alpha(-z) = \mathrm{i}^{2\alpha} I_\alpha(z)$. In the case of $N = 1$ and taking the magnitude squared, this reduces to the form in the text (3.5).

$$ {}_1\tilde{F}_1(a; b; z) = \sum_{k=0}^{\infty} \frac{\Gamma(a+k)}{\Gamma(b+k)\Gamma(a)} \frac{z^k}{k!} \tag{4.14} $$

$$ {}_1\tilde{F}_1\left(\frac{N}{2}; N+1; z\right) = \frac{e^{\frac{z}{2}}\sqrt{\pi}}{2\Gamma\left(\frac{N}{2}+1\right)} z^{\frac{1}{2}-\frac{N}{2}} \left(I_{\frac{N}{2}-\frac{1}{2}}\left(\frac{z}{2}\right) - I_{\frac{N}{2}+\frac{1}{2}}\left(\frac{z}{2}\right)\right) \tag{4.15} $$

$$ \frac{\mathrm{e}^{\frac{-3\Delta^2}{4}} \Delta^2 \sqrt{\pi}}{2\sqrt{2}} \left(I_{\frac{N}{2}-\frac{1}{2}}\left(\frac{\Delta^2}{4}\right) + I_{\frac{N}{2}+\frac{1}{2}}\left(\frac{\Delta^2}{4}\right)\right) \tag{4.16} $$

[1] http://functions.wolfram.com/07.21.03.0011.01

CHAPTER 5

A Compact Orbital Angular Momentum Spectrometer Using Quantum Zeno Interrogation

In this paper, we present a compact OAM-spectrometer comprising of only one interferometer nested within an optical loop (Figure 5.1). It uses a Quantum Zeno Interrogator (QZI) [168, 169, 159] (shaded region in Figure 5.1) to perform counterfactual measurements on the OAM state, and thus maps different OAM components of an arbitrary input light pulse into different time bins at the output. It can achieve very high extinction ratios between different OAM states and can work for arbitrarily high OAM orders limited mainly by optical losses. Funding and support provided for by Hui Deng [160].

5.1 Setup

We illustrate now how the spectrometer works by tracing, as an example, a horizontally polarized input pulse with an OAM value $l = l_0 \geq 0$, noted as $|\psi^{(0)}\rangle = |H, l_0\rangle$. The input pulse first transmits through optical switches S0 and S1 [1], and enters the QZI. The

[1] S0 and S1 are optical switches that can be switched from been transmissive to reflective. S0 needs to transmit the initial incident light, and be switched to be reflective by the end of the first outer-loop cycle. A high repetition rate is not required and it can be implemented either mechanically or opto-electrically.

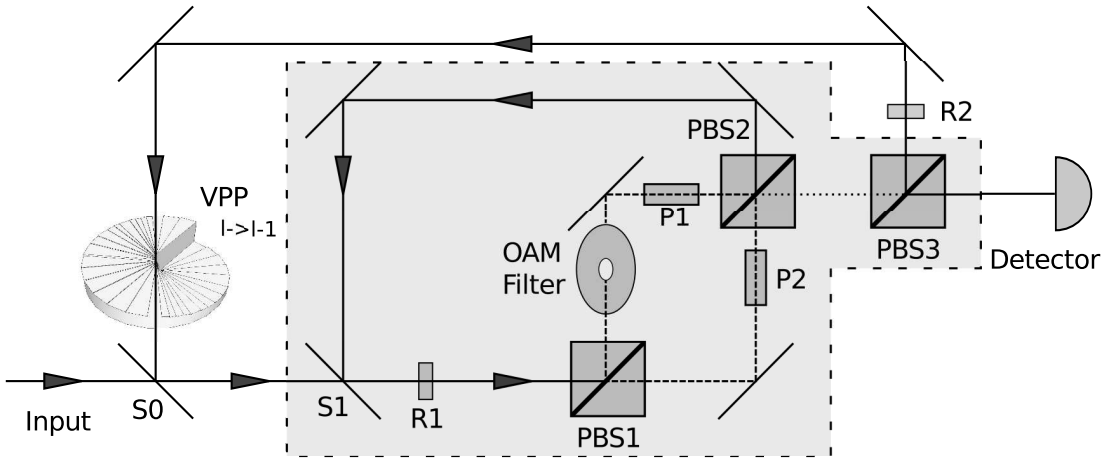

Figure 5.1: A schematic of the compact OAM spectrometer. The Quantum Zeno Interrogator (shaded region) distinguishes between zero and nonzero OAM states. The outer loop decreases the OAM value of light by one per round trip. All the beam splitters are polarizing beam splitters (PBSs) that transmits horizontally polarized light and reflects vertically polarized light. The OAM filter transmits states with zero OAM, but blocks states with non-zero OAM. S0 and S1 are switching mirrors that either transmits or reflects incident light. R1 and R2 are fixed polarization rotators, which can be half wave plates. P1 and P2 are fast polarization switches, such as Pockels cells. When activated, P1 and P2 switches horizontal polarization to vertical and vice versa. When de-activated, they are transparent to light. The shaded region is a Quantum Zeno Interrogator which separates OAM components with $l = 0$ and $l \neq 0$ into different polarizations. Hence at PBS3, zero OAM component is sent to the detector while the none-zero OAM component is sent back into the outer-loop. The outer loop decreased OAM by one per round trip via, for example, a vortex phase plate.

polarization rotator R1 rotates its polarization by $\Delta\theta = \pi/(2N)$, and the state becomes $|\psi_1^{(0)}\rangle = \cos\left(\frac{\pi}{2N}\right)|H, l_0\rangle + \sin\left(\frac{\pi}{2N}\right)|V, l_0\rangle$. If $l = 0$, the horizontal and vertical components of $|\psi_1^{(0)}\rangle$ passes through the lower and upper arms of the interferometer, respectively. They recombine into the same state $|\psi_1^{(0)}\rangle$ at the polarizing beam splitter PBS2 (neglecting an overall phase factor). S1 is switched to be reflective at the end of the first QZI loop, and the combined beam continues to loop in the QZI. The polarization is rotated by $\Delta\theta = \pi/(2N)$ each loop. After N loops, the light becomes vertically polarized and enters only the upper path of the interferometer. At this point, the polarization switch P1 is activated and switches

Alternatively it could also be a static high-reflectance mirror, if the one-time transmission loss at the very beginning can be tolerated. S1 needs to be switched every QZI loop cycle (ΔT) and need to be polarization insensitive.

the polarization into horizontal. Hence the light transmits through both PBS2 and PBS3, and arrives at the detector at time T_0.

If $l_0 \neq 0$, however, the vertical component is sent to the upper path at PBS1, and is then blocked by the OAM filter. Only the horizontal component emerges after PBS2, the state collapses into $|H, l_0\rangle$ with a probability $\cos^2\left(\frac{\pi}{2N}\right)$. After N loops, a fraction $p = \cos(\pi/(2N))^{2N}$ of the light remains in the horizontal polarization in the lower arm of the interferometer, while a fraction $1 - p$ of the light is lost (blocked by OAM filter). At this point, the polarization switch P2 is activated and switches the polarization to vertical, and the light reflects off both PBS2 and PBS3, and enters the outer loop. By this time, S0 is switched to be reflective. As the light cycles in the outer loop, the polarization in rotated back to horizontal by R2, and the OAM value is decreased by $\Delta l = 1$ per cycle by a vortex phase plate (VPP) [137]. After l_0 cycles, $l = 0$. When the light enters the QZI again, it will exit the spectrometer to the detector, at a time $T(l_0) = T_0 + l_0(NL_{QZI} + L_{out})/c$. Here L_{QZI} and L_{out} are the optical path lengths of the QZI loop (from S1 to PBS2 back to S1) and the outer-loop (from S1 to PBS2, to PBS3, to S0, back to S1). The detected fraction of the light intensity is $P(l_0) = p^{l_0} = \cos\left(\frac{\pi}{2N}\right)^{2Nl_0}$.

In short, the OAM spectrometer sorts different OAM components into different time intervals separated by $\Delta T = (NL_{QZI} + L_{out})/c$ with a *perfect* extinction ratio. The total transmission efficiency of the spectrometer is $P(l_0)$ for the component with OAM of $l_0\hbar$. $P(l_0) \to 1$ for all l_0 as $N \to \infty$ due to the quantum Zeno effect [170], as shown in the Figure 5.2(a).

In practice, optical components introduce loss. Assuming high quality, but commercially available optical components, we estimate a round trip transmission of $|\alpha|^2 \sim 0.96$ per cycle[2] for both the outer loop (α_{out}), the QZI loop (α_{QZI}) and initial and final optics ($\alpha_{init,final}$). Hence the total transmission efficiency of the OAM spectrometer becomes

[2]Technically, each $|\alpha|^2$ is slightly different, but the difference is well within 1%. The $|\alpha|^2$ that matters most is the one corresponding to the QZI loop (including S1), which, without any optimization, consists of 4 beam splitters, 5 mirrors, 1 waveplate and up to three Pockels cells. Assuming all optics are anti-reflection coated so that loss is 1% at each Pockels cell and 0.1% at each other component, we have $|\alpha|^2 \geq 0.96$.

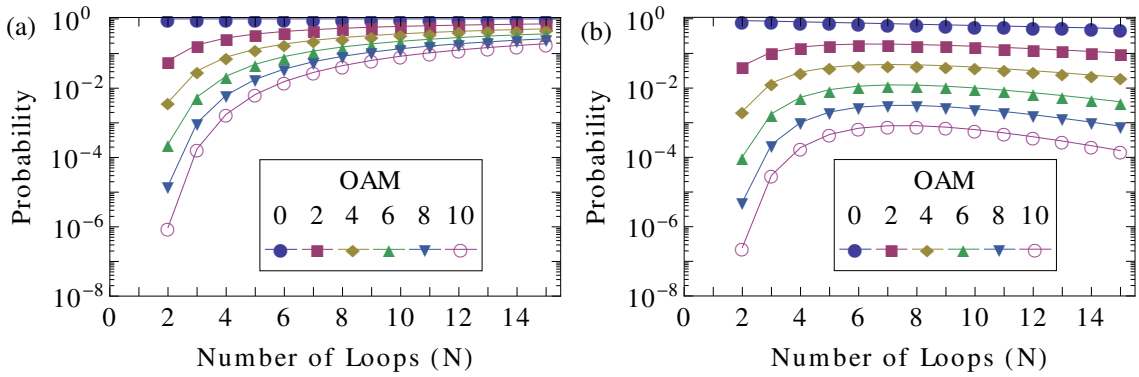

Figure 5.2: The probability of detecting the correct OAM value as a function of the number of loops (N) in the QZI using a perfect OAM filter. (a) Neglect optical loss. (b) Assume $|\alpha|^2 = 0.96$ based on commercially available optics. When optical loss is included, there exists an optimal N for higher order OAM states, due to the compromise between the quantum Zeno enhancement and optical loss.

$P(l_0) \approx \alpha^{(2N+2)(l_0+1)} \cos\left(\frac{\pi}{2N}\right)^{2Nl_0}$ for the l_0-th order OAM component. We plot in Figure 5.2(b) the $P(l_0)$ vs. N for OAM components $l_0 = 0 - 10$. With increasing N, the quantum Zeno effect leads to an increase in $P(l_0)$, while loss leads to a decrease in $P(l_0)$. As a result, an optimal N is found at about $7 - 8$ for high order OAM components. Note that the extinction ratio between different OAM states remains infinite even in the presence of loss. Crosstalk would only take place when the OAM filter is not completely opaque to nonzero OAM states.

5.2 Imperfect OAM Filters

To take into account imperfect OAM filters, we derive below the general expression for the transmission efficiency and extinction ratio, with finite N and optical loss. We consider the OAM filter having a complex transmission coefficient $\sqrt{T(l)}e^{i\phi(l)}$ for the lth OAM component. If the state $|\psi\rangle = |H, l_0\rangle$ enters the QZI, after N cycles, it exits the QZI loop in a polarization superposition state $p_H|H\rangle + p_V|V\rangle$ [171], where p_H and p_V are given by:

$$\begin{pmatrix} p_H \\ p_V \end{pmatrix} = \alpha_{QZI}^N \left[\begin{pmatrix} 1 & 0 \\ 0 & \sqrt{T(l)}e^{i\phi(l)} \end{pmatrix} \begin{pmatrix} \cos\left(\frac{\pi}{2N}\right) & \sin\left(\frac{\pi}{2N}\right) \\ \sin\left(\frac{\pi}{2N}\right) & -\cos\left(\frac{\pi}{2N}\right) \end{pmatrix} \right]^N \begin{pmatrix} 1 \\ 0 \end{pmatrix}. \tag{5.1}$$

The pulse re-enters the outer loop at PBS3 with probability $|p_H|^2$, corresponding to a successful interrogation by the QZI (if $l_0 \neq 0$). With probably $|p_V|^2$, the pulse exits toward the detector, corresponding to an error (if $l_0 \neq 0$). The total loss of this QZI interrogation is $|loss|^2 = 1 - |p_H|^2 - |p_V|^2$. In the outer loop, the OAM value of the pulse is lowered by 1 via the VPP, and the intensity of the pulse is reduced by a factor $|\alpha_{out}|^2$ per loop. Therefore, the probability of detecting the OAM eigenstate l_0 in the lth time interval (or, measured as with OAM $l\hbar$) is given by:

$$P(l; l_0) = |\alpha_{init,final}|^2 |p_V(l_0 - l)|^2 \prod_{m=l_0-l+1}^{l_0} \left(|\alpha_{out}|^2 |p_H(m)|^2\right). \tag{5.2}$$

And we define the extinction ratio η as:

$$\eta(l_0) = P(l_0; l_0) / \sum_{l \neq l_0} P(l; l_0). \tag{5.3}$$

With an imperfect OAM filter, light with nonzero OAM has a finite probability of transmitting through the filter in vertical polarization after the Nth QZI-loop. It will then be switched to horizontal polarization by P1 and exit at a time interval corresponding to components with a lower OAM. Consequently, the extinction ratio is reduced. If the light is transmitted through the filter before the Nth loop, it will results in a larger loss. An imperfect OAM filter may also partially block light with zero OAM, which which also results in loss.

Figure 5.3(a) shows, per quantum Zeno interrogation of light with OAM of $l\hbar$, the probabilities of the light exiting toward the detector ($|p_V|^2$), re-entering the outer-loop ($|p_H|^2$)

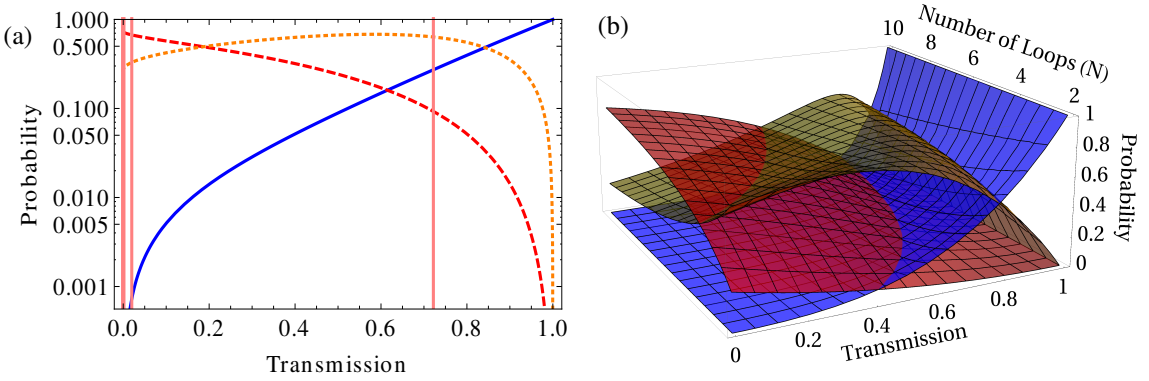

Figure 5.3: The probabilities of different outcomes of a QZI interrogation as a function of the transmission of the OAM filter, neglecting optical loss. The blue solid line represents detecting OAM=0, the red dashed line is detecting OAM$\neq 0$, and the orange dotted line, loss. (a) $N = 8$. (b) $N = 2 - 10$.

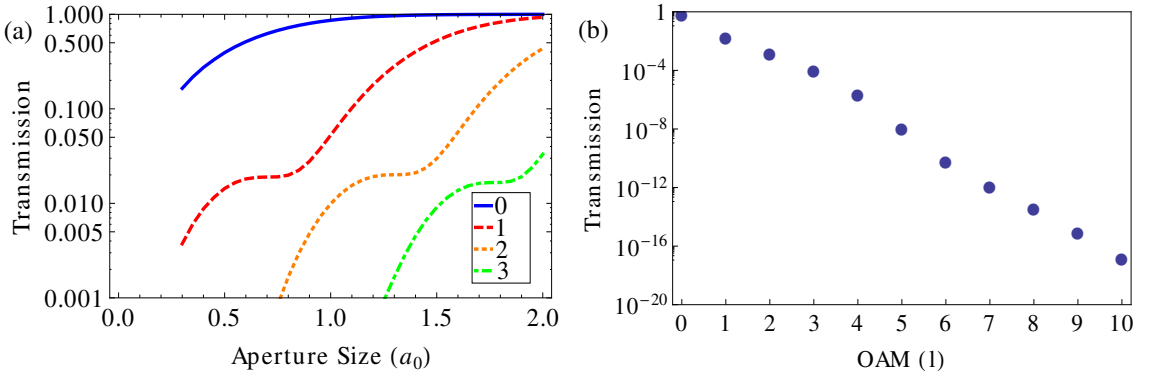

Figure 5.4: Transmission of the pinhole spatial filter (a) as a function of the normalized aperture size a_0, for OAM components with $l_0 = 0 - 3$ and (b) as a function of l_0 with $a_0 = 0.8$.

and being lost ($1 - |p_V|^2 - |p_H|^2$). These probabilities are plotted as a function of transmission $T(l, a_0)$ and N. The crossing of $|p_H|^2$ and $|p_V|^2$ separates the regimes when the interrogation result is more likely (to the right side) or less likely (to the left side) to be correct than incorrect.

5.3 Pinhole spatial filter

As a practical example of an imperfect OAM filter, we consider a pinhole spatial filter. Light with OAM of $l\hbar \neq 0$ has zero intensity at the center of the beam, while light without

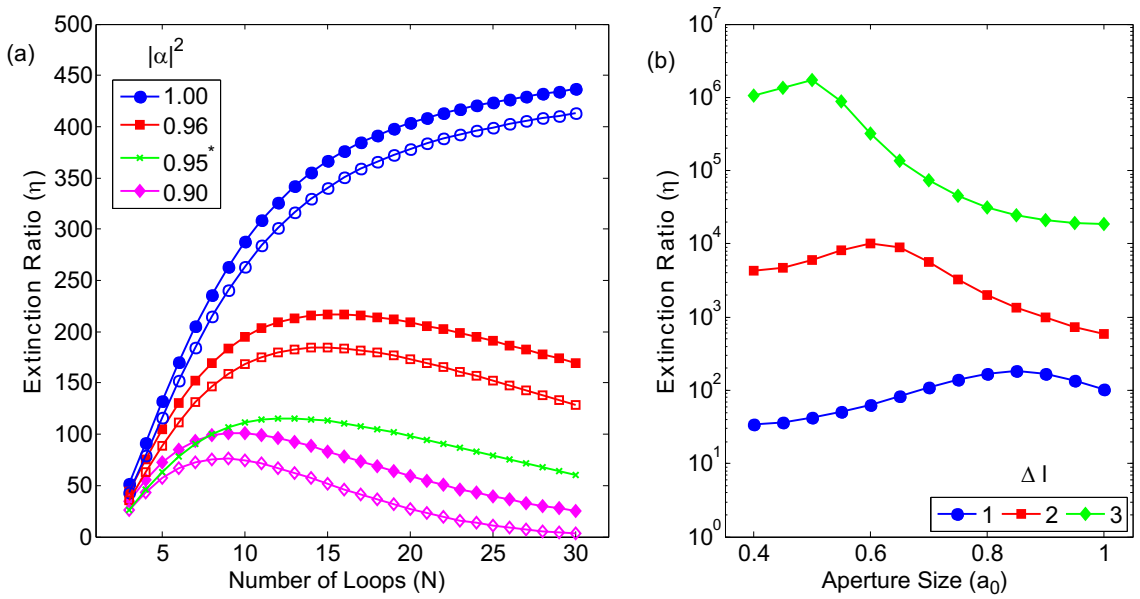

Figure 5.5: (a) Extinction ratio η as a function of the number of loops N for various losses $|\alpha|^2$. Solid symbols are for $l_0 = 1$ and open symbols are for $l_0 = 3$. $l_0 > 3$ are essentially indistinguishable from $l_0 = 3$. For the $l_0 = 0$ case, the extinction ratio is over a 1000 for all $|\alpha|^2$ values because no premature measurements are possible. The additional green crosses labeled as $|\alpha|^2 = 0.95^*$ represents $|\alpha|^2 = 0.96$ but including misalignment of the OAM filter and VPP as discussed in the text. (b) Extinction ratio η as a function of the normalized aperture size a_0 for $l_0 = 6$, $\Delta l = 1 - 3$, $N = 8$, and $|\alpha|^2 = 0.96$. Skipping OAM states increases the extinction ratio by orders of magnitude.

OAM has maximum intensity at the center. Hence a very simple pinhole efficiently distinguishes light with and without OAM. The intensity distribution of a Laguerre-Gaussian beam, a paraxial beam possessing OAM $l\hbar$, is given by [6]:

$$I_{LG}(l;\rho) = \frac{I_0}{\int_0^\infty du u^{|l|} e^{-u} L_{|l|}(u)} \left(\frac{\sqrt{2}\rho}{w_0}\right)^{|l|} L_{|l|}\left(\frac{2\rho}{w_0^2}\right) e^{-\frac{\rho^2}{w_0^2}} \tag{5.4}$$

Where $L_l(x)$ is the lth order Laguerre Polynomial. Thus the transmission $T(l)$ through a pinhole with a radius a_0 (normalized by the waist of the $l_0 = 0$ Gaussian beam) is:

$$T(l, a_0) = \int_0^{a_0} \int_0^{2\pi} \rho d\rho d\phi I_{LG}(l;\rho) \Big/ \int_0^{\infty} \int_0^{2\pi} \rho d\rho d\phi I_{LG}(l;\rho) \tag{5.5}$$

Figure 5.4(a) shows $T(l, a_0)$ vs. a_0 for $l = 0 - 3$. The transmission decreases sharply

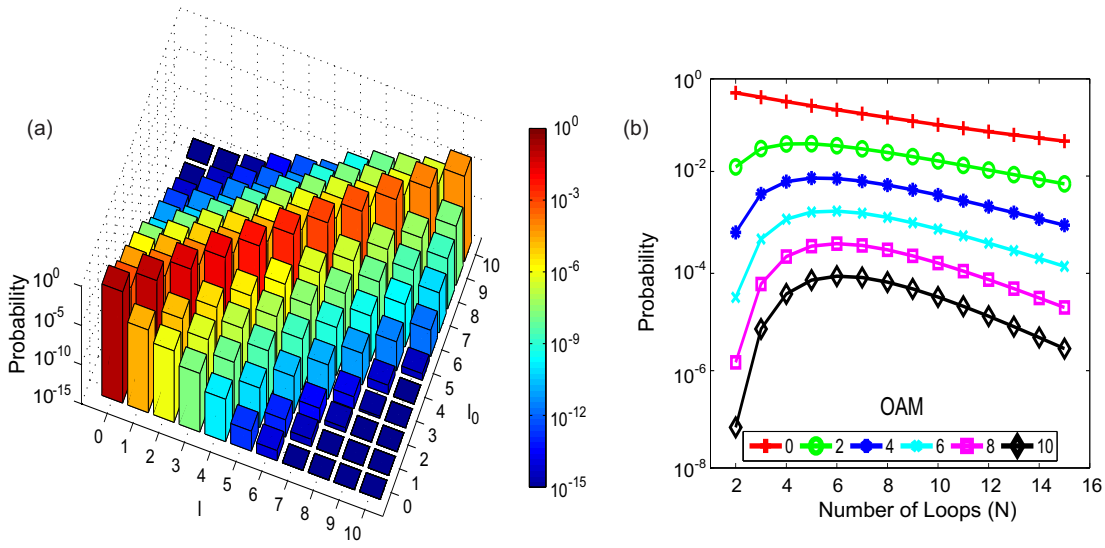

Figure 5.6: (a)The probability of measuring an OAM value l for a given input state l_0 (Equation 5.2), using pinhole as the OAM filter, $N = 8$, $|\alpha|^2 = 0.96$, and misalignment of 10% and 1%, respectively, at the pinhole filter and VPP. Despite the decrease in probability for the diagonal elements at large l_0, the off diagonal elements decrease much faster, as implied by the large extinction ratios. (b) The diagonal elements of (a) as a function of N for $l_0 = 0 - 10$.

with increasing l when a_0 is smaller than ~ 0.8. Choosing $a_0 = 0.8$, we show in Figure 5.4(b) the nearly exponential decrease of $T(l, a_0)$ with l. These values are also marked by the red vertical lines in Figure 5.3(a). Due to the fast decrease of $T(l, a_0)$ from $l = 0$ to $l \geq 1$, a large extinction ratio is readily achieved, which is very well approximated by:

$$\eta(l_0) = P(l_0; l_0) / \sum P(l \neq l_0; l_0) \approx \frac{\alpha_{out} |p_V(0)|^2 |p_H(1)|^2}{|p_V(1)|^2}. \tag{5.6}$$

η is essentially the same for all OAM components, and it is mainly determined by how well the QZI can distinguish between states with OAM values $l_0 = 0$ and $l_0 = 1$. We plot in Figure 5.5(a) η vs. N for $|\alpha|^2 = 0.9 - 1$. In general, η increases with N but decreases with $|\alpha|^2$, resulting in an optimal N for each $|\alpha|^2 < 1$. Even for $|\alpha|^2 = 0.9$, $\eta > 70$ can be reached with $N = 7$. For $|\alpha|^2 = 0.96$, η peaks at ~ 180.

5.4 Discussion of results

An additional source of error is due to the misalignment of the beam through two OAM-sensitive components: the OAM filter (e.g. a pinhole) and the VPP. Misalignment at the pinhole filter leads to reduced coupling efficiency of the zero OAM state, increased transmission of non-zero OAM states, and thus reduced extinction ratio. Misalignment on the VPP changes the desired OAM state into a superposition with neighboring OAM orders. However, these neighboring orders have very small amplitudes (e.g. $< 1\%$ with 1% misalignment) [106], and they are further filtered out through the QZI loop, resulting in negligible reduction in the extinction ratio. The main effect of misalignment at VPP is the slightly reduced transmission of the correct OAM state, hence reduced overall detection probability. We illustrate the effects of misalignment on the extinction ratio in Figure 5.5(a) (the green crosses), assuming conservatively 10% misalignment of the focused beam waist at the pinhole and 1% misalignment of the collimated beam waist at the VPP. Extinction ratios over 100 are still readily achieved.

The extinction ratio can be increased by many orders of magnitude if we only need to measure every other order, or every third order of OAM (Figure 5.5(b)). Correspondingly, we can choose smaller aperture sizes and a VPP that reduces the l by $\Delta l = 2$ or 3 per passing. A smaller aperture size also introduces extra loss, but only in the final QZI on the zero OAM state, and thus only decreases the detection probability by about a factor of two.

To evaluate the overall performance of the OAM spectrometer, we plot in Figure 5.6(a) $P(l; l_0)$ vs. l and l_0 on the log scale, including loss and misalignment. The diagonal elements $P(l_0; l_0)$ correspond to correctly detecting an OAM component. They are two orders of magnitude higher than neighboring off diagonal elements, consistent with the high extinction ratios calculated before. In Figure 5.6(b), we show $P(l_0; l_0)$ as a function of N for different l_0. $N \sim 8$ gives the highest probability for detecting high order OAM components, while still maintaining an extinction ratio of above 100.

5.5 Conclusions

In summary, we present a compact OAM spectrometer that disperses light of different OAM values in time. Loss is significant for high order OAM components with commercially available optical components. However, the high loss doesn't have an appreciable effect on the signal to noise ratio; extinction ratios of > 100 are readily achieved even after taking into account optical loss and misalignments. The extinction ratio can be further improved by many orders of magnitude by skipping OAM orders, or by using a better OAM filter than a simple pinhole.

CHAPTER 6

Generalized Quantum Zeno Interrogation

6.1 Original Quantum Zeno Interrogation

The original quantum Zeno interrogator (QZI) was created and demonstrated by Kwiat *et al.* to detect the presence of an absorbing object without directly interacting with it [159]. The concept of the original QZI was used in Chapter 5 [160]. In this introductory section, I will discuss operation principle of the QZI in more detail, in preparation how to generalize it.

The original QZI requires the light to have at least a two dimensional Hilbert space in order to non-destructively probe the state of an object (transparent versus opaque). Because the dimension is only two, and unambiguous results as desired, only a single bit of information can be discerned from the object — either the object is opaque or it is not. In the case of partially transparent objects [171] the final result will be a superposition of the two orthogonal states of the Hilbert space.

The quantum Zeno interrogator works by creating an optical loop for a set number of iterations (N). The input beam is horizontally polarized and the polarization is slowly rotated by $\theta = \frac{1}{2N}$ from horizontal to vertical. As seen in Figure 6.1, the beam continues onward to a polarizing beam splitter with object to be probed in the vertical arm. If there is *not* an object (or the object is transparent), then the system will cycle for N times and the collective rotations will build up and the light will end up vertically polarized. Vertical

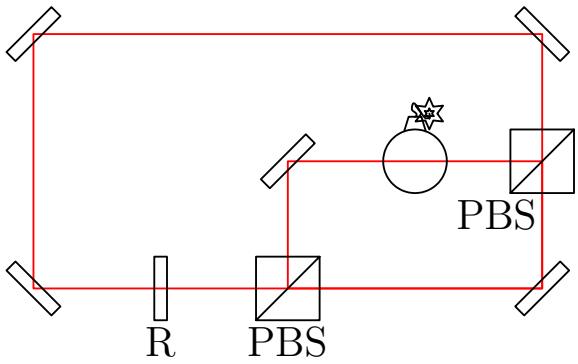

Figure 6.1: This is the original quantum Zeno interrogator using polarization to non-destructively probe the state of a single bomb. If the bomb is working (opaque, absorb photon), then the photon will be horizontally polarized with some chance of loss. If the bomb is a dud (transparent), then the photon will be vertically polarized with no chance of loss (assuming perfect optics). The chance of loss can be made arbitrarily small.

polarization will be an indicator that there is no object (or the object is transparent). If there is an object (and it is opaque), then the photon, which is in a superposition of vertical and horizontal polarization after the first polarizing beam splitter will collapse to one of the two paths. There is a $\sin^2\left(\frac{\pi}{2N}\right)$ probability that the photon is absorbed by the object, and the remaining probability that the photon simply "resets" to horizontal polarization (hence the name Quantum Zeno). After N cycles, there is a $1-\cos^{2N}\left(\frac{\pi}{2N}\right)$ chance of absorption, otherwise the photon is horizontally polarized - which will be used as an indicator that there is an object (and it is opaque). Note, as N becomes arbitrarily large, the probability of absorption tends to 0. For amplitude transmission t with N loops, the probability of vertical (P_V) and horizontal (P_H) polarization is given in Equation 6.1[1]. Note, if the object is perfectly transparent or perfectly opaque, while there is a chance for complete loss, in the event of no loss, then the result is completely unambiguous. Moreover, in the event of no loss, it is possible to determine if the object is opaque without losing the photon.

$$\begin{pmatrix} P_H \\ P_V \end{pmatrix} = \left| \left[\begin{pmatrix} 1 & 0 \\ 0 & t \end{pmatrix} \begin{pmatrix} \cos\left(\frac{\pi}{2N}\right) & \sin\left(\frac{\pi}{2N}\right) \\ \sin\left(\frac{\pi}{2N}\right) & -\cos\left(\frac{\pi}{2N}\right) \end{pmatrix} \right]^N \begin{pmatrix} 1 \\ 0 \end{pmatrix} \right|^2 . \tag{6.1}$$

[1]This is a slightly different version is given in Chapter 5 with Equation 5.1

The number of loops need to be controlled. In the original work by Kwiat *et al.* in using the optical loop, Pockel cells were used to rotate the polarization by $\frac{\pi}{2}$, which effectively swaps the polarization along each of the arms. The Pockel cells were dormant during the entire operation except for the final N^{th} loop. To understand propagation through the system, let us consider the vertical polarization path. During the previous N loops, the light would reflect at the second polarizing beam splitter; however, at the N^{th} loop, the Pockel cell would change the vertical polarization to horizontal polarization which would transmit through the second polarizing beam splitter which would leave the loop, and vice versa for the horizontal polarization path. This has the overall effect of allowing the photon to leave the setup after a controlled number of loops and encode the presence or absence of the object in the polarization degree of freedom albeit with the roles described above reversed due to the Pockel cell flipping.

It should be stressed, that QZI allows for the unambiguous non-destructive, non-interacting detection of an object with arbitrarily high fidelity and efficiency. But the original QZI is only limited to probing the binary state of a single object — either the object is present or not. To generalized the quantum Zeno interrogator I am interested in using a single photon to determine a multi-faceted property of a single object, or the state configuration of a collection of objects. Therefore, I need to use OAM, which has an arbitrary large Hilbert space. For the remainder of this chapter, I will discuss three different approaches I invented. I will discuss working or dud bombs like Elitzur and Vaidman did in their original non-demolition measurements [169] in order to explain the operating principle behind each of the generalizations. A working bomb will always absorb a single photon and then detonate while the dud bomb will be completely transparent. Each scheme, in the limit of infinite loops, will unambiguously determine the state configuration[2] of M bombs (which are working versus duds) with arbitrarily high fidelity and efficiency, whereas the state configuration is encoded in the OAM degree of freedom of a single photon.

[2]In the case of weak parallel QZI there is a slight restriction

6.2 Serial Binary QZI

The basic operating principle of the serial binary QZI is to use a series of original QZIs for each bomb with using OAM to encode the information. The original QZI can determine the state of a bomb and encode that information into polarization. This information can then be transferred over to the OAM degree of freedom. Because the OAM Hilbert space is arbitrarily large, each OAM value can be uniquely assigned to any combination of working and non-working bombs.

The more detailed operating principle is as follows. The photon is initially prepared as a horizontally polarized Gaussian ($\ell = 0$) $|H, 0\rangle$. Since the original QZI is agnostic to OAM, ℓ is unchanged. After passing through the first QZI the state with either vertically or horizontally polarized depending if the bomb was a working or dud[3]. If the bomb was working, then the photon would leave the QZI vertically polarized. The third polarizing beam splitter (PBS) (as seen in Figure 6.2) sends the photon down the lower path and passes through a wave plate and then the VPP with topological charge 2^{M-1}, where M is the total number of bombs. The wave plate resets the polarization back to $|H\rangle$ in preparation for the second QZI and the VPP encodes the state of the first bomb to the OAM degree of freedom with $\ell = 2^{M-1}$ (the $(M-1)^{th}$ binary digit). If the bomb was a dud, then the photon would leave the QZI horizontally polarized and pass through the PBS. To merge these two possibilities, a reverse Mach-Zehnder Dove prism interferometer [155, 158] is used as shown in Figure 2.12. The relative angle between the Dove prisms is chosen so that there will be a relative phase delay of $\frac{\pi}{2^{M-1}}\ell$. If states with $\ell = k2^{M-1}$ is sent in from the right (See Figure 6.2), then states with even k will be sent at the top, while states with odd k is sent towards the bottom. Therefore, when operated in reverse, if the even-or-odd k value condition is true then the states will merge along the same path. By construction, this situation is always true.

[3]Recall, if a Pockel cell is used to terminate the QZI after N loops, then the output polarization is actually reversed

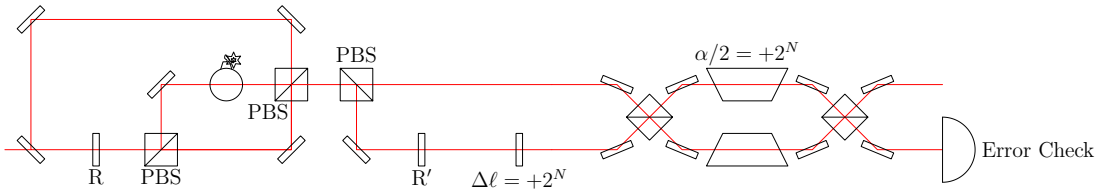

Figure 6.2: One complete unit of serial binary quantum Zeno interrogator is divided into three sections. The first section is an ordinary QZI in which the input photon will now be encoded with the configuration state of the bomb in the polarization degree of freedom. The second section will convert the polarization information into a binary digit of OAM, and then the third section, which is a reverse Mach-Zehnder Dove prism interferometer, allowed the photon to move to the upper path regardless of the OAM value in preparation for the next QZI in sequence.

For the second QZI the initial state is either $|H, 0\rangle$ or $|H, 2^{M-1}\rangle$ depending if the bomb was a dud or not. Once again, the QZI is agnostic to OAM so the value is unchanged and the state of the second bomb is encoded in the polarization and passes through a similar setup as the previous QZI except with a VPP with a reduced topological charge of 2^{M-2} and a Mach-Zehnder Dove prism interferometer with relative phase $\frac{\pi}{2^{M-2}}\ell$ between the two paths. Table 6.1 shows the combinations of possible ℓ values after two bombs. Note, in all four cases, if the photon is entering at the top of the second interferometer, it will have $\ell = k2^{M-2}$ where k is even, and k is odd, when entering from the bottom. Therefore, there will be a successful merger for any of the four combinations of bomb status with four unique ℓ values.

This process will continue for the M QZIs for the M bombs in which the VPPs topological charges will decrease by a factor of 2 each time, until having topological charge 1 for the last QZI and bomb. The final OAM value will have $\ell \in \left[0, 2^M - 1\right]$ to handle all 2^M possible combinations of M bomb configuration states. In fact, the binary encoding of ℓ will easily determine the bombs' configuration state. For example, for three bombs, $\ell = 5$ or $\ell = (101)_2$ will mean that bomb 1 is working, bomb 2 is not and bomb 3 is working.

Technically, if the bomb was active, there would be a small chance of loss, but as the number of loops increase, the probability of loss becomes arbitrarily small. In fact, the

Bomb 1	Bomb 2	ℓ	Path entering second interferometer
Dud	Dud	0	top
Dud	Working	2^{M-2}	bottom
Working	Dud	2^{M-1}	top
Working	Working	$2^{M-1} + 2^{M-2}$	bottom

Table 6.1: This table lists all the four possibilities of configuration states of the first two bombs and the OAM value shortly before the second Mach-Zehnder Dove-prism interferometer multiplexer. If the second bomb is a dud, it will enter the multiplexer on the upper path and will only successfully multiplex if the OAM value is an even multiple of 2^{M-2}. If the second bomb works, it will enter the multiplexer on the lower path and only successfully multiplex if the OAM value is an odd multiple of 2^{M-2}. These conditions hold for all the four possibilities. A similar table can be constructed for $M = 3$ bombs and will have eight possible configuration states and successful multiplexing still happens.

chance of loss is contingent upon the number of working bombs. If all are not working; there is no chance for loss because nothing will absorb the photon. For R working bombs, the probability of loss is given below:

$$P_{loss} = 1 - \cos\left(\frac{\pi}{2N}\right)^{2NR} \tag{6.2}$$

6.3 Weak Parallel QZI

For the next two parallel methods, it is important to revisit to the original QZI and determine what each component is abstractly and how to generalize. For the original QZI, a single object is probed and the state is encoded in polarization. The setup is a controlled loop with the polarization states spread out spatially by a PBS in order to selectively block one of the paths (in this chapter, we consider blocking the vertical path). A wave-plate is used to rotate the state from horizontal to vertical. Mathematically, this is just a rotation in $SO(2)$. Therefore, in order to probe all bombs simultaneously, or to probe a multi-faceted state, the PBS is replaced by an OAM beam-splitter as discussed in Chapter 2 and the wave-plate is replaced by an "OAM-rotator" that performs rotations in $SO(M+1)$ or $SO\left(2^M\right)$ for weak and strong parallel QZI respectively. Note, 2^M different states will be required to uniquely

identify all possible combinations of M bombs.

The first parallel scheme to be discussed is called "weak parallel QZI" because it only uses $M+1$ different states, as opposed to the full 2^M, which is reserved for "strong parallel QZI". If we consider the case of M bombs and know *a priori* at most one of the bombs is defective and the goal is to identify that bomb, then only $M+1$ states are required. This may seem contrived, but could be useful to probe a multi-faceted state that is sensitive to only a single OAM value from the set of OAM values chosen.

The scheme works by considering an $M+1$ subset in OAM space. Without loss of generalization, the subspace is $\ell \in [0, M]$. With this subspace taken, the state, before entering the weak parallel QZI setup as shown in Figure 6.3, is initialized to be $|\ell = 0\rangle$. The $|\ell = 0\rangle$ state is known as the control state, as was horizontal polarization in the original QZI. The state then passes through the "OAM-rotator" which is just a rotation in $SO(M+1)$, as given by Equation 6.3. The symbol $R^K_{\ell_1,\ell_2}(\theta)$ is a rotation in $SO(K)$ between axes ℓ_1 and ℓ_2 by an angle θ. Note, the dimensions start at $\ell = 0$ and thus the axes go from 0 to $K-1$. The full form is given in Equation 6.4 and explicit examples are given in Equations 6.5 and 6.6. $\delta_{i,j}$ is the Kronecker delta. For the original QZI the waveplate would do the operation $R^2_{H,V}\left(\frac{\pi}{2N}\right)$. In consistency with previous terminology, N is the predetermined number of loops.

$$R^{M+1}_{weakQZI}\left(\frac{\pi}{2N}\right) = R^{M+1}_{0,1}\left(\frac{\pi}{2N}\right) R^{M+1}_{0,2}\left(\frac{\pi}{2N}\right) \cdots R^{M+1}_{0,M}\left(\frac{\pi}{2N}\right) \tag{6.3}$$

$$\left[R^K_{\ell_1,\ell_2}(\theta)\right]_{i,j} = \delta_{i,j} + \delta_{\ell_1,\ell_1}(\cos\theta - 1) + \delta_{\ell_1,\ell_2}(-\sin\theta) + \delta_{\ell_2,\ell_1}(\sin\theta) + \delta_{\ell_1,\ell_1}(\cos\theta - 1) \tag{6.4}$$

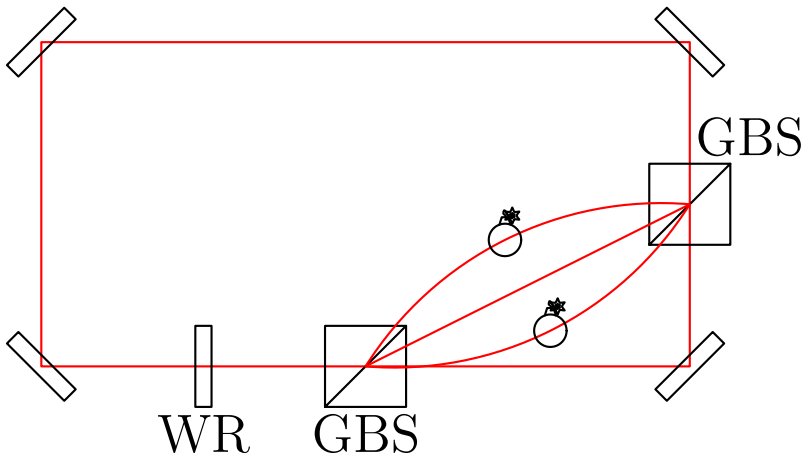

Figure 6.3: This is the weak parallel QZI setup for $M = 3$ bombs. For this particular setup, the second path has been arbitrarily selected to be free (bomb is a dud, thus transparent or not present). WR OAM-rotator which mathematically operates by the rotation matrix given be Equation 6.3 and GBS is an OAM beam-splitter which separates the states $\ell = 0, 1, 2$ and 3, to probe for the missing bomb. The curved paths are illustrative only. After N loops, the final output state will be mostly in $\ell = 2$.

$$R^3_{0,1}(\theta) = \begin{bmatrix} \cos\theta & -\sin\theta & 0 \\ \sin\theta & \cos\theta & 0 \\ 0 & 0 & 1 \end{bmatrix}; \quad R^3_{0,2}(\theta) = \begin{bmatrix} \cos\theta & 0 & -\sin\theta \\ 0 & 1 & 0 \\ \sin\theta & 0 & \cos\theta \end{bmatrix} \tag{6.5}$$

$$R^4_{1,2}(\theta) = \begin{bmatrix} 1 & 0 & 0 & 0 \\ 0 & \cos\theta & 0 & -\sin\theta \\ 0 & 0 & 1 & 0 \\ 0 & \sin\theta & 0 & \cos\theta \end{bmatrix} \tag{6.6}$$

After the "OAM-rotator" the state is now in a little bit of every OAM value, but still mostly in $|\ell = 0\rangle$ as long as N is relatively large. The photon now passes through the OAM beam-splitter which converts the OAM superposition into a superposition of all the paths. The path that $\ell = 0$ travels will always be empty, exactly like how the horizontal path was always empty in the original QZI. The other M paths will each contain a bomb with at most

one bomb a dud[4]. Like in the original QZI the presence of a working bomb will collapse the wave function into the transparent paths which is either the control ($\ell = 0$) if all bombs are working, or a superposition of the control and the bomb-free path. The actual state is given by the equation below:

$$|\psi\rangle_{weakQZI;M}^{N\ loops;\ 1\ pass} = Diag\left[1, \delta_{1,d}, \delta_{2,d}, \cdots, \delta_{M,d}\right] R_{weakQZI}^{M+1}\left(\frac{\pi}{2N}\right) \begin{bmatrix} 1 \\ 0 \\ \vdots \\ 0 \end{bmatrix} \tag{6.7}$$

The first element is a diagonal matrix where d refers to the index for the dud bomb. If there is no dud bomb, then $d = 0$. The final column vector represents the original input state which was $|\ell = 0\rangle$. Therefore, after N loops, the final state will be:

$$|\psi\rangle_{weakQZI;M}^{N\ loops;\ N\ passes} = \left[Diag\left[1, \delta_{1,d}, \delta_{2,d}, \cdots, \delta_{M,d}\right] R_{weakQZI}^{M+1}\left(\frac{\pi}{2N}\right)\right]^N \begin{bmatrix} 1 \\ 0 \\ \vdots \\ 0 \end{bmatrix} \tag{6.8}$$

In the limit as $N \to \infty$, becomes $|\ell = d\rangle$ as suggested from numerical analysis.

6.3.1 Reduction to original QZI ($M = 1$ bomb)

In the case of $M = 1$, Equation 6.8 reduces to the original QZI and we can solve for the state exactly:

[4]Or missing — whatever makes the path effectively transparent

$$|\psi\rangle_{weakQZI;1}^{N\ loops;\ N\ passes} = \left(\begin{bmatrix} 1 & 0 \\ 0 & \delta_{1,d} \end{bmatrix} \begin{bmatrix} \cos\frac{\pi}{2N} & -\sin\frac{\pi}{2N} \\ \sin\frac{\pi}{2N} & \cos\frac{\pi}{2N} \end{bmatrix} \right)^N \begin{bmatrix} 1 \\ 0 \end{bmatrix} = \begin{bmatrix} \delta_{0,d}\cos^N\left(\frac{\pi}{2N}\right) \\ \delta_{1,d} \end{bmatrix} \tag{6.9}$$

If there is no dud ($d = 0$), the probability that the state will be in $\ell = 0$ (analogous to horizontal polarization in the original QZI) is given below. There is also no chance for $\ell = 1$ (vertical) and loss is $1 - P_2(\ell = 0)$.

$$P_2(\ell = 0) = \cos^{2N}\left(\frac{\pi}{2N}\right) \tag{6.10}$$

If there is a dud ($d = 1$), then there is no chance for $\ell = 0$ (horizontal) and 100% for $\ell = 1$ (vertical) and no chance for loss. This once again, is what is expected from the original QZI. The limit of $N \to \infty$ $P_2(\ell = 0) \to 1$. The derivation is given in A.

6.3.2 $M > 1$ bombs

For $M > 1$ bombs, the general form of Equation 6.8 is quite complicated and not very illuminating; therefore, results as a function of N (number of loops) and M (number of bombs) will be plotted. In the original QZI ($M = 1$, single bomb case), there is no crosstalk, only loss. For the weak parallel QZI with $M > 1$, there is crosstalk due to the non-abelian nature of the rotation matrices. The crosstalk quickly vanishes as N increases (See Figure 6.5). Numerical approximations up to $M = 150$ and $N = 10000$ (See Figure 6.4 and 6.5) is highly suggestive that the final result will be $|\ell = d\rangle$ where d represented which bomb was a dud as defined earlier.

The purpose of weak parallel is not to identify the complete configuration state of all bombs, but to determine which of the M bombs, if any, is a dud. For other quantum systems, weak parallel QZI would be useful for anything with many states in which all but one act differently and trying to probe for the difference without disturbing any of the other

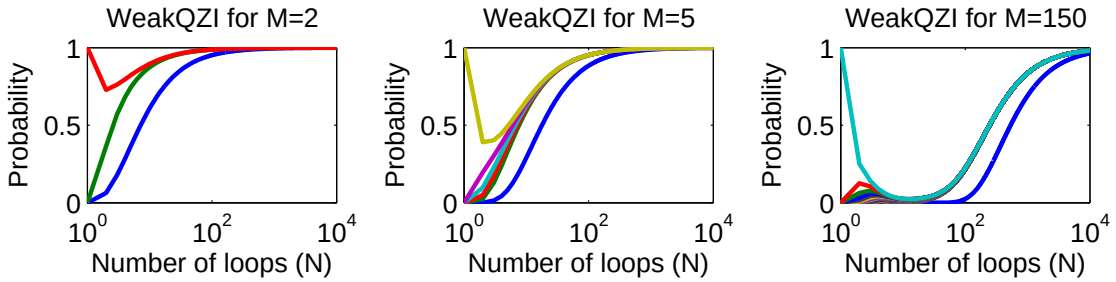

Figure 6.4: Weak parallel QZI is successful in the limit of large number of loops (N); however, even for a small, but non-trivial number of bombs (e.g., $M = 5$), only about 10 loops are required to have a greater than 50% chance of detecting the dud bomb. For a larger number of bombs, say $M = 150$, the number of required loops in on the order of hundreds for better than 50% success; however, will still be perfectly successful in the limit of infinite number of loops, like the original QZI. In the limit of small loop numbers (N), the results are chaotic due to the non-abelian nature of $SO(N > 2)$. However, after a reasonable number of loops, all M possible dud bomb's configurations coalesce to an asymptotic limit of $\cos\left(\frac{\pi}{2N}\right)^{2N\frac{M-1}{2}}$. The line set apart is the case in which there are no dud-bombs and the result will return the control $\ell = 0$. The probability of that is exactly $1-$ Equation 6.2 for all N. For fixed M and N the loss with no dud-bombs is greater than the loss with at least one dud-bomb. This makes sense because there is a greater of loss if there are more working bombs (chance to be absorbed).

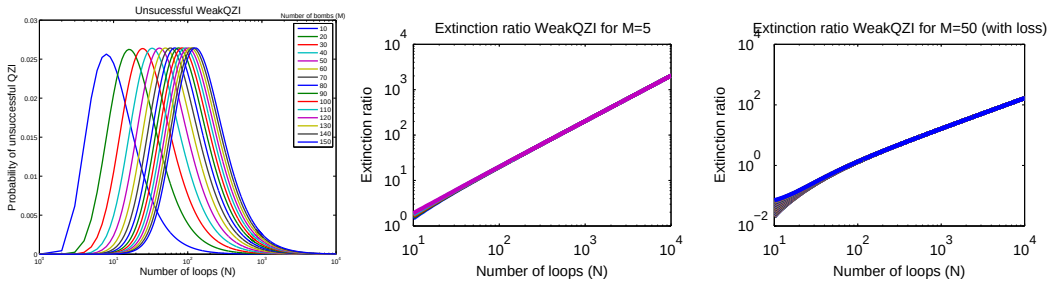

Figure 6.5: (Left) The chance for misleading QZI, which is defined as returning the control state $\ell = 0$ when there was actually a dud bomb, starts out small, reaches a peak value a little over 2.5% and then vanishes to zero in the limit of large number of loops. This peak position increases for increasingly large number of bombs. The reason the misleading rate starts out low is because the loss rate dominates. (Center) The ratio between the probability of a successful QZI and a false one for $M = 5$ bombs for each possible bomb. Once again, due to the non-abelian algebra of $SO(N > 2)$, the order of rotation matrices matters until the angles become insignificant (large N) and then results coalesce. (Right) The same ratio, but with $M = 50$ bombs. In both cases, plotting starts after $N = 10$ because the ratios are extremely small due to high loss.

states.

6.4 Strong Parallel QZI

Strong parallel QZI, as the name suggests, is like weak parallel QZI but determines full configuration state of all M bombs (or objects) and therefore requires 2^M orthogonal OAM states to encode the information. Strong parallel QZI operates very similarly to weak parallel QZI except with a few key differences. The initial state for both parallel schemes is $|\ell = 0\rangle$ and the output state, in the limit of infinite number of loops, will exactly [5] tell the information about the bombs. There is still an OAM rotator required; except now that rotations are done in $SO(2^M)$ and is a bit more complicated. An OAM beam-splitter is also required, but will separate the 2^M states along 2^M paths instead of $M + 1$. $\ell = 0$ will still be the control, and the M bombs will now have to block multiple paths in such a way that uniquely determines the configuration state of the bombs.

To better conceptualize how strong parallel QZI works, let us first discuss the M-dimensional hypercube. The first three hypercubes are drawn in Figure 6.6. An M-dimensional hypercube is embedded in M-dimensional space. Each dimension has a one-to-one relationship with each bomb. There are 2^M vertices in this hypercube. Each vertex can be uniquely identified by the coordinate vector in $\mathbb{R}^M$ whereas the sides of the hypercube are length 1 and one of the corners is affixed to the origin. That vector has a one-to-one relationship with the 2^M different bomb configuration states by the relation that a 0 in index K indicates that bomb K works. Each vector can easily be mapped to a binary number and will be any number between 0 and $2^M - 1$. This is the same as in the serial binary QZI case, except now with the roles of 0 and 1 reversed.

On the same M-dimensional hypercube, there are $M2^{M-1}$ edges. Each edge is connected to two vertices and each vertex is uniquely determined by an integer between 0 and

[5] Numerical approximations suggest this.

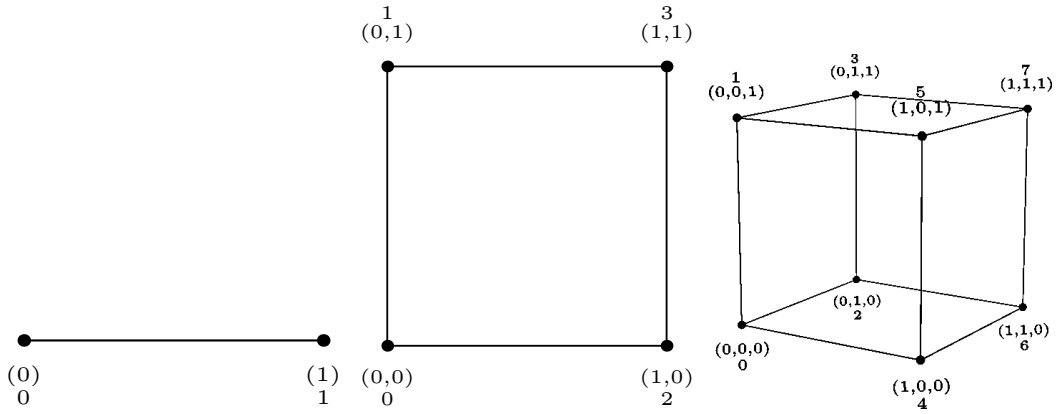

Figure 6.6: The first three hypercubes, also known as line, square and cube. The vertices are labelled twice by a binary vector as explained in the text and the decimal representation of the binary vector, which will also be the logical OAM value attached to that vertex. The hypercubes are not necessary to understand strong parallel QZI, but are rather used as an analogy to give an intuitive understanding for the equations and algorithms. Note, the logical OAM values need not be sequential as seen by $M = 3$ in which vertices associated with the the principle axes are labeled $\ell = 1, 2$ and 4.

$2^M - 1$. Consider a rotation in $\mathbb{R}^{2^M}$ between the axes defined by the integer representing the two vertices at the ends of a particular edge by an angle $\frac{\pi}{2N}$. Each of these rotation matrices are an element of set Q. The set Q spans all the edges of the hypercube. The total rotation matrix required for successful strong parallel QZI is the product of these matrices in set Q. Like in the weak parallel QZI, due to the non-abelian nature of $SO(N > 2)$, the exact order of the rotations will change intermediary results; however, in the limit of infinite number of loops (N) the effect or order is negligible. The equation for this rotation matrix is given below and an algorithm to calculate these rotation matrices of set Q is given in Section B.

$$R^{2^M}_{strongQZI}\left(\frac{\pi}{2N}\right) = \prod_{(i,j)\in Q} R^{2^M}_{i,j}\left(\frac{\pi}{2N}\right) \tag{6.11}$$

Since there are 2^M OAM states, the OAM beam-splitter will separate these states into 2^M paths. However, there are only M bombs; therefore, each bomb will be set to block multiple paths. Of course, if the bomb is a dud, the bomb is transparent and will not absorb

the photon along its assigned path(s). The first[6] path ($\ell = 0$) is always unblocked because it is the control. The next M paths[7] are each blocked by a single bomb. The next $\binom{M}{2}$ paths are blocked by two bombs and so forth. Recall $\sum_{i=0}^{M}\binom{M}{i} = 2^M$ so there are the correct number of paths. Given a path L, in order to determine which bombs block said path, convert L into binary and if the i^{th} digit is 1, then the i^{th} bomb blocks that path; otherwise not. It can be clearly seen that the control path $\ell = 0$ is $(000\cdots000)_2$ and thus no bombs block its path; while $2^M - 1$ is $(111\cdots111)_2$ and all bombs block its path. Consider the configuration state of the bombs (working versus non-working) as an M-dimensional vector $\vec{d}$, we can define 2^M different matrices $P_{M,\vec{d}}$ that is a diagonal matrix, with a 1 in the (i,i) position if the i^{th} path is open (all bombs assigned to that path are duds). An algorithm to calculate these matrices is given in Section B. Note, because of the binary mapping, the numbers may not be consecutive. For example with $M = 3$, $\ell = 0$ is the control path, but $\ell = 1, 2, 4$ will only have a single bomb assigned to its path. However, these ℓ values denote logical OAM values and any set of 2^M OAM values can be used and they need not even be consecutive nor equally spaced. The arrangement is chosen for easier mathematical mapping. In Figure 6.7 I show the arrangement for $M = 2$ and $M = 3$.

We can now explicitly calculate the outcome state from the strong parallel QZI for any number of bombs (M) and any number of loops (N) by using Equation 6.8 and replacing the weak parallel elements with the strong parallel ones. The equation is given below:

$$|\psi\rangle_{strongQZI;M}^{N\ loops;\ N\ passes} = \left[P_{M,\vec{d}}R_{strongQZI}^{2^M}\left(\frac{\pi}{2N}\right)\right]^N \begin{bmatrix}1\\0\\\vdots\\0\end{bmatrix} \tag{6.12}$$

As in the weak parallel QZI case, if there is only a single bomb; the above equation reduces to the original QZI case which has already been discussed in Section 6.3.1. For

[6] One path is $\binom{M}{0}$
[7] $\binom{M}{1}$

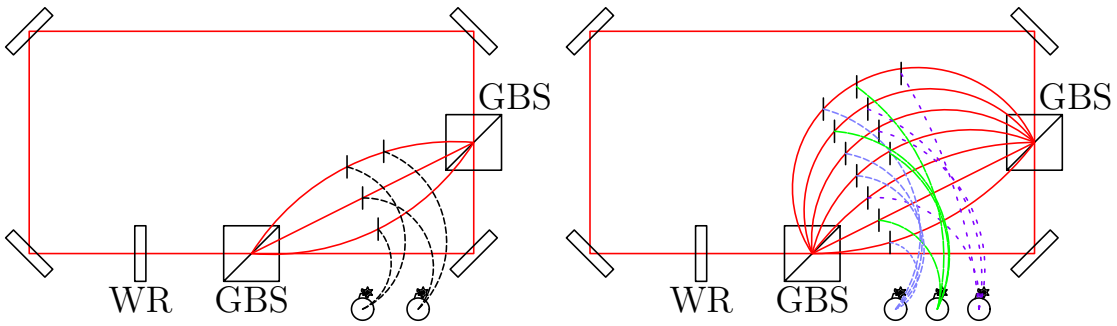

Figure 6.7: Strong parallel QZI setup for 2 (Left) and 3 (Right) bombs. As in the weak parallel case, WR is a OAM-rotator that performs the action of Equation 6.11. GBS is an OAM beam-splitter that now separates 2^M different OAM modes. Because there are now more paths than bombs, bombs have multi triggers for multiple paths. In the case where there is more than one triggers on a single path, the order of the triggers does not matter because if the path was going to be blocked by any of the bombs, then the path would be blocked; it need not be the first bomb. By strategically positioning the triggers along all the paths, which state the photon evolves into will uniquely determine the bomb configuration. For $M = 3$ bombs (right image), the different bomb to path mappings are color coded as such: cyan (dashed), green (solid) and purple (dotted).

$M > 1$ bombs, the expression in Equation 6.12 has no simple closed form, but numerical results tell a similar tale as weak parallel QZI.

Once again, as the number of loops (N) increase the probability of success approaches unity (See Figure 6.8) while the probability of misleading results (wrong result) or loss reaches as peak not immediately at low N, but shortly thereafter until tapering off as the probability of success approaches unity (See Figure 6.9) of the form [8] below, where D is the number of dud bombs:

$$\cos\left(\frac{\pi}{2N}\right)^{2N(M-D)} \tag{6.13}$$

There will be $\binom{M}{D}$[9] states that approach each limit, since the more working bombs there are, the more likely a loss can occur.

[8] Except for $D = M$.

[9] $\binom{M}{D} = \binom{M}{M-D}$

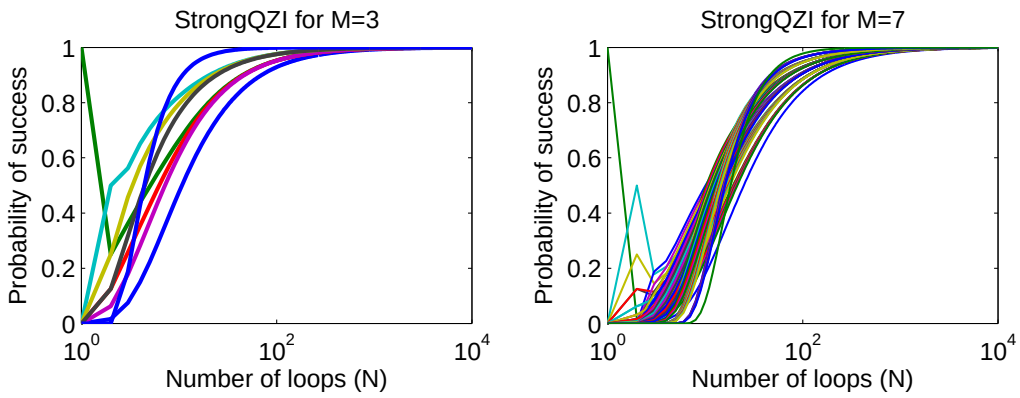

Figure 6.8: Except for the first few loops, the probability of success starts low and then asymptotically approaches unity in a form similar to 1-Equation 6.2. With one exception, the asymptotic limit is $\cos\left(\frac{\pi}{2N}\right)^{2N(M-D)}$ where M is the total bombs and D are the amount of duds. In the case of no duds, this answer is exact except for $N = 1$. This is the expected control ($\ell = 0$) solution. The exception is where $D = M$ in which no simple expression matches the asymptotic limit.

6.5 Conclusions

I have developed and described three generalizations for the original quantum Zeno interrogator developed by Kwiat *et al.* [159]. The first, serial binary QZI keeps the use of polarization for the actual QZI probing, but then shifts proved information into the arbitrarily large Hilbert space of OAM. The downside is that the amount of objects scales with the number of bombs and fast, high-fidelity optical switches may be too impractical to chain more than a few serial binary schemes together. The other two generalizations probe the information in parallel by using the OAM degree of freedom to probe the state(s) directly. In the case of $M = 1$, both parallel schemes simplify back to the original QZI, since there will only be 2 OAM states. For $M > 1$, the size of the Hilbert space exceeds 2, and thus the algebra of the rotation matrices is non-abelian. In the limit of large number of loops, the various states coalesce to an asymptotic term that is associated with the number of working bombs, and not the order of the rotation in the rotation matrices 6.3 and 6.11. In future work, I hope to definitively prove I get the state $|\ell = \vec{d}\rangle$ where $\vec{d}$ is either the number of the dud bomb (weak parallel) or the vector associated with the bomb's state configura-

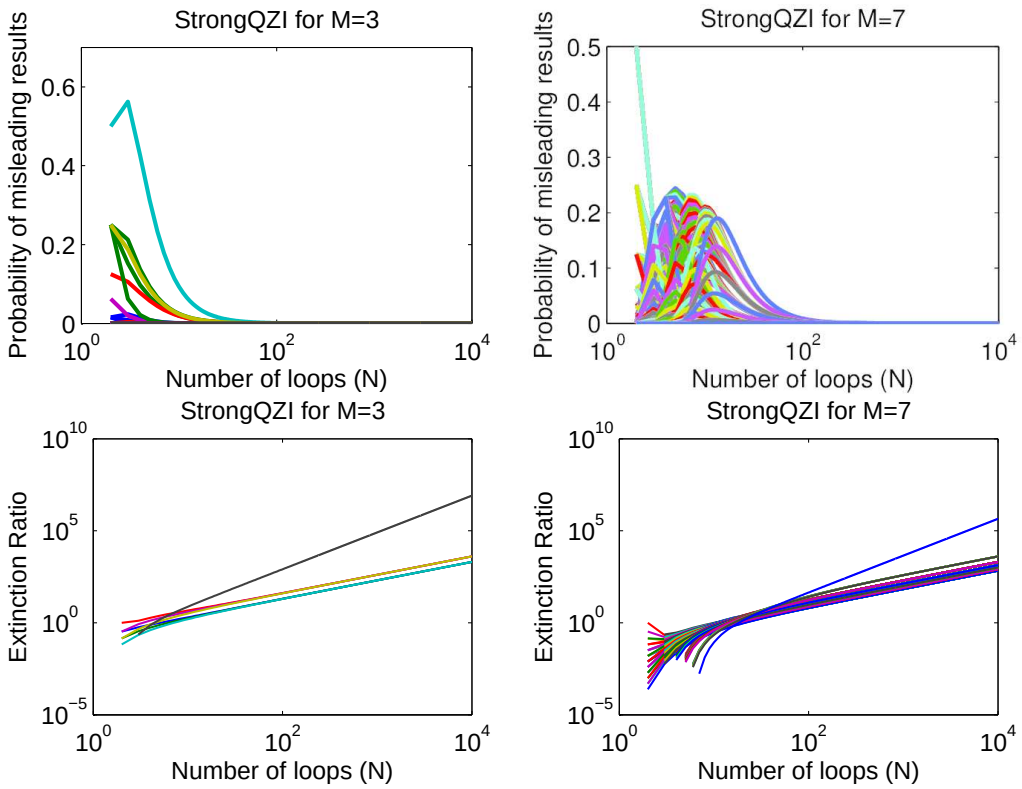

Figure 6.9: (Top Row) These results are different from the weak parallel QZI case where the only misleading value would be getting $\ell = 0$ when there was a dud bomb. In the strong parallel QZI case, if there are multiple dud bombs, the union of ℓ states assigned to any of those bombs has potential to be a misleading error. The correct result is only the intersect, which is always a single ℓ value. (Bottom row) The ratio between getting a successful QZI versus any other result misleading or lost, steadily increases as the number of loops (N) increases; which is expected.

tion (strong parallel). These three schemes demonstrate a unique quantum algorithm only available to high dimensional states, systems that orbital angular momentum of light can reach.

CHAPTER 7

Conclusions

In 1992, Allen *et al.* realized that light contains a well defined orbital angular momentum (OAM) in the paraxial approximation [6]. This ushered in a burgeoning new era of optical research and researchers worldwide have used OAM for a variety of applications. However, in order to use OAM for any of these applications, one must first need robust methods to create, transmit and detect OAM. The first part of my thesis focused on the detecting, or measuring, OAM, while the second part presents an application of OAM using the higher dimensional states it provides.

In this thesis, I give a history of previous methods by other researchers used for measuring OAM. Many of them measure OAM by mapping to some other degree of freedom and then making a measurement. Often, the different OAM states will go along different paths or ports. Therefore, in order to measure more OAM states, more paths, ports or experimental resources will be required. Additionally, larger optics will be required to support the larger spatial extend of higher order transverse modes.

My schemes differ from all previous schemes by using an optical loop device in order to map OAM to the temporal degree of freedom. My OAM measuring devices accomplished several goals:

1. Due to the optical loop design, the same number of optical elements can be used to measure any number of OAM states. Many other schemes require more optical elements to measure more OAM states. My methods were the *first* to use the optical

loop design.

2. Both devices have high fidelity. Additionally, the overall concept of the optical loop does not require a specific OAM filter, so any future OAM filters with better fidelity can be easily incorporated into either of my schemes.

3. The devices are fast and due to the optical loop design are compact.

The first scheme I presented is a projective OAM spectrometer that has average nearest neighbor crosstalk of less than -21.3 dB for 5 different OAM states, which is among the highest reported fidelities in the literature. The second scheme is an extension of the first, but is an OAM-beam splitter, which means that it can determine the OAM value of a single photon. The second scheme achieves this by inserting a quantum Zeno interrogator that can non-destructively determine if a photon of a certain ℓ value would pass through a filter or not. This allows the mapping of OAM to time-binning with arbitrarily high efficiency while still maintaining high fidelity.

In the second part of my thesis, I discuss a particular quantum algorithm that uses the high dimensionality of OAM that I call the generalized quantum Zeno interrogator. In the original scheme by Kwiat *et al.* [159], they use the polarization degree of freedom to non-destructively probe the 1-bit state of an a single object. In the experiment, they can determine if the object is transparent or opaque without directly interacting with the object. I extend this to use the OAM degree of freedom to non-destructively probe higher dimensional states. This has not been discussed in the literature.

I present three different generalizations:

Serial Binary QZI: This uses the original polarization-based QZI but transfers the information to the OAM degree of freedom to non-destructively probe and store the full configuration of M objects.

Weak Parallel QZI: This uses OAM as a generalization of polarization from two dimensions to M dimensions to non-destructively probe an object (or set of objects) and

discern from M+1 possibilities.

Strong Parallel QZI: This extends the weak parallel case, but can determine the full state configuration of M objects using only the OAM degree of freedom of a single photon.

These schemes shows a concrete example of how the higher dimensionality of OAM can solve problems inaccessible to polarization. These schemes also demonstrate that not only does OAM have increased bandwidth for communication purposes, but can extract higher dimensional information from quantum systems.

The OAM measurement schemes presented in this paper can allow for better measurement of OAM states for communication and imaging purposes. In the future, higher fidelities can be achieved be controlling the misalignment. Additionally, when optical elements continue to improve, in the limit of perfect optics, the Quantum Zeno-based OAM spectrometer provides the only scheme that can measure an arbitrarily large OAM value with arbitrarily high fidelity and efficiency of a single photon.

The generalize QZIs presented in this dissertation allows for non-destructive characterization of higher dimensional states. Future work could involve the experimental realization of the first non-trivial example with weak parallel QZI with two objects and three OAM states. This could be achieved with today's experimental equipment. All these schemes allow access to higher dimensional states via the exploitation of OAM.

APPENDIX A

Mathematical Derivations

Original QZI proper limit

For the original QZI, or any of the generalized QZI in the limit of a single bomb, the probability of detecting the presence of the bomb, if there is a working bomb is given by Equation 6.10. In Kwiat *et al.*, [159] they state that this cosine probability will go to 1 in the limit that N approaches infinity; however, they do not derive the expression.

In this section, I will rigorously provide that derivation. First take the natural log of both sides of Equation 6.10

$$\lim_{N\to\infty} \log\left(P_2(\ell=0)\right) = \lim_{N\to\infty} 2N \times \cos\left(\frac{\pi}{2N}\right) = \lim_{N\to\infty} \frac{\cos\left(\frac{\pi}{2N}\right)}{1/(2N)} \tag{A.1}$$

This expression is indeterminate (0/0) so invoke l'Hôpital's rule [172] yielding the expression below:

$$\lim_{N\to\infty} \log\left(P_2(\ell=0)\right) = \lim_{N\to\infty} \frac{\frac{\pi}{2}\tan\frac{\pi}{2N}\frac{1}{N^2}}{-\frac{1}{2N^2}} = \lim_{N\to\infty} -\pi\tan\frac{\pi}{2N} = 0 \tag{A.2}$$

$$\lim_{N\to\infty} \left(P_2(\ell=0)\right) = \mathrm{e}^0 = 1 \quad \square \tag{A.3}$$

APPENDIX B

Programs

Strong QZI programs

Determine Rotation Matrices for Strong QZI

In this section, I will describe how to generate the strong parallel QZI rotation matrix in Equation 6.11, or more precisely derive the pair of indices in set Q. As discussed in the text, the rotation matrix is a product of rotation matrices in $\mathbb{R}^{2^M}$ between the axes i and j, which are the vertices at the endpoints of an edge of the hypercube. Iterate over all the edges and one will have the matrix.

To understand how to iterate over all the edges, first consider a unidirectional graph of the vertices of the hypercube.

The algorithm is to simply traverse the graph. However, this process will have duplicated entries. The version that I coded checks to see if the node was already visited. The code is two functions. The main function strongRotList.m and a helper recursive function strongRotListHelper.m. The code is not optimized for efficiency, but not important since the number of dimensions used is small (only went up to $N = 7$ in thesis). The source code is included below:

```
function strongList = strongRotList(numDim)


strongList = strongRotListHelper(numDim,zeros(1,numDim),0);
strongList = strongList(1:end-1,:);
```

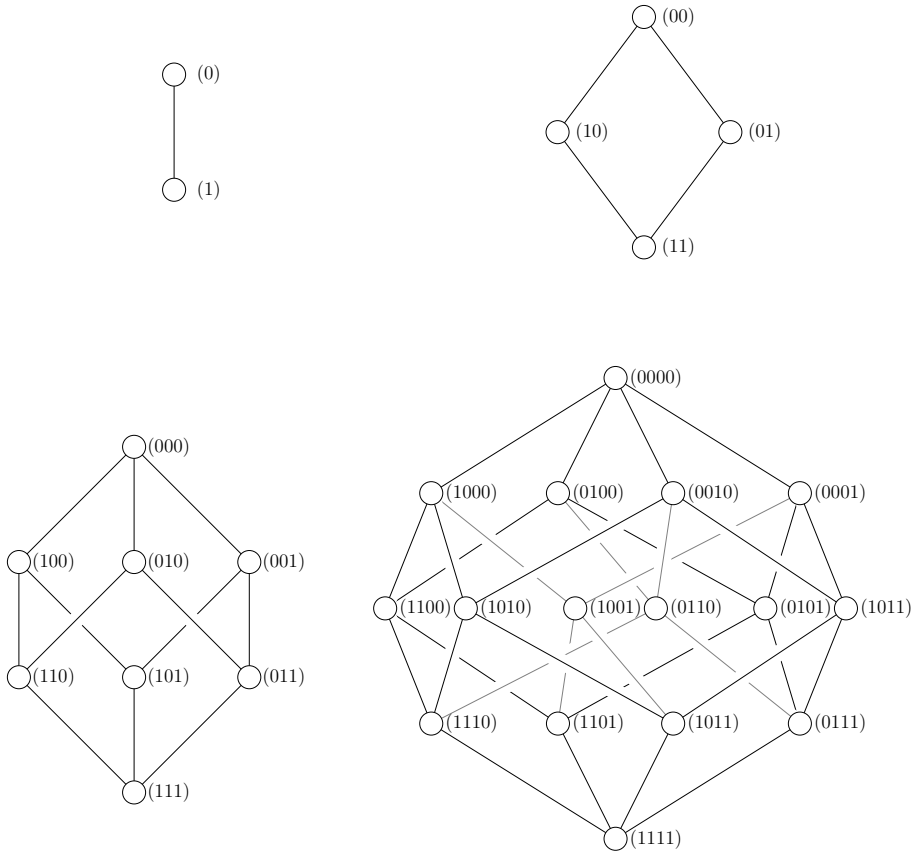

Figure B.1: These are the unidirection graphs of the vertices and edges of the first four hypercubes. This is also a two-dimensional representation of these hypercubes. The vertices are labelled with their coordinates in $\mathbb{R}^N$ where $N = 1, 2, 3, 4$.

```
end
```

```
function strongList = strongRotListHelper(numDim, currentBin,ci,strongList)
if(ci==0)
    strongList=[-1,-1];
end

for i=1:numDim,
    if(currentBin(i) == 0)
        newBin = currentBin;
        newBin(i)=1;
```

```
        %check for duplicates
        skip=0;
        for ak=1:size(strongList,1),
            if(strongList(ak,:) == [bi2de(currentBin),bi2de(newBin)])
                skip=1;
                break;
            end
        end

        if(skip==0)
            strongList = [bi2de(currentBin), bi2de(newBin);
                        strongRotListHelper(numDim, newBin,1,strongList)];
        end
    end
end

end
```

Determine Path Matrix for Strong QZI

In this section I will provide the algorithm to calculate $P_{M,\vec{d}}$ for strong parallel QZI. This is a straight-forward program that takes the input binary vector $\vec{d}$, or openPath in the source code which states which of the M bombs are duds. This outputs a $2^M \times 2^M$ matrix.

```
function pathMat = strongPath(numDims,openPath)

pathMat=zeros(2^numDims,2^numDims);
curPath=zeros(1,numDims);
testPath=zeros(1,numDims);

for i=0:2^numDims-1,
    testPath=de2bi(i,numDims);
    isLegit=1;
    for j=1:numDims,
        if(testPath(j)==1 && openPath(j)==1)
            isLegit=isLegit*1;
        elseif(testPath(j)==1 && openPath(j)==0)
            isLegit=isLegit*0;
        end
```

```
    end
    if(isLegit==1)
        pathMat(bi2de(testPath)+1,bi2de(testPath)+1)=1;
    end
end
end
```

BIBLIOGRAPHY

[1] Geissbuehler, M. and Lasser, T., "How to display data by color schemes compatible with red-green color perception deficiencies," *Optics Express*, Vol. 21, No. 8, April 2013, pp. 9862–9874.

[2] Eastman, P., *Go, Dog. Go!*, Beginner Books(R), Random House Children's Books, 1961.

[3] Maxwell, J. C., "A Dynamical Theory of the Electromagnetic Field," *Philosophical Transactions of the Royal Society of London*, Vol. 155, Jan. 1865, pp. 459–512.

[4] Poynting, J. H., "On the Transfer of Energy in the Electromagnetic Field," *Philosophical Transactions of the Royal Society of London*, Vol. 175, Jan. 1884, pp. 343–361.

[5] Poynting, J. H., "The Wave Motion of a Revolving Shaft, and a Suggestion as to the Angular Momentum in a Beam of Circularly Polarised Light," *Proceedings of the Royal Society of London. Series A*, Vol. 82, No. 557, July 1909, pp. 560–567.

[6] Allen, L., Beijersbergen, M. W., Spreeuw, R. J. C., and Woerdman, J. P., "Orbital angular momentum of light and the transformation of Laguerre-Gaussian laser modes," *Physical Review A*, Vol. 45, No. 11, June 1992, pp. 8185.

[7] Jackson, J. D., *Classical Electrodynamics Third Edition*, Wiley, 3rd ed., Aug. 1998.

[8] Abers, E. S., *Quantum Mechanics*, Benjamin Cummings, June 2003.

[9] Beth, R. A., "Mechanical Detection and Measurement of the Angular Momentum of Light," *Physical Review*, Vol. 50, No. 2, July 1936, pp. 115.

[10] Moothoo, D. N., Arlt, J., Conroy, R. S., Akerboom, F., Voit, A., and Dholakia, K., "Beths experiment using optical tweezers," *American Journal of Physics*, Vol. 69, No. 3, 2001, pp. 271.

[11] Siegman, A. E., *Lasers*, University Science Books, Jan. 1986.

[12] Barnett, S. M. and Allen, L., "Orbital angular momentum and nonparaxial light beams," *Optics Communications*, Vol. 110, No. 56, Sept. 1994, pp. 670–678.

[13] Siegman, A. E., "Hermite-gaussian functions of complex argument as optical-beam eigenfunctions," *Journal of the Optical Society of America*, Vol. 63, No. 9, Sept. 1973, pp. 1093–1094.

[14] Saleh, B. E. A. and Teich, M. C., *Fundamentals of Photonics*, Wiley-Interscience, 2nd ed., March 2007.

[15] Yao, A. M. and Padgett, M. J., "Orbital angular momentum: origins, behavior and applications," *Advances in Optics and Photonics*, Vol. 3, No. 2, June 2011, pp. 161–204.

[16] Kimel, I. and Elias, L. R., "Relations between Hermite and Laguerre Gaussian modes," *IEEE Journal of Quantum Electronics*, Vol. 29, No. 9, 1993, pp. 2562–2567.

[17] Berry, M. V., Nye, J. F., and Wright, F. J., "The Elliptic Umbilic Diffraction Catastrophe," *Philosophical Transactions of the Royal Society of London. Series A, Mathematical and Physical Sciences*, Vol. 291, No. 1382, April 1979, pp. 453–484.

[18] Coullet, P., Gil, L., and Rocca, F., "Optical vortices," *Optics Communications*, Vol. 73, No. 5, Nov. 1989, pp. 403–408.

[19] Nye, J. F. and Berry, M. V., "Dislocations in Wave Trains," *Proceedings of the Royal Society of London. A. Mathematical and Physical Sciences*, Vol. 336, No. 1605, Jan. 1974, pp. 165–190.

[20] Bazhenov, V., Vasnetsov, M., and Soskin, M. S., "Laser-beams with screw dislocation in their wave-fronts," *JETP LETTERS*, Vol. 52, No. 8, Oct. 1990, pp. 429–431.

[21] Bandres, M. A. and Gutiérrez-Vega, J., "Ince Gaussian beams," *Optics Letters*, Vol. 29, No. 2, Jan. 2004, pp. 144–146.

[22] Bandres, M. A. and Gutiérrez-Vega, J. C., "Ince-Gaussian modes of the paraxial wave equation and stable resonators," *Journal of the Optical Society of America A*, Vol. 21, No. 5, May 2004, pp. 873–880.

[23] Bandres, M. A., "Elegant Ince-Gaussian beams," *Optics Letters*, Vol. 29, No. 15, Aug. 2004, pp. 1724–1726.

[24] Durnin, J., "Exact solutions for nondiffracting beams. I. The scalar theory," *Journal of the Optical Society of America A*, Vol. 4, No. 4, April 1987, pp. 651–654.

[25] Gori, F., Guattari, G., and Padovani, C., "Bessel-Gauss beams," *Optics Communications*, Vol. 64, No. 6, Dec. 1987, pp. 491–495.

[26] Einstein, A., "über einen die Erzeugung und Verwandlung des Lichtes betreffenden heuristischen Gesichtspunkt," *Annalen der Physik*, Vol. 322, No. 6, Jan. 1905, pp. 132–148.

[27] Dholakia, K., Simpson, N. B., Padgett, M. J., and Allen, L., "Second-harmonic generation and the orbital angular momentum of light," *Physical Review A*, Vol. 54, No. 5, Nov. 1996, pp. R3742–R3745.

[28] Einstein, A., Podolsky, B., and Rosen, N., "Can Quantum-Mechanical Description of Physical Reality Be Considered Complete?" *Physical Review*, Vol. 47, No. 10, May 1935, pp. 777.

[29] Bell, J., "On the Einstein Podolsky Rosen Paradox," *Physics*, Vol. 1, 1964, pp. 195–200.

[30] Clauser, J. F., Horne, M. A., Shimony, A., and Holt, R. A., "Proposed Experiment to Test Local Hidden-Variable Theories," *Physical Review Letters*, Vol. 23, No. 15, Oct. 1969, pp. 880.

[31] Freedman, S. J. and Clauser, J. F., "Experimental Test of Local Hidden-Variable Theories," *Physical Review Letters*, Vol. 28, No. 14, April 1972, pp. 938.

[32] Horodecki, R., Horodecki, P., Horodecki, M., and Horodecki, K., "Quantum entanglement," *Reviews of Modern Physics*, Vol. 81, No. 2, June 2009, pp. 865.

[33] Kwiat, P. G., Mattle, K., Weinfurter, H., Zeilinger, A., Sergienko, A. V., and Shih, Y., "New High-Intensity Source of Polarization-Entangled Photon Pairs," *Physical Review Letters*, Vol. 75, No. 24, Dec. 1995, pp. 4337.

[34] Burnham, D. C. and Weinberg, D. L., "Observation of Simultaneity in Parametric Production of Optical Photon Pairs," *Physical Review Letters*, Vol. 25, No. 2, July 1970, pp. 84–87.

[35] Hong, C. K. and Mandel, L., "Theory of parametric frequency down conversion of light," *Physical Review A*, Vol. 31, No. 4, April 1985, pp. 2409.

[36] Ou, Z. Y. and Mandel, L., "Violation of Bell's Inequality and Classical Probability in a Two-Photon Correlation Experiment," *Physical Review Letters*, Vol. 61, No. 1, July 1988, pp. 50–53.

[37] Shih, Y. H. and Alley, C. O., "New Type of Einstein-Podolsky-Rosen-Bohm Experiment Using Pairs of Light Quanta Produced by Optical Parametric Down Conversion," *Physical Review Letters*, Vol. 61, No. 26, Dec. 1988, pp. 2921–2924.

[38] Rarity, J. G. and Tapster, P. R., "Experimental violation of Bells inequality based on phase and momentum," *Physical Review Letters*, Vol. 64, No. 21, May 1990, pp. 2495–2498.

[39] Howell, J. C., Bennink, R. S., Bentley, S. J., and Boyd, R. W., "Realization of the Einstein-Podolsky-Rosen Paradox Using Momentum- and Position-Entangled Photons from Spontaneous Parametric Down Conversion," *Physical Review Letters*, Vol. 92, No. 21, May 2004, pp. 210403.

[40] Strekalov, D. V., Pittman, T. B., Sergienko, A. V., Shih, Y. H., and Kwiat, P. G., "Postselection-free energy-time entanglement," *Physical Review A*, Vol. 54, No. 1, July 1996, pp. R1–R4.

[41] Tittel, W., Brendel, J., Zbinden, H., and Gisin, N., "Violation of Bell Inequalities by Photons More Than 10 km Apart," *Physical Review Letters*, Vol. 81, No. 17, Oct. 1998, pp. 3563–3566.

[42] Brendel, J., Gisin, N., Tittel, W., and Zbinden, H., "Pulsed Energy-Time Entangled Twin-Photon Source for Quantum Communication," *Physical Review Letters*, Vol. 82, No. 12, March 1999, pp. 2594–2597.

[43] Walborn, S. P., Pádua, S., and Monken, C. H., "Conservation and entanglement of Hermite-Gaussian modes in parametric down-conversion," *Physical Review A*, Vol. 71, No. 5, May 2005, pp. 053812.

[44] Ren, X.-F., Guo, G.-P., Li, J., and Guo, G.-C., "Entanglement of the HermiteGaussian modes states of photons," *Physics Letters A*, Vol. 341, No. 14, June 2005, pp. 81–86.

[45] Salakhutdinov, V. D., Eliel, E. R., and Löffler, W., "Full-Field Quantum Correlations of Spatially Entangled Photons," *Physical Review Letters*, Vol. 108, No. 17, April 2012, pp. 173604.

[46] McLaren, M., Agnew, M., Leach, J., Roux, F. S., Padgett, M. J., Boyd, R. W., and Forbes, A., "Entangled Bessel-Gaussian beams," *Optics Express*, Vol. 20, No. 21, Oct. 2012, pp. 23589–23597.

[47] Krenn, M., Fickler, R., Huber, M., Lapkiewicz, R., Plick, W., Ramelow, S., and Zeilinger, A., "Entangled singularity patterns of photons in Ince-Gauss modes," *Physical Review A*, Vol. 87, No. 1, Jan. 2013, pp. 012326.

[48] Kwiat, P. G., "Hyper-entangled states," *Journal of Modern Optics*, Vol. 44, No. 11-12, Nov. 1997, pp. 2173–2184.

[49] Yang, T., Zhang, Q., Zhang, J., Yin, J., Zhao, Z., ukowski, M., Chen, Z.-B., and Pan, J.-W., "All-Versus-Nothing Violation of Local Realism by Two-Photon, Four-Dimensional Entanglement," *Physical Review Letters*, Vol. 95, No. 24, Dec. 2005, pp. 240406.

[50] Cinelli, C., Barbieri, M., Perris, R., Mataloni, P., and Martini, F. D., "All-Versus-Nothing Nonlocality Test of Quantum Mechanics by Two-Photon Hyperentanglement," *Physical Review Letters*, Vol. 95, No. 24, Dec. 2005, pp. 240405.

[51] Barreiro, J. T., Langford, N. K., Peters, N. A., and Kwiat, P. G., "Generation of Hyperentangled Photon Pairs," *Physical Review Letters*, Vol. 95, No. 26, Dec. 2005, pp. 260501.

[52] Nagali, E. and Sciarrino, F., "Generation of hybrid polarization-orbital angular momentum entangled states," *Optics Express*, Vol. 18, No. 17, 2010, pp. 18243–18248.

[53] Mair, A., Vaziri, A., Weihs, G., and Zeilinger, A., "Entanglement of the orbital angular momentum states of photons," *Nature*, Vol. 412, No. 6844, July 2001, pp. 313–316.

[54] Dada, A. C., Leach, J., Buller, G. S., Padgett, M. J., and Andersson, E., "Experimental high-dimensional two-photon entanglement and violations of generalized Bell inequalities," *Nat Phys*, Vol. 7, No. 9, 2011, pp. 677–680.

[55] Krenn, M., Huber, M., Fickler, R., Lapkiewicz, R., Ramelow, S., and Zeilinger, A., "Generation and confirmation of a (100 100)-dimensional entangled quantum system," *Proceedings of the National Academy of Sciences*, Vol. 111, No. 17, April 2014, pp. 6243–6247.

[56] Feng, S. and Kumar, P., "Spatial Symmetry and Conservation of Orbital Angular Momentum in Spontaneous Parametric Down-Conversion," *Physical Review Letters*, Vol. 101, No. 16, Oct. 2008, pp. 163602.

[57] Romero, J., Giovannini, D., McLaren, M. G., Galvez, E. J., Forbes, A., and Padgett, M. J., "Orbital angular momentum correlations with a phase-flipped Gaussian mode pump beam," *Journal of Optics*, Vol. 14, No. 8, Aug. 2012, pp. 085401.

[58] Miatto, F. M., Yao, A. M., and Barnett, S. M., "Full characterization of the quantum spiral bandwidth of entangled biphotons," *Physical Review A*, Vol. 83, No. 3, March 2011, pp. 033816.

[59] Torres, J. P., Alexandrescu, A., and Torner, L., "Quantum spiral bandwidth of entangled two-photon states," *Physical Review A*, Vol. 68, No. 5, Nov. 2003, pp. 050301.

[60] Merali, Z., "Quantum Mechanics Braces for the Ultimate Test," *Science*, Vol. 331, No. 6023, March 2011, pp. 1380–1382.

[61] Weihs, G., Jennewein, T., Simon, C., Weinfurter, H., and Zeilinger, A., "Violation of Bell's Inequality under Strict Einstein Locality Conditions," *Physical Review Letters*, Vol. 81, No. 23, Dec. 1998, pp. 5039–5043.

[62] Rowe, M. A., Kielpinski, D., Meyer, V., Sackett, C. A., Itano, W. M., Monroe, C., and Wineland, D. J., "Experimental violation of a Bell's inequality with efficient detection," *Nature*, Vol. 409, No. 6822, Feb. 2001, pp. 791–794.

[63] Giustina, M., Mech, A., Ramelow, S., Wittmann, B., Kofler, J., Beyer, J., Lita, A., Calkins, B., Gerrits, T., Nam, S. W., Ursin, R., and Zeilinger, A., "Bell violation using entangled photons without the fair-sampling assumption," *Nature*, Vol. 497, No. 7448, May 2013, pp. 227–230.

[64] Vértesi, T., Pironio, S., and Brunner, N., "Closing the Detection Loophole in Bell Experiments Using Qudits," *Physical Review Letters*, Vol. 104, No. 6, Feb. 2010, pp. 060401.

[65] Heisenberg, W., "Über den anschaulichen Inhalt der quantentheoretischen Kinematik und Mechanik," *Zeitschrift für Physik*, Vol. 43, No. 3-4, March 1927, pp. 172–198.

[66] Weyl, H., "Quantenmechanik und Gruppentheorie," *Zeitschrift für Physik*, Vol. 46, No. 1-2, Nov. 1927, pp. 1–46.

[67] Robertson, H. P., "The Uncertainty Principle," *Physical Review*, Vol. 34, No. 1, July 1929, pp. 163–164.

[68] Franke-Arnold, S., Barnett, S. M., Yao, E., Leach, J., Courtial, J., and Padgett, M., "Uncertainty principle for angular position and angular momentum," *New Journal of Physics*, Vol. 6, Aug. 2004, pp. 103–103.

[69] Barnett, S. M. and Pegg, D. T., "Quantum theory of rotation angles," *Physical Review A*, Vol. 41, No. 7, April 1990, pp. 3427–3435.

[70] Jha, A. K., Jack, B., Yao, E., Leach, J., Boyd, R. W., Buller, G. S., Barnett, S. M., Franke-Arnold, S., and Padgett, M. J., "Fourier relationship between the angle and angular momentum of entangled photons," *Physical Review A*, Vol. 78, No. 4, Oct. 2008, pp. 043810.

[71] Jha, A. K., Leach, J., Jack, B., Franke-Arnold, S., Barnett, S. M., Boyd, R. W., and Padgett, M. J., "Angular Two-Photon Interference and Angular Two-Qubit States," *Physical Review Letters*, Vol. 104, No. 1, Jan. 2010, pp. 010501.

[72] Vaziri, A., Weihs, G., and Zeilinger, A., "Experimental Two-Photon, Three-Dimensional Entanglement for Quantum Communication," *Physical Review Letters*, Vol. 89, No. 24, Nov. 2002, pp. 240401.

[73] Gibson, G., Courtial, J., Padgett, M., Vasnetsov, M., Pas'ko, V., Barnett, S., and Franke-Arnold, S., "Free-space information transfer using light beams carrying orbital angular momentum," *Optics Express*, Vol. 12, No. 22, Nov. 2004, pp. 5448–5456.

[74] Bennett, C. H. and Brassard, G., "Quantum cryptography: Public key distribution and coin tossing," *Proceedings of IEEE International Conference on Computers, Systems and Signal Processing*, Vol. 175, No. 0, 1984.

[75] Shor, P. W. and Preskill, J., "Simple Proof of Security of the BB84 Quantum Key Distribution Protocol," *Physical Review Letters*, Vol. 85, No. 2, July 2000, pp. 441–444.

[76] Shor, P., "Algorithms for quantum computation: discrete logarithms and factoring," *, 35th Annual Symposium on Foundations of Computer Science, 1994 Proceedings*, Nov. 1994, pp. 124–134.

[77] Bourennane, M., Karlsson, A., and Björk, G., "Quantum key distribution using multilevel encoding," *Physical Review A*, Vol. 64, No. 1, June 2001, pp. 012306.

[78] Cerf, N. J., Bourennane, M., Karlsson, A., and Gisin, N., "Security of Quantum Key Distribution Using d-Level Systems," *Physical Review Letters*, Vol. 88, No. 12, March 2002, pp. 127902.

[79] Bruß, D. and Macchiavello, C., "Optimal Eavesdropping in Cryptography with Three-Dimensional Quantum States," *Physical Review Letters*, Vol. 88, No. 12, March 2002, pp. 127901.

[80] Durt, T., Kaszlikowski, D., Chen, J., and Kwek, L. C., "Security of quantum key distributions with entangled qudits," *Physical Review A*, Vol. 69, No. 3, March 2004, pp. 032313.

[81] Gröblacher, S., Jennewein, T., Vaziri, A., Weihs, G., and Zeilinger, A., "Experimental quantum cryptography with qutrits," *New Journal of Physics*, Vol. 8, No. 5, May 2006, pp. 75.

[82] Molina-Terriza, G., Vaziri, A., Ursin, R., and Zeilinger, A., "Experimental Quantum Coin Tossing," *Physical Review Letters*, Vol. 94, No. 4, Jan. 2005, pp. 040501.

[83] Shi, Y., "Both Toffoli and Controlled-NOT need little help to do universal quantum computation," *arXiv:quant-ph/0205115*, May 2002.

[84] Ralph, T. C., Resch, K. J., and Gilchrist, A., "Efficient Toffoli gates using qudits," *Physical Review A*, Vol. 75, No. 2, Feb. 2007, pp. 022313.

[85] Nielsen, M. A., Bremner, M. J., Dodd, J. L., Childs, A. M., and Dawson, C. M., "Universal simulation of Hamiltonian dynamics for quantum systems with finite-dimensional state spaces," *Physical Review A*, Vol. 66, No. 2, Aug. 2002, pp. 022317.

[86] Wang, X., Sanders, B. C., and Berry, D. W., "Entangling power and operator entanglement in qudit systems," *Physical Review A*, Vol. 67, No. 4, April 2003, pp. 042323.

[87] Wang, J., Yang, J.-Y., Fazal, I. M., Ahmed, N., Yan, Y., Huang, H., Ren, Y., Yue, Y., Dolinar, S., Tur, M., and Willner, A. E., "Terabit free-space data transmission employing orbital angular momentum multiplexing," *Nature Photonics*, Vol. 6, No. 7, 2012, pp. 488–496.

[88] Bozinovic, N., Yue, Y., Ren, Y., Tur, M., Kristensen, P., Huang, H., Willner, A. E., and Ramachandran, S., "Terabit-Scale Orbital Angular Momentum Mode Division Multiplexing in Fibers," *Science*, Vol. 340, No. 6140, June 2013, pp. 1545–1548.

[89] Paterson, C., "Atmospheric Turbulence and Orbital Angular Momentum of Single Photons for Optical Communication," *Physical Review Letters*, Vol. 94, No. 15, April 2005, pp. 153901.

[90] Tyler, G. A. and Boyd, R. W., "Influence of atmospheric turbulence on the propagation of quantum states of light carrying orbital angular momentum," *Optics Letters*, Vol. 34, No. 2, Jan. 2009, pp. 142–144.

[91] Rodenburg, B., Lavery, M. P. J., Malik, M., O'Sullivan, M. N., Mirhosseini, M., Robertson, D. J., Padgett, M., and Boyd, R. W., "Influence of atmospheric turbulence on states of light carrying orbital angular momentum," *Optics Letters*, Vol. 37, No. 17, Sept. 2012, pp. 3735–3737.

[92] Pors, B.-J., Monken, C. H., Eliel, E. R., and Woerdman, J. P., "Transport of orbital-angular-momentum entanglement through a turbulent atmosphere," *Optics Express*, Vol. 19, No. 7, March 2011, pp. 6671–6683.

[93] Tamburini, F., Mari, E., Sponselli, A., Thidé, B., Bianchini, A., and Romanato, F., "Encoding many channels on the same frequency through radio vorticity: first experimental test," *New Journal of Physics*, Vol. 14, No. 3, March 2012, pp. 033001.

[94] Torner, L., Torres, J., and Carrasco, S., "Digital spiral imaging," *Optics Express*, Vol. 13, No. 3, Feb. 2005, pp. 873–881.

[95] Molina-Terriza, G., Rebane, L., Torres, J. P., Torner, L., and Carrasco, S., "Probing canonical geometrical objects by digital spiral imaging," *Journal of the European Optical Society: Rapid Publications*, Vol. 2, April 2007.

[96] Petrov, D., Rahuel, N., Molina-Terriza, G., and Torner, L., "Characterization of dielectric spheres by spiral imaging," *Optics Letters*, Vol. 37, No. 5, March 2012, pp. 869–871.

[97] Simon, D. S. and Sergienko, A. V., "Two-photon spiral imaging with correlated orbital angular momentum states," *Physical Review A*, Vol. 85, No. 4, April 2012, pp. 043825.

[98] Uribe-Patarroyo, N., Fraine, A., Simon, D. S., Minaeva, O., and Sergienko, A. V., "Object Identification Using Correlated Orbital Angular Momentum States," *Physical Review Letters*, Vol. 110, No. 4, Jan. 2013, pp. 043601.

[99] Chen, L., Lei, J., and Romero, J., "Quantum digital spiral imaging," *Light: Science & Applications*, Vol. 3, No. 3, March 2014, pp. e153.

[100] Simon, D. S., Jaeger, G., and Sergienko, A. V., "Quantum information in communication and imaging," *International Journal of Quantum Information*, Vol. 12, No. 04, June 2014, pp. 1430004.

[101] Fürhapter, S., Jesacher, A., Bernet, S., and Ritsch-Marte, M., "Spiral phase contrast imaging in microscopy," *Optics Express*, Vol. 13, No. 3, Feb. 2005, pp. 689–694.

[102] Steiger, R., Bernet, S., and Ritsch-Marte, M., "Mapping of phase singularities with spiral phase contrast microscopy," *Optics Express*, Vol. 21, No. 14, July 2013, pp. 16282–16289.

[103] Swartzlander, Grover A., J., "Peering into darkness with a vortex spatial filter," *Optics Letters*, Vol. 26, No. 8, April 2001, pp. 497–499.

[104] Foo, G., Palacios, D. M., and Swartzlander, J., "Optical vortex coronagraph," *Optics Letters*, Vol. 30, No. 24, Dec. 2005, pp. 3308–3310.

[105] Swartzlander, G. A. J., "The optical vortex coronagraph," *Journal of Optics A: Pure and Applied Optics*, Vol. 11, No. 9, Sept. 2009, pp. 094022.

[106] Molina-Terriza, G., Torres, J. P., and Torner, L., "Management of the Angular Momentum of Light: Preparation of Photons in Multidimensional Vector States of Angular Momentum," *Physical Review Letters*, Vol. 88, No. 1, Dec. 2001, pp. 013601.

[107] Tamburini, F., Anzolin, G., Umbriaco, G., Bianchini, A., and Barbieri, C., "Overcoming the Rayleigh Criterion Limit with Optical Vortices," *Physical Review Letters*, Vol. 97, No. 16, Oct. 2006, pp. 163903.

[108] Mari, E., Tamburini, F., Swartzlander, G. A., Bianchini, A., Barbieri, C., Romanato, F., and Thidé, B., "Sub-Rayleigh optical vortex coronagraphy," *Optics Express*, Vol. 20, No. 3, Jan. 2012, pp. 2445–2451.

[109] Swartzlander, G. A., Ford, E. L., Abdul-Malik, R. S., Close, L. M., Peters, M. A., Palacios, D. M., and Wilson, D. W., "Astronomical demonstration of an optical vortex coronagraph," *Optics Express*, Vol. 16, No. 14, July 2008, pp. 10200–10207.

[110] Peters, M. A., Close, L. M., Rademacher, M., Stalcup, T., Swartzlander, G. A., Ford, E., and Abdul-Malik, R. S., "A high-Strehl low-resolution optical imager (BESSEL): Detection of a 0.7/D separation binary from the ground," *New Astronomy*, Vol. 13, No. 5, July 2008, pp. 359–369.

[111] Mawet, D., Serabyn, E., Liewer, K., Burruss, R., Hickey, J., and Shemo, D., "The Vector Vortex Coronagraph: Laboratory Results and First Light at Palomar Observatory," *The Astrophysical Journal*, Vol. 709, No. 1, Jan. 2010, pp. 53.

[112] Serabyn, E., Mawet, D., and Burruss, R., "An image of an exoplanet separated by two diffraction beamwidths from a star," *Nature*, Vol. 464, No. 7291, April 2010, pp. 1018–1020.

[113] Tamburini, F., Thidé, B., Molina-Terriza, G., and Anzolin, G., "Twisting of light around rotating black holes," *Nature Physics*, Vol. 7, No. 3, 2011, pp. 195–197.

[114] Rumala, Y. S. and Leanhardt, A. E., "Multiple-beam interference in a spiral phase plate," *Journal of the Optical Society of America B*, Vol. 30, No. 3, March 2013, pp. 615–621.

[115] Rumala, Y. S., "Interference theory of multiple optical vortex states in spiral phase plate etalon: thick-plate and thin-plate approximation," *Journal of the Optical Society of America B*, Vol. 31, No. 6, June 2014, pp. A6–A12.

[116] Lavery, M. P. J., Speirits, F. C., Barnett, S. M., and Padgett, M. J., "Detection of a Spinning Object Using Lights Orbital Angular Momentum," *Science*, Vol. 341, No. 6145, Aug. 2013, pp. 537–540.

[117] Ashkin, A., Dziedzic, J. M., Bjorkholm, J. E., and Chu, S., "Observation of a single-beam gradient force optical trap for dielectric particles," *Optics Letters*, Vol. 11, No. 5, May 1986, pp. 288–290.

[118] He, H., Friese, M. E. J., Heckenberg, N. R., and Rubinsztein-Dunlop, H., "Direct Observation of Transfer of Angular Momentum to Absorptive Particles from a Laser Beam with a Phase Singularity," *Physical Review Letters*, Vol. 75, No. 5, July 1995, pp. 826–829.

[119] Friese, M. E. J., Enger, J., Rubinsztein-Dunlop, H., and Heckenberg, N. R., "Optical angular-momentum transfer to trapped absorbing particles," *Physical Review A*, Vol. 54, No. 2, Aug. 1996, pp. 1593–1596.

[120] Lee, M. P., Curran, A., Gibson, G. M., Tassieri, M., Heckenberg, N. R., and Padgett, M. J., "Optical shield: measuring viscosity of turbid fluids using optical tweezers," *Optics Express*, Vol. 20, No. 11, May 2012, pp. 12127–12132.

[121] Arlt, J. and Padgett, M. J., "Generation of a beam with a dark focus surrounded by regions of higher intensity: the optical bottle beam," *Optics Letters*, Vol. 25, No. 4, Feb. 2000, pp. 191–193.

[122] Heckenberg, N. R., McDuff, R., Smith, C. P., and White, A. G., "Generation of optical phase singularities by computer-generated holograms," *Optics Letters*, Vol. 17, No. 3, Feb. 1992, pp. 221–223.

[123] Harris, M., Hill, C. A., Tapster, P. R., and Vaughan, J. M., "Laser modes with helical wave fronts," *Physical Review A*, Vol. 49, No. 4, April 1994, pp. 3119–3122.

[124] Hecht, E., *Optics*, Addison Wesley, 4th ed., Aug. 2001.

[125] Hickmann, J. M., Fonseca, E. J. S., Soares, W. C., and Chávez-Cerda, S., "Unveiling a Truncated Optical Lattice Associated with a Triangular Aperture Using Light's Orbital Angular Momentum," *Physical Review Letters*, Vol. 105, No. 5, July 2010, pp. 053904.

[126] Berkhout, G. C. G. and Beijersbergen, M. W., "Method for Probing the Orbital Angular Momentum of Optical Vortices in Electromagnetic Waves from Astronomical Objects," *Physical Review Letters*, Vol. 101, No. 10, Sept. 2008, pp. 100801.

[127] Berkhout, G. C. G. and Beijersbergen, M. W., "Using a multipoint interferometer to measure the orbital angular momentum of light in astrophysics," *Journal of Optics A: Pure and Applied Optics*, Vol. 11, No. 9, Sept. 2009, pp. 094021.

[128] Li, F., song Jiang, Y., Tang, H., and Ou, J., "Measuring the azimuthal and radial indexes of Laguerre-Gaussian beams," *Optoelectronics Letters*, Vol. 6, No. 3, May 2010, pp. 222–225.

[129] Wang, Z., Zhang, Z., and Lin, Q., "A novel method to determine the helical phase structure of LaguerreGaussian beams," *Journal of Optics A: Pure and Applied Optics*, Vol. 11, No. 8, Aug. 2009, pp. 085702.

[130] Beijersbergen, M., Allen, L., van der Veen, H., and Woerdman, J., "Astigmatic laser mode converters and transfer of orbital angular momentum," *Optics Communications*, Vol. 96, No. 13, Feb. 1993, pp. 123–132.

[131] Courtial, J., Dholakia, K., Allen, L., and Padgett, M., "Gaussian beams with very high orbital angular momentum," *Optics Communications*, Vol. 144, No. 4-6, Dec. 1997, pp. 210–213.

[132] Topuzoski, S. and Janicijevic, L., "Fraunhofer diffraction of a LaguerreGaussian laser beam by fork-shaped grating," *Journal of Modern Optics*, Vol. 58, No. 2, 2011, pp. 138.

[133] Karimi, E., Zito, G., Piccirillo, B., Marrucci, L., and Santamato, E., "Hypergeometric-Gaussian modes," *Optics Letters*, Vol. 32, No. 21, Nov. 2007, pp. 3053–3055.

[134] Davis, J. A., Cottrell, D. M., Campos, J., Yzuel, M. J., and Moreno, I., "Encoding amplitude information onto phase-only filters," *Applied Optics*, Vol. 38, No. 23, Aug. 1999, pp. 5004–5013.

[135] Ando, T., Ohtake, Y., Matsumoto, N., Inoue, T., and Fukuchi, N., "Mode purities of Laguerre-Gaussian beams generated via complex-amplitudemodulation using phase-only spatial light modulators," *Optics Letters*, Vol. 34, No. 1, Jan. 2009, pp. 34–36.

[136] Bolduc, E., Bent, N., Santamato, E., Karimi, E., and Boyd, R. W., "Exact solution to simultaneous intensity and phase encryption with a single phase-only hologram," *Optics Letters*, Vol. 38, No. 18, Sept. 2013, pp. 3546–3549.

[137] Beijersbergen, M. W., Coerwinkel, R. P. C., Kristensen, M., and Woerdman, J. P., "Helical-wavefront laser beams produced with a spiral phaseplate," *Optics Communications*, Vol. 112, No. 5-6, Dec. 1994, pp. 321–327.

[138] Oemrawsingh, S. S. R., van Houwelingen, J. A. W., Eliel, E. R., Woerdman, J. P., Verstegen, E. J. K., Kloosterboer, J. G., and 't Hooft, G. W., "Production and characterization of spiral phase plates for optical wavelengths," *Applied Optics*, Vol. 43, No. 3, Jan. 2004, pp. 688–694.

[139] Heckenberg, N. R., McDuff, R., Smith, C. P., Rubinsztein-Dunlop, H., and Wegener, M. J., "Laser beams with phase singularities," *Optical and Quantum Electronics*, Vol. 24, No. 9, Sept. 1992, pp. S951–S962.

[140] Bekshaev, A. and Karamoch, A., "Spatial characteristics of vortex light beams produced by diffraction gratings with embedded phase singularity," *Optics Communications*, Vol. 281, No. 6, March 2008, pp. 1366–1374.

[141] Sueda, K., Miyaji, G., Miyanaga, N., and Nakatsuka, M., "Laguerre-Gaussian beam generated with a multilevel spiral phase plate for high intensity laser pulses," *Optics Express*, Vol. 12, No. 15, July 2004, pp. 3548–3553.

[142] Shen, Y., Campbell, G. T., Hage, B., Zou, H., Buchler, B. C., and Lam, P. K., "Generation and interferometric analysis of high charge optical vortices," *Journal of Optics*, Vol. 15, No. 4, April 2013, pp. 044005.

[143] Campbell, G., Hage, B., Buchler, B., and Lam, P. K., "Generation of high-order optical vortices using directly machined spiral phase mirrors," *Applied Optics*, Vol. 51, No. 7, March 2012, pp. 873–876.

[144] Moh, K. J., Yuan, X.-C., Cheong, W. C., Zhang, L. S., Lin, J., Ahluwalia, B. P. S., and Wang, H., "High-power efficient multiple optical vortices in a single beam generated by a kinoform-type spiral phase plate," *Applied Optics*, Vol. 45, No. 6, Feb. 2006, pp. 1153–1161.

[145] Marrucci, L., Manzo, C., and Paparo, D., "Optical Spin-to-Orbital Angular Momentum Conversion in Inhomogeneous Anisotropic Media," *Physical Review Letters*, Vol. 96, No. 16, April 2006, pp. 163905.

[146] Miller, D. A. B., "Communicating with Waves Between Volumes: Evaluating Orthogonal Spatial Channels and Limits on Coupling Strengths," *Applied Optics*, Vol. 39, No. 11, April 2000, pp. 1681–1699.

[147] Lavery, M. P. J., Robertson, D. J., Sponselli, A., Courtial, J., Steinhoff, N. K., Tyler, G. A., Wilner, A. E., and Padgett, M. J., "Efficient measurement of an optical orbital-angular-momentum spectrum comprising more than 50 states," *New Journal of Physics*, Vol. 15, No. 1, Jan. 2013, pp. 013024.

[148] Padgett, M. J. and Lesso, J. P., "Dove prisms and polarized light," *Journal of Modern Optics*, Vol. 46, No. 2, 1999, pp. 175–179.

[149] Moreno, I., Paez, G., and Strojnik, M., "Polarization transforming properties of Dove prisms," *Optics Communications*, Vol. 220, No. 46, May 2003, pp. 257–268.

[150] Moreno, I., "Jones Matrix for Image-Rotation Prisms," *Applied Optics*, Vol. 43, No. 17, June 2004, pp. 3373–3381.

[151] Garetz, B. A. and Arnold, S., "Variable frequency shifting of circularly polarized laser radiation via a rotating half-wave retardation plate," *Optics Communications*, Vol. 31, No. 1, Oct. 1979, pp. 1–3.

[152] Courtial, J., Dholakia, K., Robertson, D. A., Allen, L., and Padgett, M. J., "Measurement of the Rotational Frequency Shift Imparted to a Rotating Light Beam Possessing Orbital Angular Momentum," *Physical Review Letters*, Vol. 80, No. 15, April 1998, pp. 3217–3219.

[153] Courtial, J., Robertson, D. A., Dholakia, K., Allen, L., and Padgett, M. J., "Rotational Frequency Shift of a Light Beam," *Physical Review Letters*, Vol. 81, No. 22, Nov. 1998, pp. 4828–4830.

[154] Leach, J., Padgett, M. J., Barnett, S. M., Franke-Arnold, S., and Courtial, J., "Measuring the Orbital Angular Momentum of a Single Photon," *Physical Review Letters*, Vol. 88, No. 25, June 2002, pp. 257901.

[155] Wei, H., Xue, X., Leach, J., Padgett, M. J., Barnett, S. M., Franke-Arnold, S., Yao, E., and Courtial, J., "Simplified measurement of the orbital angular momentum of single photons," *Optics Communications*, Vol. 223, No. 1-3, July 2003, pp. 117–122.

[156] Leach, J., Courtial, J., Skeldon, K., Barnett, S. M., Franke-Arnold, S., and Padgett, M. J., "Interferometric Methods to Measure Orbital and Spin, or the Total Angular Momentum of a Single Photon," *Physical Review Letters*, Vol. 92, No. 1, Jan. 2004, pp. 013601.

[157] Lavery, M. P. J., Dudley, A., Forbes, A., Courtial, J., and Padgett, M. J., "Robust interferometer for the routing of light beams carrying orbital angular momentum," *New Journal of Physics*, Vol. 13, No. 9, Sept. 2011, pp. 093014.

[158] García-Escartín, J. C. and Chamorro-Posada, P., "Quantum multiplexing with the orbital angular momentum of light," *Physical Review A*, Vol. 78, No. 6, Dec. 2008, pp. 062320.

[159] Kwiat, P. G., White, A. G., Mitchell, J. R., Nairz, O., Weihs, G., Weinfurter, H., and Zeilinger, A., "High-Efficiency Quantum Interrogation Measurements via the Quantum Zeno Effect," *Physical Review Letters*, Vol. 83, No. 23, Dec. 1999, pp. 4725.

[160] Bierdz, P. and Deng, H., "A compact orbital angular momentum spectrometer using quantum zeno interrogation," *Optics Express*, Vol. 19, No. 12, June 2011, pp. 11615–11622.

[161] Berkhout, G. C. G., Lavery, M. P. J., Courtial, J., Beijersbergen, M. W., and Padgett, M. J., "Efficient Sorting of Orbital Angular Momentum States of Light," *Physical Review Letters*, Vol. 105, No. 15, Oct. 2010, pp. 153601.

[162] Bryngdahl, O., "Geometrical transformations in optics," *Journal of the Optical Society of America*, Vol. 64, No. 8, Aug. 1974, pp. 1092–1099.

[163] Lavery, M. P. J., Robertson, D. J., Berkhout, G. C. G., Love, G. D., Padgett, M. J., and Courtial, J., "Refractive elements for the measurement of the orbital angular momentum of a single photon," *Optics Express*, Vol. 20, No. 3, Jan. 2012, pp. 2110–2115.

[164] Dudley, A., Mhlanga, T., Lavery, M., McDonald, A., Roux, F. S., Padgett, M., and Forbes, A., "Efficient sorting of Bessel beams," *Optics Express*, Vol. 21, No. 1, Jan. 2013, pp. 165–171.

[165] Mirhosseini, M., Malik, M., Shi, Z., and Boyd, R. W., "Efficient separation of the orbital angular momentum eigenstates of light," *Nature Communications*, Vol. 4, Nov. 2013.

[166] Bierdz, P., Kwon, M., Roncaioli, C., and Deng, H., "High fidelity detection of the orbital angular momentum of light by time mapping," *New Journal of Physics*, Vol. 15, No. 11, Nov. 2013, pp. 113062.

[167] Karimi, E., Marrucci, L., de Lisio, C., and Santamato, E., "Time-division multiplexing of the orbital angular momentum of light," *Optics Letters*, Vol. 37, No. 2, Jan. 2012, pp. 127–129.

[168] Peres, A., "Zeno paradox in quantum theory," *American Journal of Physics*, Vol. 48, No. 11, 1980, pp. 931.

[169] Elitzur, A. C. and Vaidman, L., "Quantum mechanical interaction-free measurements," *Foundations of Physics*, Vol. 23, No. 7, July 1993, pp. 987–997.

[170] Misra, B. and Sudarshan, E. C. G., "The Zenos paradox in quantum theory," *Journal of Mathematical Physics*, Vol. 18, No. 4, 1977, pp. 756.

[171] Jang, J.-S., "Optical interaction-free measurement of semitransparent objects," *Physical Review A*, Vol. 59, No. 3, March 1999, pp. 2322.

[172] l'Hôpital, G., *Analyse des infiniment petits, pour l'intelligence des lignes courbes*, Paris : Montalant, 1716.